An Arctic sea ice concentration data record on a 6.25 km polar stereographic grid from three-years' Landsat-8 imagery

Hee-Sung Jung[1], Sang-Moo Lee[1,2], Joo-Hong Kim[3], and Kyungsoo Lee[1]

[1]Department of Earth and Environmental Sciences, Seoul National University, Seoul, 08826, Republic of Korea
[2]Institute for Data Innovation in Science, Seoul National University, Seoul, 08826, Republic of Korea
[3]Korea Polar Research Institute, Incheon, 21990, Republic of Korea

Correspondence to: Sang-Moo Lee (sangmoolee@snu.ac.kr)

Abstract. The decline of Arctic sea ice in the global warming era has received much attention as a contributing factor to the changes in the weather/climate in the Arctic and beyond. The coverage of Arctic sea ice (i.e., sea ice concentration (SIC)) has been monitored since 1972 using satellite passive microwave (PMW) measurements because of their extensive coverage and all-weather capability. However, the fundamental basis of algorithms for estimating SIC has not improved much since the early days due to the lack of reference SIC data, leading to discrepancies between existing PMW SIC algorithms. To overcome this issue, this study aims to construct data records of reference SIC over Arctic sea ice using 30 m resolution imagery from the Operational Land Imager (OLI) onboard Landsat-8. In order to collect relatively bright and clear scenes, thresholds of solar elevation > 15° and cloud cover < 10% were applied in this study. Clouds in each Landsat-8 scene were masked using the cloud masking array provided in Landsat data. Due to the poor accuracy of the cloud masking array over ice-covered surface types, an additional step of visually inspecting the state of cloud mask using the true-~~color~~colour image was designated in this study. Each Landsat-8 scene was sorted into four categories depending on the state of cloud mask. Normalized Difference Snow Index and OLI band 5 reflectivity were used to differentiate between ice and open water within each selected Landsat-8 pixel. The classified data were projected onto a 6.25 km polar stereographic grid, and SIC for each grid cell was obtained by counting ice-classified pixels within the grid. SIC was only computed for grid cells with more than 99% of its area covered with Landsat-8 pixels to limit the uncertainty in SIC arising from grids that are not fully concentrated with Landsat-8 pixels. Uncertainty in the produced SIC was 1~4%, inferred using the Gaussian error propagation method. Out of 15,286 collected Landsat-8 images, 14,297 images were translated into SIC maps, and a total of 2,934,399 Landsat-8 SIC grid cells were generated. Evaluation of Landsat-8 SIC with SIC from ice charts revealed a good linear relationship (correlation coefficient of 0.96) between the two products as well as a mean negative bias which fell within the uncertainty range of Landsat-8 SIC. SIC based on Landsat-8 can be used as reference SIC to evaluate existing SIC products and thus one can improve SIC products as well as the use of the improved SIC for other applications such as data assimilation and retrieval studies. The vast amount of Landsat-8 SIC generated in this study may also be used to train deep learning models for estimation of Arctic SIC coverage. The Landsat-8 SIC dataset can be publicly accessed at

1 Introduction

Since space-borne multi-channel passive microwave (PMW) observations have been available, areal information of Arctic sea ice has been successfully monitored. During the past four decades, these observations have shown that sea ice extent (SIE) which is defined as the area of ocean where ~~at least~~ sea ice concentration (SIC) is greater than 15% has been rapidly declining at a statistically significant negative trend of -12.7% per decade observed in September (Cavalieri and Parkinson, 2012; Meier et al., 2014; Meier and Stroeve, 2022). In the global warming era, the change in Arctic sea ice area is considered as a key indicator of climate change and this is closely associated with the changes in the Arctic local weather as well as the weather at mid-latitudes (Honda et al., 2009; Jaiser et al., 2012; Kim et al., 2014; Trewin et al., 2021; Shi et al., 2023). Therefore, obtaining precise observations of Arctic SIC is essential in order to diagnose the influences of climate change on Arctic sea ice.

As mentioned above, the spatial coverage of Arctic sea ice (i.e., SIC) has been monitored using satellite PMW measurements with their extensive spatial coverage over the Arctic and all-weather capability. Beginning with the launch of the Electrically Scanning Microwave Radiometer (ESMR) onboard Nimbus-5 in 1972 (Parkinson et al., 1987), successive launches of PMW sensors has allowed for the construction of comprehensive and continuous records of Arctic SIC. The Scanning Multi channel Microwave Radiometer (SMMR), launched in 1978, was equipped with five channels (6.6, 10.7, 18.0, 21.0, and 37.0 GHz) in first two Stokes' polarizations. The emergence of multi-channel PMW radiometers has led to the development of various SIC retrieval methods which were more accurate relative to the previous methods used for ESMR which only had a single channel at 19 GHz. Addition of ~~a~~ the near 90 GHz high frequency channels in the PMW sensors following SMMR, which include the Special Sensor Microwave Imager (SSM/I), the Special Sensor Microwave Imager/Sounder (SSMIS), the Advanced Microwave Scanning Radiometer - Earth Observing System (AMSR-E), and the AMSR2, has allowed for spatially- enhanced SIC retrievals.

~~There have been developed v~~Various PMW SIC algorithms have been developed, which estimate SIC based on combinations of brightness temperatures (TB) at various channels and empirically -derived tie-points. One of the best-known algorithms is the Bootstrap (BT) algorithm first suggested by Comiso et al. (1984). In BT algorithm, vertically polarized TBs at 19 and 37 GHz and horizontally polarized TB at 37 GHz are utilized to determine reference TBs (i.e., tie-points) over open water and fully-concentrated ice, which can be used to convert the observed TB to SIC with the following equation:

$$\text{SIC} = \frac{T_B - T_O}{T_I - T_O} \tag{1}$$

where T_B is the satellite-measured TB and T_O and T_I are the empirically -determined open water and ice tie-points, respectively. Tie-points in the BT algorithm are updated on a daily basis and acquired separately for the Arctic and the

Antarctic in order to accommodate the variation of TB fields with respect to time and hemisphere (Comiso, 1995). Another well-known algorithm is the NASA Team (NT) algorithm which utilizes horizontally polarized TB at 19 GHz and vertically polarized TBs at 19 and 37 GHz to calculate the polarization ratio (PR) and the spectral gradient ratio (GR), which are used to determine a set of tie-points to estimate SIC and determine the surface type from a combination of open water, first-year ice, and multi-year ice (Cavalieri et al., 1984). The other is the Arctic Radiation and Turbulence Interaction Study (ARTIST) Sea Ice (ASI) algorithm, which was developed by Kaleschke et al. (2001), in order to exploit the high resolution of the near-90 GHz channels. The ASI algorithm estimates SIC using the tie-points derived from the polarization difference calculated in the near-90 GHz channels. The high sensitivity of the near-90 GHz channels to atmospheric effects is compensated for by the usage of weather filters, which are applied using the GR thresholds suggested by Gloersen and Cavalieri (1986) and Cavalieri et al. (1995), and by setting SIC to zero in areas where BT SICs are zero (Spreen et al., 2008).

However, ~~there exist~~ discrepancies exist among various PMW SIC records retrieved from different algorithms owing to the different channel combinations, tie-points, and weather filters used in each algorithm (Comiso et al., 1997; Anderson et al., 2007). Due to the lack of reference SIC data with satisfactory temporal and spatial coverages, these disagreements have been studied mainly through inter-comparison of different PMW SICs and ensemble methods which compare individual SIC products to their averaged value. For instance, Ivanova et al. (2014) reported that different PMW SIC products showed a maximum difference of up to 1.3×10^6 km^2 in area and 0.6×10^6 km^2 in extent over the Arctic and larger deviations during the summer due to the differing sensitivity of retrieval algorithms to the presence of melt ponds and the associated emissivity change ~~ice/water mixtures~~, as well as a humid atmosphere (Ivanova et al., 2014; Comiso et al., 2017; Horvat et al., 2023). Although these inter-comparison approaches can provide valuable assessments of the consistency of PMW SIC products from sub-seasonal to climatological timescales, it is noted that there is a limitation to providing a quantitative assessment of PMW SIC products.

In order to make such quantitative assessments, it is essential to have independent SIC data that can be used as a reference. Spaceborne sensors with visible (VIS) to infrared (IR) channels, such as the Moderate Resolution Imaging Spectroradiometer (MODIS) and the sensors onboard the Landsat series, have been used to generate reference SIC due to their finer spatial resolutions than PMW sensors (Markus et al., 2002, Cavalieri et al., 2006, 2010; Rösel and Kaleschke, 2011; Kern et al., 2022; Tanaka and Lu, 2023; Song and Minnett, 2024). However, validation attempts using VIS/IR-based SIC as a reference have been limited to the usage of a small number of VIS/IR images, with the exception of Kern et al. (2022) which used a relatively large number of Landsat scenes (386 scenes) to generate a reference SIC. The dataset by Kern et al. (2022) is also utilized in this study for validation of the produced Landsat-8 SIC, and the results of the comparison are presented in Section 3.2. In addition to VIS/IR instruments, SIC observations from synthetic aperture radar (SAR) have also been used for PMW-based SIC validation purposes, but difficulties in obtaining an accurate and automated SIC map from SAR images result in the limited use of SAR images for validation purposes (Anderson et al., 2007; Park et al., 2017; Han and Kim, 2018; Tanaka and Lu, 2023).

Recently, efforts to leverage the advantages of both VIS/IR sensors and PMW sensors for retrieving SIC have been explored through data merging techniques. Ludwig et al. (2020) used a combination of MODIS and AMSR2 measurements to construct a high-resolution (1 km) and spatially continuous SIC data over pan-Arctic areas. This approach exploited the benefits of the 1 km resolution MODIS imagery while mitigating its inherent disadvantage of spatial discontinuity due to clouds by introducing the AMSR2 measurements. While the SIC dataset produced by Ludwig et al. (2020) is both high-resolution and covers pan-Arctic areas, due to the retrievals being reliant on the AMSR2 measurements, the product cannot be considered a fully independent reference data for PMW SIC validation. Therefore, it is still necessary to construct a dataset of Arctic SIC that is fully independent of PMW measurements.

In addition to this, recent applications of deep-learning (DL) models for estimating SIC have shown promising results. Karvonen (2017) trained a multi-layer perceptron (MLP) model using various combinations of PMW signals extracted from AMSR2 and SAR as the training inputs and SIC fields derived from the Finish Meteorological Institute ice charts as the reference. This MLP model produced improved SIC compared to the high-resolution ASI SIC. However, the data used to train the DL model suggested by Karvonen (2017) were limited to regions around the Baltic Sea and were only acquired during the winter of 2015-2016. Chi et al. (2019) proposed an estimation of Arctic SIC based on MLP model trained with raw AMSR2 TBs as the inputs and SIC derived from seventy-two MODIS images during 2016 as the reference, demonstrating that the DL-based SIC shows better performance than the widely used BT and ASI SICs. Since both studies used training datasets acquired during a limited time period but showed promising results of the use of DL techniques for SIC production, it is also desirable to construct a data record for reference SIC data with satisfactory temporal and spatial coverages.

Therefore, this study aims to construct a reference SIC dataset of satisfactory spatiotemporal extent, to allow for validation of various SIC products over pan-Arctic areas as well as to be used for DL training. To do this, a total of 14,297 Landsat-8 images over the three years (2020-2022) were translated into SIC maps in a 6.25 km polar stereographic grid, andgrid and catalogued into a sub-region of the Arctic Ocean.

The rest of this paper isremaining sections of this paper are organized as follows: Section 2 provides a detailed description of the Landsat-8 dataset, the land, sea ice region, coastal area masks, and the reference datasets used to evaluate the Landsat-8 SIC in this study. Section 3 describes the processing pipeline of a Landsat-8 image into a SIC dataset along with the uncertainty estimation. The resultant SIC product and its uncertainty are shown in Section 4. Possible errors in Landsat-8 SIC, evaluation of Landsat-8 SIC using existing SIC from ice charts, evaluation of Landsat-8 SIC over melt ponds, and qualitative assessment of two PMW SIC products using SIC from Landsat-8 as a reference are discussed in Section 5. Section 6 provides the data availability statement, and Section 7 gives the summary and conclusion of this research.

2 Used Data

2.1 Landsat-8 OLI-TIRS Collection 2 Level 1 Products

In this study, reflectivities measured by the Operational Land Imager (OLI) onboard Landsat-8, which is a polar orbiting satellite with orbit inclination of 98.2° and a repeat cycle of 16 days (Zanter, 2019), were used to retrieve SICs over pan-Arctic areas. The OLI sensor has a swath width of 185 km, measuring radiances at eight bands from VIS to short-wave IR (SWIR) with a spatial resolution of 30 m. It should be noted that areas with a latitude higher than 82°N in the northern hemisphere are not measured by Landsat-8 (i.e., the hatched area in Fig. 1) due to the orbit inclination of Landsat-8 and the relatively narrow swath width of the OLI. The Landsat-8 Collection 2 Level 1 product used in this study contains eleven spectral band images (nine bands from the OLI and two bands from the Thermal Infrared Sensor) provided in GeoTIFF format, two quality assessment bands containing masking information for clouds, cloud shadows, cirrus, fill values, and radiometric saturation. To calculate the SIC, the OLI-measured reflectivities at near-infrared (NIR) band 5 and SWIR band 6 (used in the Normalized Difference Snow Index) were used in this study. It is worth noting that the methods developed in this study (described in Section 3) utilize the NIR and SWIR bands for SIC retrieval and are therefore applicable to a wider range of high-resolution sensors that observe at similar bands, including the Multi-Spectral Instrument (MSI) onboard Sentinel-2. However, due to the more robust cloud mask performance of the Landsat-8 product, in this study, the Landsat-8 Collection 2 Level 1 product was selected to be used for the production of reference SIC data (Zhu et al., 2015; Tarrio et al., 2020).

For the period of Jan. 2020 – Dec. 2022, Landsat-8 Collection 2 Level 1 product and the corresponding true-color images were downloaded from the United States Geological Survey Earth Explorer (https://earthexplorer.usgs.gov/). To circumvent the influences of cloud contamination and low solar elevation angle on SIC calculation, which hampers accurate classification of ice and open water, only Landsat-8 images with less than 10% cloud cover (based on fractional cloud masked area from the quality assessment band of Landsat-8) during daytime cloud cover (solar elevation higher than 15°) were collected. While the threshold of 0% cloud cover would ensure the acquisition of the least cloudy scenes, this also results in the loss of a considerable number of Landsat-8 scenes that contain clear-sky portions (see Fig. S1 and Table S1 in the supplements for the number of available Landsat-8 scenes subject to different threshold values of cloud cover). Therefore, the threshold value for cloud cover was relaxed to 10% during the acquisition of Landsat-8 images. Since VIS measurements were are not available during polar night-time, the Landsat-8 data between early December to January were not collected. It should also be noted that, due to the sun-synchronous orbit of Landsat-8 along with the narrow swath width of OLI, Landsat-8 does not measure areas where latitude is higher than 82°N. A total of 15,286 images were collected and sorted into twelve sub-regions of the pan-Arctic area for the calculation of SIC. In the case of a Landsat-8 image that observed across more than one sub-region, the image was sampled repeatedly for each sub-region. Footprints of the collected Landsat-8 images are displayed in Fig. 1 and the number and the temporal availability of the collected images for each area are listed in Table 1.

Sub-rRegion	Baffin Bay	Barents Sea	Beaufort Sea	Bering Sea	Canadian A.	Central Arctic
Count	2476	672	451	699	3174	2343
2020	Jan. 13-Nov. 30	Feb. 27-Oct. 7	Mar. 6-Sep. 17	Jan. 19-Dec. 3	Feb. 29-Oct. 2	Mar. 23-Sep. 2
2021	Feb. 16-Nov. 26	Feb. 22-Oct. 5	Mar. 7-Sep. 30	Jan. 13-Dec. 3	Mar. 1-Sep. 28	Mar. 24-Sep. 11
2022	Jan. 25-Dec. 6	Mar. 4-Sep. 29	Mar. 4-Oct. 4	Jan. 24-Nov. 16	Mar. 3-Oct. 10	Mar. 25-Sep. 13
Sub-rRegion	Chukchi Sea	E. Greenland	E. Siberian	Hudson Bay	Kara Sea	Laptev Sea
Count	427	1468	546	1485	899	646
2020	Feb. 27-Oct. 10	Feb. 18-Oct. 31	Mar. 4-Sep. 21	Jan. 13-Nov. 14	Mar. 6-Sep. 16	Mar. 10-Sep. 27
2021	Feb. 25-Oct. 11	Feb. 25-Oct. 27	Mar. 7-Oct. 2	Jan. 17-Nov. 6	Mar. 7-Sep. 17	Mar. 15-Sep. 13
2022	Mar. 6-Oct. 14	Mar. 4-Oct. 30	Mar. 10-Sep. 7	Jan. 18-Oct. 29	Mar. 5- Sep. 29	Mar. 12-Sep. 6

Table 1: The number of Landsat-8 images collected in this study and the available period for each sub-region of the pan-Arctic areas

160
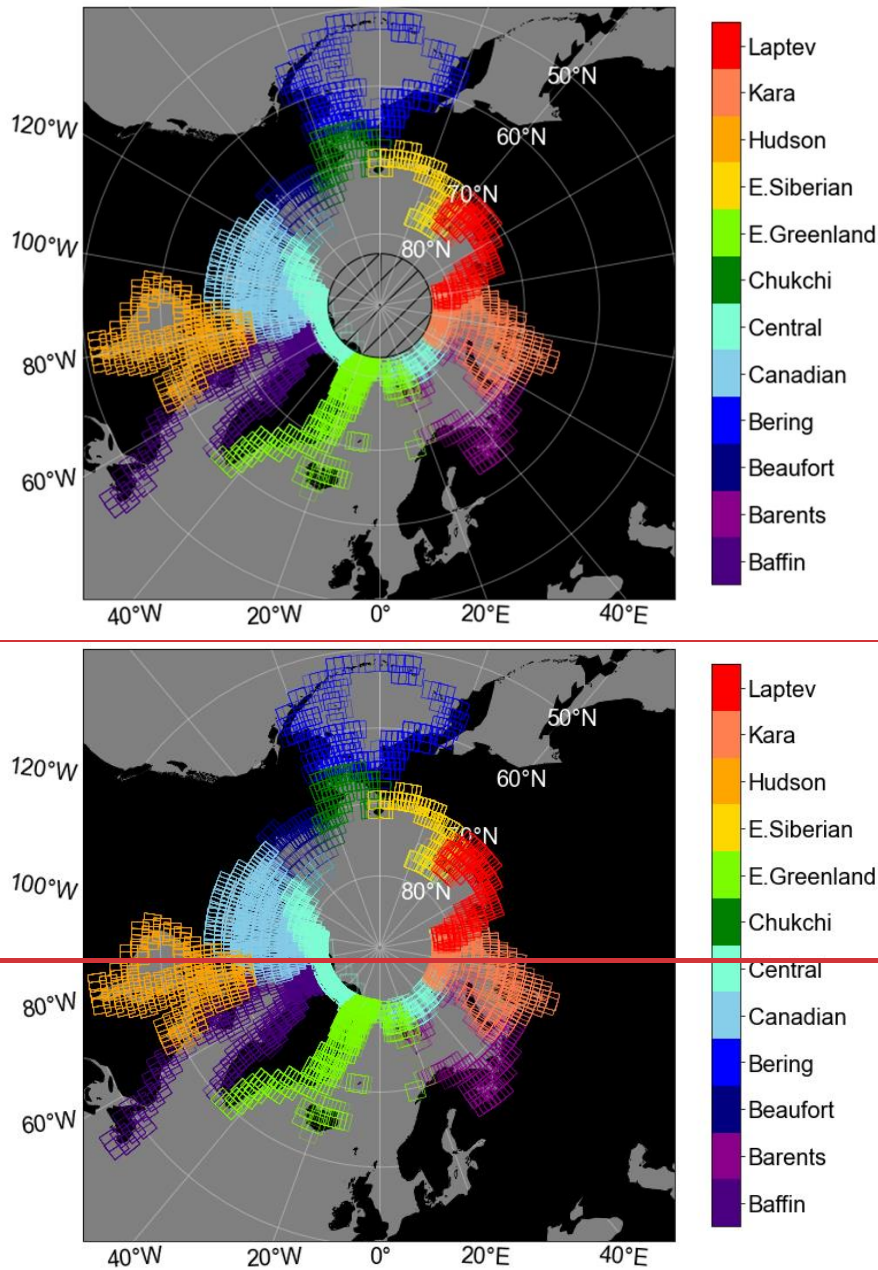
Figure 1: Footprints of the collected Landsat-8 images over each ~~sub-~~region ~~ofover~~ the pan-Arctic areas during the period of Jan. 2020 – Dec. 2022. The hatched region denotes the areas unmeasured by Landsat-8 due to its orbital inclination (i.e., pole hole). The regions of the pan-Arctic areas were distinguished using the region mask provided by Meier and Stewart (2023). The map projection is NSIDC Sea Ice Polar Stereographic North (EPSG: 3413) and the map was plotted using Python.~~the study period.~~

2.2 Land and Sea Ice Region Masks

170 ~~Sub r~~Regions of the Arctic Ocean were distinguished using the National Snow and Ice Data Center (NSIDC) 'Arctic and Antarctic Regional Masks for Sea Ice and Related Data Products, Version 1' data (Meier and Stewart, 2023), which divides the Arctic Ocean into nineteen different ~~sub-~~regions with 6.25, 12.5, and 25 km resolution polar stereographic (PSR) grids. In addition, this product provides surface masking information to differentiate between ocean areas and non-ocean areas such as land, freshwater, land ice, ice shelf, and disconnected ocean. The flag values for the Arctic Ocean ~~sub-~~regions and

175 the different surface types can be found in the product user guide (Meier and Stewart, 2023). Amongst the ~~sub-~~regions, twelve regions (i.e., Baffin Bay and Labrador Seas, Barents Sea, Beaufort Sea, Bering Sea, Canadian Archipelago, Central Arctic, Chukchi Sea, East Greenland Sea, East Siberian Sea, Hudson Bay, Kara Sea, and Laptev Sea; Fig. 2) were selected to generate Landsat-8 based SICs, because the above twelve regions have climatologically meaningful sea ice extent.

180
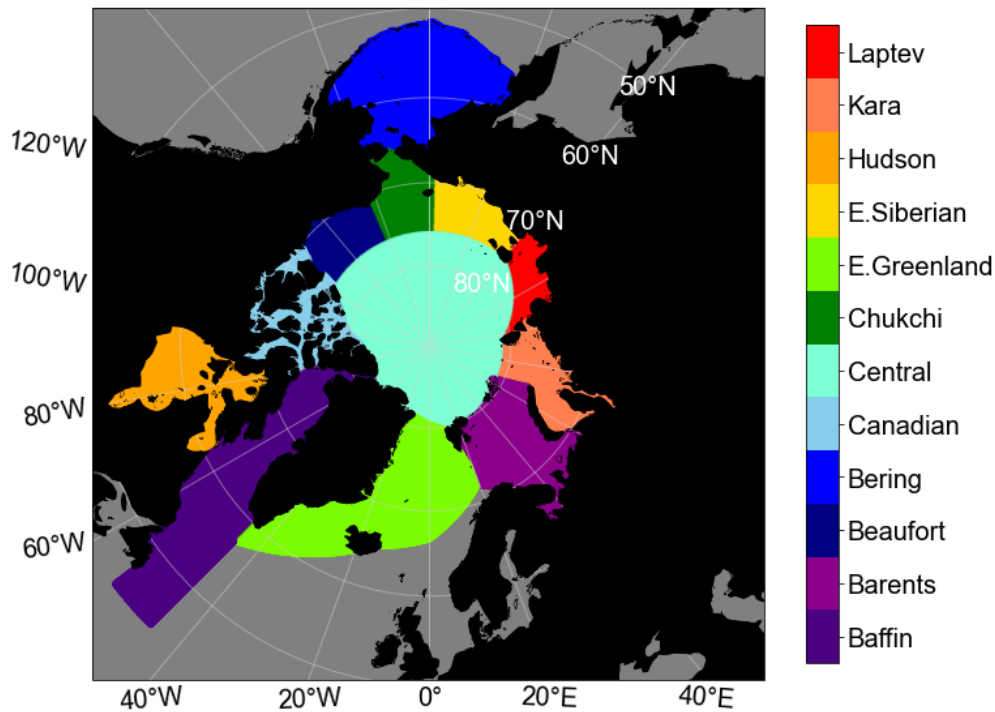
Figure 2: Geographic distribution of the designated ~~sub-~~regions of the Arctic Ocean, based on NSIDC Sea Ice Region Mask data (Meier and Stewart, 2023). The map projection is NSIDC Sea Ice Polar Stereographic North (EPSG: 3413) and the map was plotted using Python.

185

2.3 Ice/Water Classified Landsat-8 Images

The performance of ice and open water classification (later described in Ssection 3.2), in this study, was evaluated using ice-water classification data from the 'Land surface type over water from supervised classification of surface broadband albedo estimates' (Kern, 2021; Kern et al., 2022). This dataset contains ice/water classification estimates using broadband albedo values from the Landsat series (i.e., bandwidth weighted mean albedo from Landsat-8-measured reflectivities at bands 3, 4, and 5), where each pixel in a scene is classified into open water, thin or bare ice, and thick or snow-covered ice based on supervised classification. In ourthis study, the two ice categories (i.e., one for thin or bare ice and the other for thick or snow-covered ice) were considered as a same ice category due to the higher ambiguities in the discrimination among different ice types relative to the discrimination between ice and open water (Kern et al., 2022). In order to evaluate the ice and water classification method (see Section 3.2) suggested by ourthis study we processed Landsat-8 reflectance from six clear-sky scenes that Kern (2021) had classified, and then compared results. The result of the comparison is presented in Section 3.2 and the , 6 classified scenes (Kern, 2021) under clear sky condition of which scene location and time of the Landsat-8 scenes that were used in the evaluation are provided in the supplements Fig. S21 and Table S21. and the corresponding Landsat-8 reflectivities were used.

2.4 Ice Chart Data

Ice charts provide SIC intervals over the Arctic obtained by manual interpretation of satellite images from various sensors such as SAR, MODIS, and the Advanced Very High Resolution Radiometer (AVHRR). In this study, operational ice charts from Norwegian Meteorological Institute (MET Norway), which provide SIC maps in PSR grid with nominal resolution of 1 km, were used to evaluate the performance of the produced Landsat-8 SIC. Each grid in the ice chart contains the classified six SIC values (5, 20, 50, 75, 95, and 100%), which represent the ice concentration intervals defined by the World Meteorological Organization (WMO) (Table A1). The ice charts are provided on a daily basis and cover the spatial domain of approximately 80°W-80°E, 60°N-85°N, which overlap with the sub-regions of Barents Sea, Central Arctic, East Greenland Sea, and Kara Sea defined in Ssection 2.2. It is noted that SIC in ice charts are based on the interpretation of multiple satellite imageries by ice analysts, and therefore contain high uncertainties, which are reflected by the wide ice concentration intervals designated for each of the six SIC values (Table A1). Even with such high uncertainties, SIC from ice charts have been widely selected as reference data in SIC product validation studies, because they can be used to provide quantitative information about the observed ice coverage (Agnew and Howell, 2010; Ivanova et al., 2015; Karvonen, 2017). In this study, two-years (2021 and 2022) of ice charts were collected among which 222 ice charts that have spatial overlap with the coverage of Landsat-8 SIC and have time difference of less than 1 hour with the Landsat-8 scene were used for evaluation of the produced Landsat-8 SIC (see Table S32 in the supplements for the list of ice charts and Landsat-8 files used in the evaluation of the produced Landsat-8 SIC).

2.5 Melt Pond Fraction Data

Melt ponds are formed from the surface melting of sea ice and are known to exist in preponderance over the Arctic during the melting season (Untersteiner, 1961; Fetterer and Untersteiner, 1998; Rösel et al., 2012). In the VIS/IR ranges, melt ponds typically exhibit lower spectral reflectivities relative to dry sea ice (Perovich, 1996; Malinka et al., 2018), and therefore may introduce errors in SIC estimated from VIS/IR observations because the optical characteristics of melt ponds may not be differentiated from those of open ocean. In order to test the sensitivity of Landsat-8 SICs to the existence of melt ponds, in this study, a melt pond fraction (i.e., the fractional areal coverage of melt ponds over sea ice; MPF) dataset estimated from clear-sky Sentinel-2 satellite imagery was introduced (Niehaus and Spreen, 2022; Niehaus et al., 2023). This dataset also contains an open water mask (OW mask), which is a binary classification mask of each pixel in a Sentinel-2 scene into ice and open water. This dataset is available from 2017 to 2021 for the Arctic melting season (i.e., June, July, and August). In this study, each MPF dataset was tested for spatiotemporal overlap (time difference of less than 3 hours) with the coverage of Landsat-8 SIC. The total of six MPF datasets were found to be overlapping with the coverage of Landsat-8 SIC and thus available for use in the evaluation. the total of six MPF datasets that are spatially overlapped with the coverage of Landsat-8 SIC dataset and have time difference of less than 3 hours with the Landsat-8 scene were selected for evaluation of variation in Landsat-8 SIC due to melt pond presence. The list of availableselected MPF datasets and the corresponding Landsat-8 scenes can be sceneseen in Table S43 of the supplements.

3 Method

Figure 3 shows the processing pipeline of a Level 1 Landsat-8 image into a SIC product based on 6.25 km resolution PSR grid. Details of each process are explained as the following sub-sections.
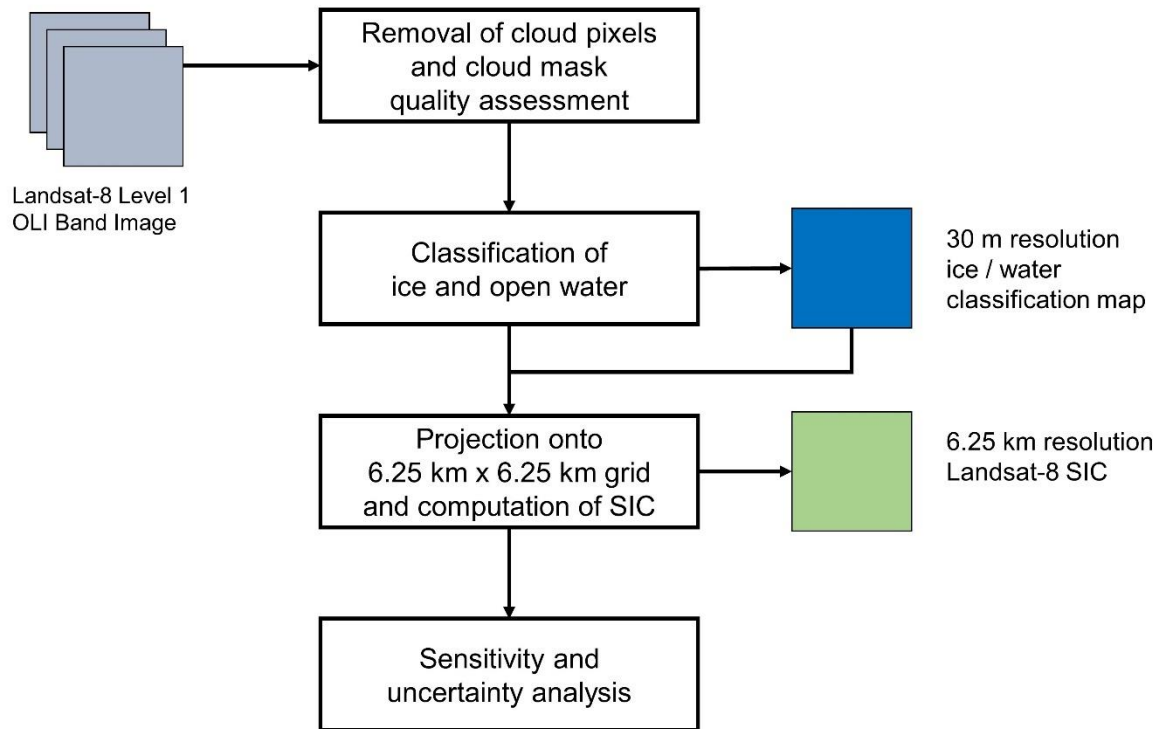
Figure 3: Processing pipeline of Level 1 Landsat-8 OLI images into SICs with 6.25 km resolution.

3.1 Removal of Cloud Pixels and Cloud Mask Quality Assessment

245   Satellite observations of surface properties from the VIS and NIR channels are hindered by the presence of clouds. Therefore, it is important to filter the presence of clouds prior to the SIC data production. In this study, clouds and cloud shadows within each Landsat-8 scene were masked using the masking array constructed from the quality assessment band of each Landsat-8 Level 1 product, which is generated by the C Function of Mask (CFMask) (Zhu and Woodcock, 2012). CFMask is a cloud detection algorithm that provides masking information for clouds, cloud shadows, and cirrus. Confidence scores are

250   also given in three levels (i.e., low, medium, and high) for clouds and two levels (i.e., low and high) for cirrus. Confidence score for cloud shadows is not provided because cloud shadows are only derived from high confidence cloud pixels by using the geometric relationship between the position of the sun and high confidence cloud pixels (Zhu and Woodcock, 2012). Although the application of the lowest confidence scores in the removal of clouds and cirrus would ensure the lowest rate of false negatives (FN; cloud pixels that ~~were~~are mistaken as clear pixels) in cloud detection, the use of the lowest confidence

255   scores also result in the removal of a considerable number of sea ice pixels under clear sky (Foga et al, 2017). Therefore, it is important to select proper confidence scores to retain as many clear sky sea ice pixels as possible while minimizing the number of FN cases. In this study, pixels with medium and high confidence scores for clouds and for cirrus, respectively,

were discarded prior to Landsat-8 SIC production to avoid cloud and cirrus contamination. In addition, as suggested in Foga et al. (2017), dilated cloud pixels, which are clear pixels completely surrounded by cloud pixels, were also masked to prevent contamination by cloud edges where cloud detection uncertainty is high.

It is important to note that CFMask over ice-covered surface types has lower accuracy than other surface types (Foga et al., 2017; Qiu et al., 2019). Therefore, an additional step for cloud mask quality assessment is designated in this study. In this step, a visual inspection was performed by comparing the cloud mask array, which is constructed by masking cloud, cirrus, cloud shadow, and dilated cloud pixels, from each Landsat-8 image with the corresponding true-color image to identify the cases of FN, false positive (FP; clear pixels that ~~were~~are mistaken as cloud pixels), true negative (TN; clear pixels correctly detected as clear pixels), and true positive (TP; cloud pixels correctly detected as cloud pixels) pixels in the Landsat-8 image. From this additional step, Landsat-8 images were sorted into four categories depending on the assessed quality of cloud masking. Images with the existence of FN cloud pixels in the cloud mask array, which indicate the underestimated cloud cover, were labelled as Category 1 (C1). Images dominated by FP cloud pixels, which occur in cases of the overestimated cloud cover, were tagged as C2. Images dominated by TP cloud pixels, which correspond to correctly estimated cloud cover for cloudy sky, were labelled as C3. Images dominated by TN cloud pixels, which correctly estimate clear sky, were labelled as C4. For images under C2 (i.e., overestimated cloud coverages with medium confidence scores for clouds and high confidence scores for cirrus), the cloud mask array was regenerated with a higher confidence score (high confidence clouds and cirrus) and visually inspected against the true-color image to determine the adequacy of the higher confidence score cloud mask as follows: If any FN cloud pixels were present in the higher confidence cloud mask, the original confidence score (i.e., medium for clouds and high for cirrus) was used to mask the clouds. Further details of the visual screening step are provided in Appendix B.

In this study, for Landsat-8 images that were labelled as C2, C3, and C4, Landsat-8 pixels that remain after the application of CFMask were assumed to be clear sky pixels (i.e., "clear pixel assumption"). However, for Landsat-8 images labelled as C1, the "clear pixel assumption" is not valid because C1 category underestimates clouds by CFMask according to the visual inspection step, which implies that the associated error due to the underestimated cloud cover in SIC calculation is expected. Therefore, possible error from the presence of unmasked cloud pixels in C1 is further evaluated in ~~S~~section 5.1. The number of Landsat-8 images under the four categories over the twelve ~~sub~~ regions is provided in Table 2, and the assessed cloud mask quality (i.e., C1, C2, C3, and C4) for each Landsat-8 image is provided in the variable under the name 'cloud_contamination_category' in the produced Landsat-8 SIC dataset in order to allow for quality control of the data in its usage.

Category	C1[a]	C2[b]	C3[c]	C4[d]
Baffin Bay	826	80	907	663
Barents Sea	271	10	265	126

Beaufort Sea	215	27	111	98
Bering Sea	209	24	264	202
Canadian A.	1,573	176	854	571
Central Arctic	1,165	42	705	431
Chukchi Sea	154	30	134	109
E. Greenland	767	29	369	303
E. Siberian	230	36	145	135
Hudson Bay	619	116	351	399
Kara Sea	490	34	245	130
Laptev Sea	328	23	165	130

[a]underestimated cloud cover
[b]overestimated cloud cover
[c]correctly estimated cloud cover for cloudy sky
[d]correctly estimated cloud cover for clear sky

Table 2: The number of Landsat-8 images for the four cloud mask categories (i.e., C1: underestimated cloud cover, C2: overestimated cloud cover, C3: correctly estimated cloud cover for cloudy sky, and C4: correctly estimated cloud cover for clear sky) over the twelve ~~sub~~-**regions** ~~of~~**over the Arctic Ocean during the** ~~study period~~**periods of Jan. 2020 – Dec. 2022.**

3.2 Ice and Open Water Classification

Classification of a Landsat-8 pixel ~~into~~as ice ~~and~~or open water was performed by applying thresholds to the top-of-atmosphere (TOA) reflectivity at band 5 (NIR) and the normalized difference snow index (NDSI). ~~In order t~~To do this, first, the reflectivity of a Landsat-8 pixel, which is stored as a 16-bit digital number in the Landsat-8 Collection 2 Level 1 dataset, was scaled to TOA reflectivity using the following equation (Zanter, 2019):

$$\rho_\lambda = \frac{M_\rho Q_{DN} + A_\rho}{\sin(\theta_{SE})} \tag{2}$$

where M_ρ, and A_ρ are the multiplicative and additive scale factors, θ_{SE} is the solar elevation angle, and Q_{DN} is the TOA reflectivity of the Landsat-8 pixel in 16-bit digital number format.

Then, the NDSI was calculated from the scaled reflectivities as follows:

$$\text{NDSI} = \frac{\rho_5 - \rho_6}{\rho_5 + \rho_6} \tag{3}$$

where ρ_5 and ρ_6 are the TOA reflectivities at bands 5 (NIR) and 6 (SWIR) of the OLI sensor, respectively.

The steps for differentiating ice and open water pixels and for removing possible cloud pixels are shown in Fig. 4. The first is the ρ_5 criterion in order to detect open water pixels, which has lower reflectivity at band 5 compared to that over ice or cloud pixels. The next step is the NDSI criterion in order for detecting ice pixels, which has higher NDSI than cloud pixels, due to higher reflectivity of ice at band 5 and lower reflectivity of ice at band 6, compared to the cloud reflectivities (Hall et

al., 1995; Riggs et al., 1996, 1999). The NDSI criterion for the separation of ice and cloud pixels was kept in order to reinforce cloud removal process in addition to CFMask explained in Ssection 3.1. In this study, the thresholds for ρ_5 and NDSI were selected as 0.08 and 0.45, respectively (Liu et al., 2016; Tanaka and Lu, 2023).

315 As mentioned in Ssection 3.1, the "clear pixel assumption" was applied during the classification of Landsat-8 images labelled C2, C3, and C4. Accordingly, the performance of classification steps based on ρ_5 and NDSI with the selected thresholds was evaluated over clear sky pixels using the surface classification data from Landsat-8 images (Kern, 2021) mentioned in Ssection 2.3 as reference data. The values of ρ_5 and NDSI were collected separately over open water and ice pixels in the reference data and classification over the collected pixels was performed following the procedure in Fig. 4.

320 From the distributions of ice and open water pixels in the two-dimensional histogram between NDSI (x-axis) and ρ_5 (y-axis) in Fig. CB1, it can be seen that ice and open water are well differentiated by the selected threshold values of ρ_5 and NDSI, respectively (Fig. CB1). In addition, for quantitative assessment of the performance of ice and open water classification, the recall was computed for the open water and ice categories using the classification result summarized in Table 3 and Eq 4.

$$RC_{X \text{ as } X} = \frac{N_{X \text{ as } X}}{N_{X \text{ as } X} + N_{X \text{ as } \sim X}} \tag{4}$$

325 where $N_{X \text{ as } X}$ and $N_{X \text{ as } \sim X}$ are the number of pixels in category X classified as X (TP) and the number of pixels in category X classified as not X (FN), respectively. With the designated thresholds the recall was found to be 98.94% for water and 97.67% for ice. FN classifications of ice into open water can cause negatively biased SIC. The bias due to such classification error was estimated to be 2.33% from the percentage of the number of ice pixels that were classified as open water in Table 3. Conversely, FN classification of open water into ice can cause positively biased SIC, which was estimated to be 1.06% from

330 the value in Table 3. Misclassification of ice or open water pixels into cloud pixels from the application of the NDSI threshold rarely occurred for both ice and open water categories. Thus, it can be concluded that the classification method used in this study is accurate over clear sky pixels. Furthermore, the error from ice/water classification over clear sky is within the uncertainty range of Landsat-8 SIC which is discussed in Ssection 4.3.

This classification result may not be applicable for Landsat-8 images tagged C1 (i.e., underestimated cloud cover), because

335 as mentioned in Ssection 3.1, such images aredo not consisted solely of clear sky pixels, but contain undetected cloud pixels by CFMask. Therefore, for Landsat-8 images labelled C1, in order to understand possible errors in SIC calculation from the designated classification method, it is necessary to evaluate the performance of classification over the undetected cloud pixels. This is discussed further in Ssection 5.1.
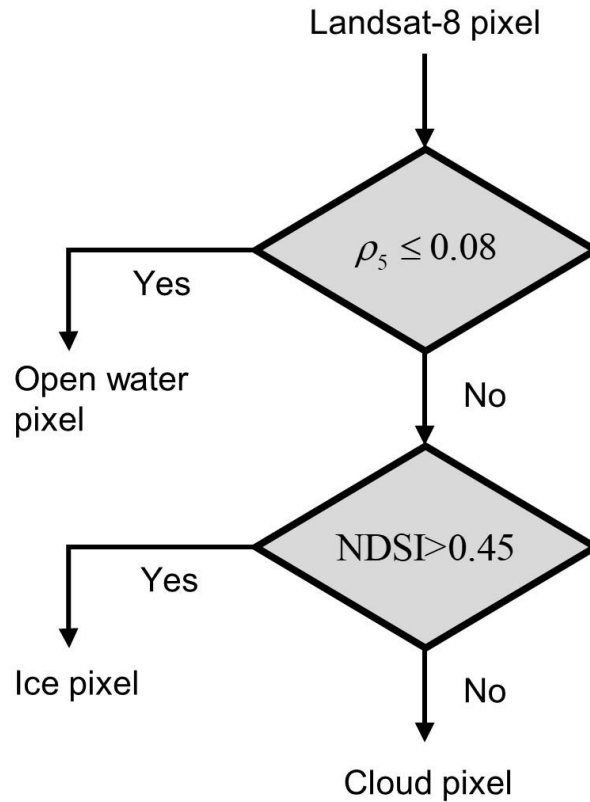
Figure 4: The process for separating ice, open water, and possible unmasked clouds using ρ_5 and NDSI criterion, where ρ_5 and NDSI are the TOA reflectivity at band 5 of the OLI sensor and the Normalized Difference Snow Index, respectively.

Reference \ Classified	Open water	Ice	Cloud
Open water	13,271,877 (98.94%)	141,582 (1.06%)	19 (0.00%)
Ice	747,481 (2.33%)	31,353,954 (97.67%)	336 (0.00%)

Table 3: The number of classified pixels for open water, ice, and cloud from the suggested method and surface classification reference data (Kern, 2021). The original categories in the reference data are shown in the rows, and the classified categories from the method in Fig. 4 are shown in the columns. The values inside the parentheses indicate the percentage of pixels from the original category that are classified into open water, ice, and cloud.

350 **3.3 Projection and Computation of SIC**

After the ice and open water classification for the selected Landsat-8 pixels, the classified pixels were projected onto the target grid system of the NSIDC Polar Stereographic grid with 6.25 km resolution. The number of ice and open water pixels within each 6.25 km × 6.25 km grid cell was used to compute SIC for the grid cell according to,

$$SIC = \frac{N_{ice}}{N_{ice} + N_{water}} \times 100 \, (\%) \tag{5}$$

355 where N_{ice} and N_{water} are the number of Landsat-8 pixels classified as ice and water within each 6.25 km × 6.25 km grid cell, respectively. It is noted that some of the grid cells with 6.25 km resolution are not ~~fully concentrated~~entirely filled by Landsat-8 pixels at the edges of a Landsat-8 image and/or near cloud masked regions. In this study, this kind of grid cell is referred to as 'partially-covered grid cell'. Therefore, SIC computed in such a grid cell is unlikely to be representative of the actual ice coverage over the area covered by the grid cell. To avoid this caveat, a minimum threshold in the number of 360 Landsat-8 pixels for a single 6.25 km × 6.25 km grid cell ($N_{critical}$) was applied prior to the computation of SIC. In this study, a specific value of $N_{critical}$ was introduced as the minimum threshold, which is discussed in the following subsection.

3.4 Sensitivity Test and Uncertainty Analysis

The sensitivity of Landsat-8 SIC to the prescribed thresholds of ρ_5 and NDSI was investigated for each cloud contamination 365 category. In doing so, for each of the four cloud contamination categories (i.e., C1, C2, C3, and C4), ten scenes were randomly sampled over ~~each~~all twelve ~~sub-~~regions (Fig. 2), and thus 120 scenes were used per each cloud contamination category for sensitivity test (see Table S~~5~~4 in the supplements for the full list of scenes used for sensitivity test). SIC over the selected scenes were calculated using Eq. 5 based on classification results with NDSI and ρ_5 thresholds perturbed by their uncertainties. Values of 0.015 and 0.016 were assigned as the uncertainties of ρ_5 and ρ_6, respectively, followed by Pinto et al. 370 (2020) which provides the root mean squared differences of the Landsat-8 TOA reflectivities and in situ observed reflectivities at bands 5 and 6. The uncertainty of NDSI was calculated using the Gaussian error propagation method, which can be written for NDSI as:

$$\sigma_{NDSI}^2 = \left(\frac{\partial NDSI}{\partial \rho_5}\right)^2 \sigma_{\rho_5}^2 + \left(\frac{\partial NDSI}{\partial \rho_6}\right)^2 \sigma_{\rho_6}^2 \tag{6}$$

where σ_{ρ_5} and σ_{ρ_6} are the uncertainties of Landsat-8 TOA reflectivities at bands 5 and 6, respectively. Substituting Eq. 3 375 for NDSI in Eq. 6, the analytical form of the uncertainty in NDSI can be expressed as the following:

$$\sigma_{NDSI}^2 = \frac{4\rho_6^2}{(\rho_5 + \rho_6)^4} \sigma_{\rho_5}^2 + \frac{4\rho_5^2}{(\rho_5 + \rho_6)^4} \sigma_{\rho_6}^2 \tag{7}$$

From Eq. 7 with $\sigma_{\rho_5} = 0.015$ and $\sigma_{\rho_6} = 0.016$, a value of 0.05 was assigned as the uncertainty of NDSI which is the median value of σ_{NDSI} computed over 480 randomly selected Landsat-8 scenes. For the four cloud contamination categories, mean values of SICs calculated with the perturbed thresholds of 0.45±0.05 and 0.08±0.015 for the NDSI and ρ_5, respectively,

380 are provided in Fig. 5. With the perturbation of ±0.015 for ρ_5 threshold, mean SICs from C1, C2, C3, and C4 vary by ∓0.641%, ∓0.495%, ∓0.665%, and ∓0.402%, respectively (blue lines in Fig. 5). With perturbation of ±0.05 for NDSI threshold, mean SIC from C1, C2, C3, and C4 varied by ∓0.111%, ∓0.002%, ∓0.007%, and ∓0.002%, respectively (red lines in Fig. 5). The calculated SICs are more sensitive to the ρ_5 threshold relative to the NDSI threshold because the ρ_5 threshold is responsible for separating open water and ice. It is noted that sensitivity of SICs to the NDSI threshold is two-

385 orders of magnitude higher for scenes labelled C1 than for C2, C3, and C4. The very low sensitivity of SICs to the NDSI threshold for scenes labelled C2, C3, and C4 infers that cloud pixels in such scenes had been successfully masked by CFMask prior to the ice/water classification described in Ssection 3.2. However, relatively higher sensitivity of SICs to the NDSI threshold for scenes under C1 infers that undetected cloud pixels had remained after the application of CFMask and that such cloud pixels had been further removed by the NDSI threshold.

390 Gaussian error propagation was also used to estimate the uncertainty of Landsat-8 SIC according to:

$$\sigma_{\text{SIC}}^2 = \left(\frac{\partial \text{SIC}}{\partial \text{NDSI}} \right)^2 \sigma_{\text{NDSI}}^2 + \left(\frac{\partial \text{SIC}}{\partial \rho_5} \right)^2 \sigma_{\rho_5}^2 \ (\%) \tag{8}$$

where σ_x and $\dfrac{\partial \text{SIC}}{\partial x}$ are the uncertainty of x and the sensitivity of SIC to x, respectively. The sensitivities for the two variables (i.e., ρ_5 and NDSI) were computed numerically from the mean SIC variation observed in sensitivity test (see Tables S65, S76, S87, and S98 in the supplementary for the computed values of sensitivity). In addition, in order to check the

395 relative contribution of each variable to the overall uncertainty in SIC, a contribution factor (CF_x) was defined and calculated for the two variables as the following:

$$\text{CF}_x = \frac{\left(\dfrac{\partial \text{SIC}}{\partial x} \right)^2 \sigma_x^2}{\sigma_{\text{SIC}}^2} \times 100 \ (\%) \tag{9}$$

The estimated uncertainty of Landsat-8 SIC (σ_{SIC}) produced in this study was less than 1% in average for all four cloud contamination categories and the ρ_5 threshold contributes to about 99% of the uncertainty for C2, C3, and C4 and about 97%

400 of the uncertainty for C1 in SIC calculation. Further discussion of the uncertainty of Landsat-8 SIC is handled in Ssection 4.3. As mentioned in Ssection 3.3, Landsat-8 SIC can be largely deviated from actual SIC if Landsat-8 measures partially covered grid cell, in other words, SIC computed from partially-covered grid cells may not be representative of actual ice coverage over the entire grid cell and the corresponding uncertainty of SIC estimates in such grid cell can be as large as the

fraction of the uncovered areas. In order to circumvent such a problem, in this study, $N_{critical}$ was determined as $0.99 \times N_{max}$

405   where N_{max} is the maximum number of Landsat-8 pixels within a 6.25 km × 6.25 km grid cell.
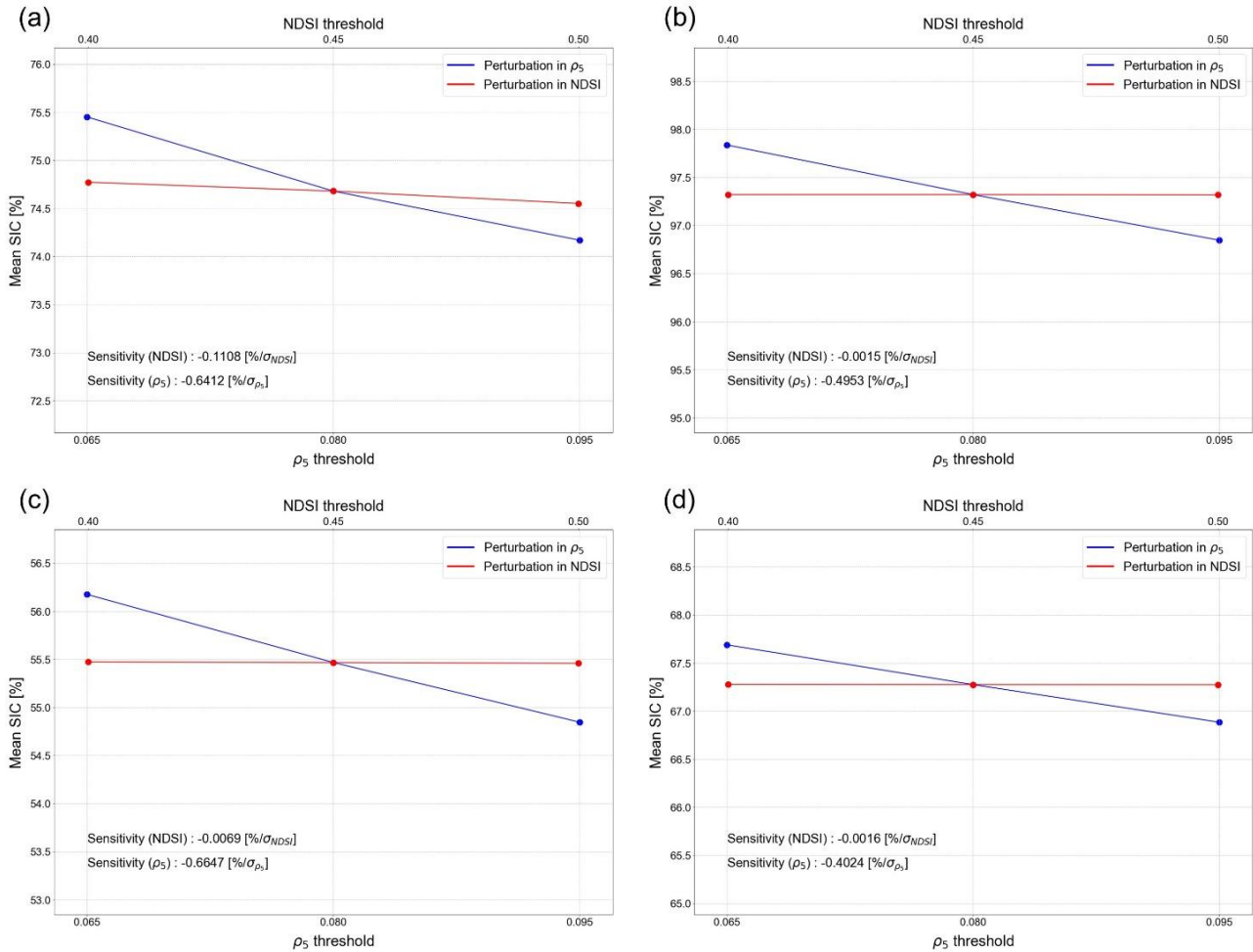
Figure 5: Mean of Landsat-8 SIC values for (a) C1 (i.e., underestimated cloud cover), (b) C2 (i.e., overestimated cloud cover), (c)
410   **C3 (i.e., correctly estimated cloud cover for cloudy sky), and (d) C4 (i.e., correctly estimated cloud cover for clear sky) derived**
from the selected scenes under perturbed thresholds for NDSI (red) and ρ_5 (blue), where ρ_5 and NDSI are the TOA reflectivity at
band 5 of the OLI sensor and the Normalized Difference Snow Index, respectively.

3.5 Application of Land and Region Masks

415   In order to circumvent potential contamination of land signals, in this study, SIC pixels generated over non-ocean regions

were masked using the surface mask described in Ssection 2.2. The sub region mask was applied in addition to the surface

mask to obtain SIC products catalogued into the 12 ~~sub~~-regions. If all SIC pixels in a Landsat-8 scene were masked by the combination of land, ~~sub~~-region, and cloud masks, the scene was removed from the SIC dataset.

420 **4 Result**

4.1 Landsat-8 SIC Dataset

Out of 15,286 Landsat-8 Level 1 images collected over pan-Arctic areas during the study period, the number of Landsat-8 images used for calculating SICs for the categories of C1, C2, C3, and C4 were 6,336 (41.4%), 549 (3.6%), 4,389 (28.1%), and 3,123 (20.4%), respectively. The remaining 989 (6.5%) images were removed from the combination of surface, ~~sub~~-
425 region, and cloud masks. For each of the twelve ~~sub~~-regions, the number of Landsat-8 scenes generated into Landsat-8 SIC (N_{scene}), and the number of produced Landsat-8 SIC pixels (N_{pixel}) for each cloud contamination categories during the study period are shown in Fig. 6 along with the mean and standard deviation of SIC (see Table S10~~9~~ in the supplementary for values). The total number of Landsat-8 SIC pixels produced ~~in~~ during the study period was 2,934,399.
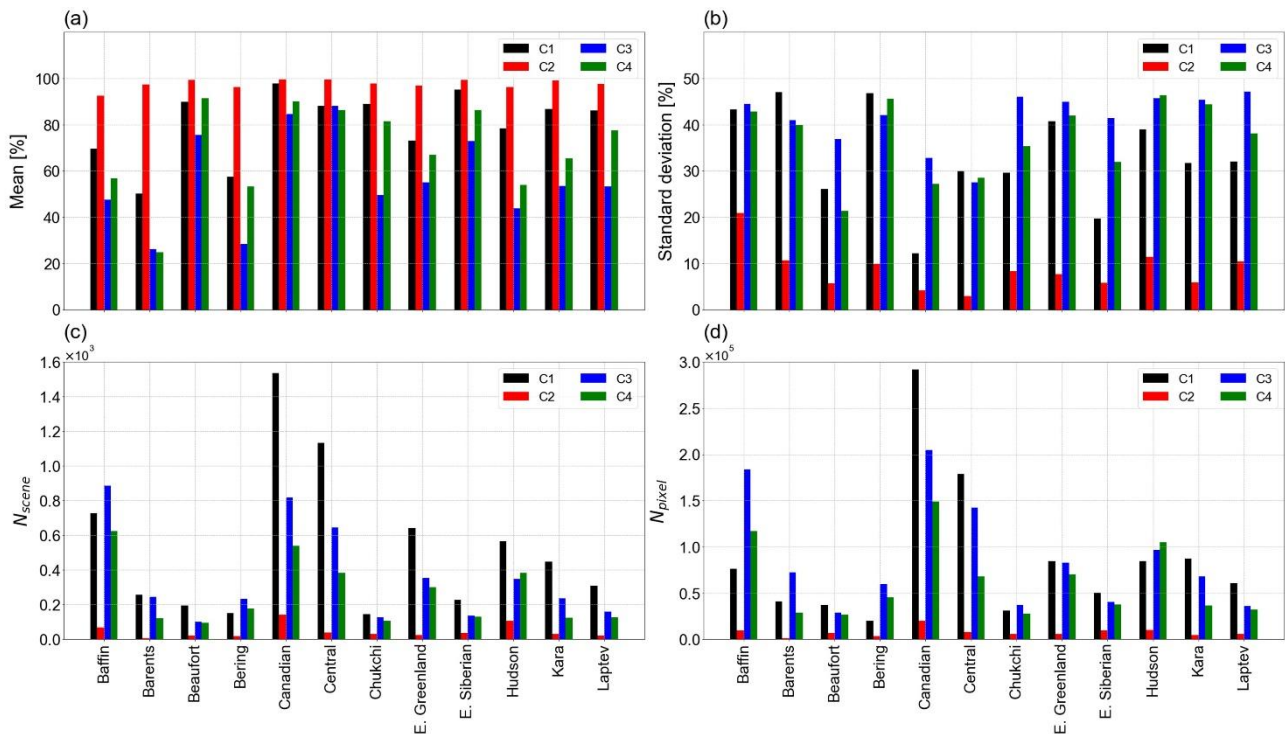
430

Figure 6: (a) The mean SIC, (b) the standard deviation of SIC, (c) the number of Landsat-8 scenes used for SIC production (N_{scene}), and (d) the number of Landsat-8 SIC pixels produced (N_{pixel}) over the twelve ~~sub~~-regions. The black, red, blue, and green bars indicate values for categories C1 (i.e., underestimated cloud cover), C2 (i.e., overestimated cloud cover), C3 (i.e., correctly estimated cloud cover for cloudy sky), and C4 (i.e., correctly estimated cloud cover for clear sky), respectively.

435

4.2 Qualitative Evaluation for Landsat-8 SIC Under Four Cloud Contamination Categories

Figure 7 shows the Landsat-8 true-color image (first column of Fig. 7), classification map of ice, open water, and the removed cloud pixels (second column of Fig. 7), and Landsat-8 SIC in 6.25 km resolution (third column of Fig. 7) for the four selected cases. Ice and open water pixels, which were differentiated following the methods explained in ~~S~~section 3.2,
440 are shown as the white and blue pixels, respectively. Cloud pixels removed in both CFMask and the NDSI criterion are shown as the cyan pixels. Cloud pixels removed from CFMask but undetected from the NDSI criterion are shown as the purple pixels. Cloud pixels removed from the NDSI criterion but undetected in CFMask are shown as the red pixels. SICs were only estimated over grid cells that satisfy $N > N_{critical}$, therefore grid cells with more than 1% of its area covered with cloud pixels or grid cells located near the edges of a Landsat-8 scene have no SIC values. In addition, areas close to the
445 coastline (within 6.25 km) are masked in the Landsat-8 SIC maps presented in Fig. 7.

The first case is an example of the underestimated cloud cover (i.e., C1) on March 13, 2022 over the Kara Sea (first row of Fig. 7) where cloud pixels observed in the lower left area of Fig. 7a w~~ere~~as not removed by CFMask (cyan and purple pixels in Fig. 7b). However, for this particular scene, most of such undetected cloud pixels were removed from application of the NDSI criterion (red pixels in Fig. 7b) and therefore the produced SIC was estimated only over clear sky area (Fig. 7c). The
450 second case is an example of the overestimated cloud cover (i.e., C2) on March 17, 2021 over the Barents Sea (second row of Fig. 7) where FP cloud pixels are densely distributed in the upper left area of Fig. 7e. It is shown that SICs were not estimated ~~over the pixels~~for grid cells with such wrongly-masked pixel~~s~~ (Fig. 7f). The third is an example of correctly estimated cloud cover for cloudy sky (i.e., C3) on June 26, 2022 over the Kara Sea (third row of Fig. 7) where the position of cloud pixels removed from CFMask (cyan and purple pixels in Fig. 7h) coincide well with the location of cloud presented in
455 the true-color image (Fig. 7g). The fourth case is an example of correctly estimated cloud cover for clear sky (i.e., C4) on June 15, 2022 over the Beaufort Sea (fourth row of Fig. 7) where no clouds are observed in both the true-color image (Fig. 7j) and the classification map (Fig. 7k).

For all four cases, over clear sky pixels, discrimination between open water pixels (blue pixels in Fig. 7b, Fig. 7e, Fig. 7h, and Fig. 7k) and ice pixels (white pixels in Fig. 7b, Fig. 7e, Fig. 7h, and Fig. 7k) based on the ρ_5 thresholds coincided well
460 with the locations of open water and ice observed from the true-color images (first column in Fig. 7). Therefore, it can be concluded that the ice-water classification in this study is successfully done and the calculated SICs ~~are well corresponding~~correspond well to the classification results (third column in Fig. 7). In addition, cloud pixels only detected from the NDSI criterion (red pixels in second column in Fig. 7) are rarely observable for the cases of C2, C3, and C4 which further demonstrates the validity of the assumption that all cloud pixels had been removed prior to ice/water classification in
465 ~~S~~section 3.2 for the Landsat-8 scenes under the three categories.
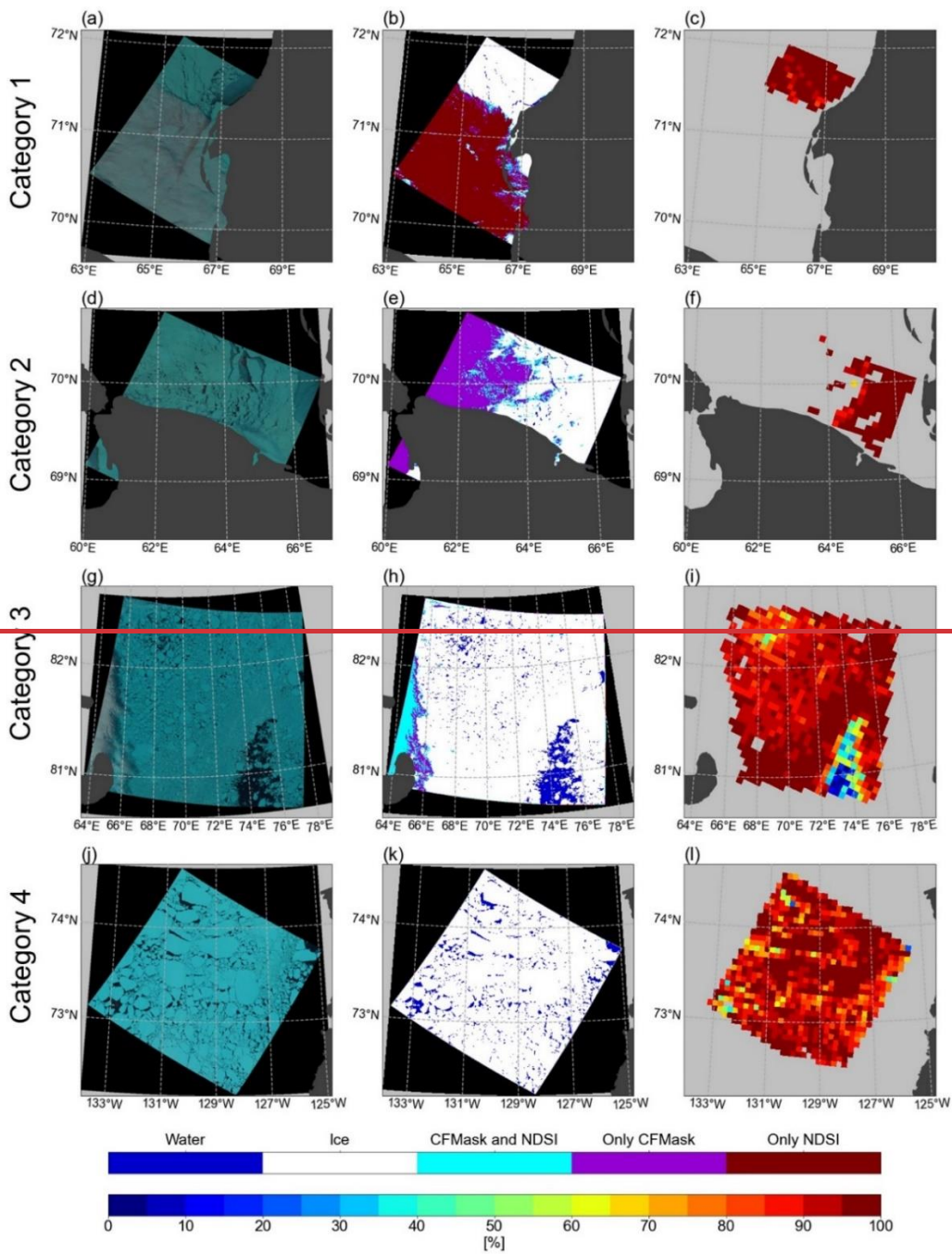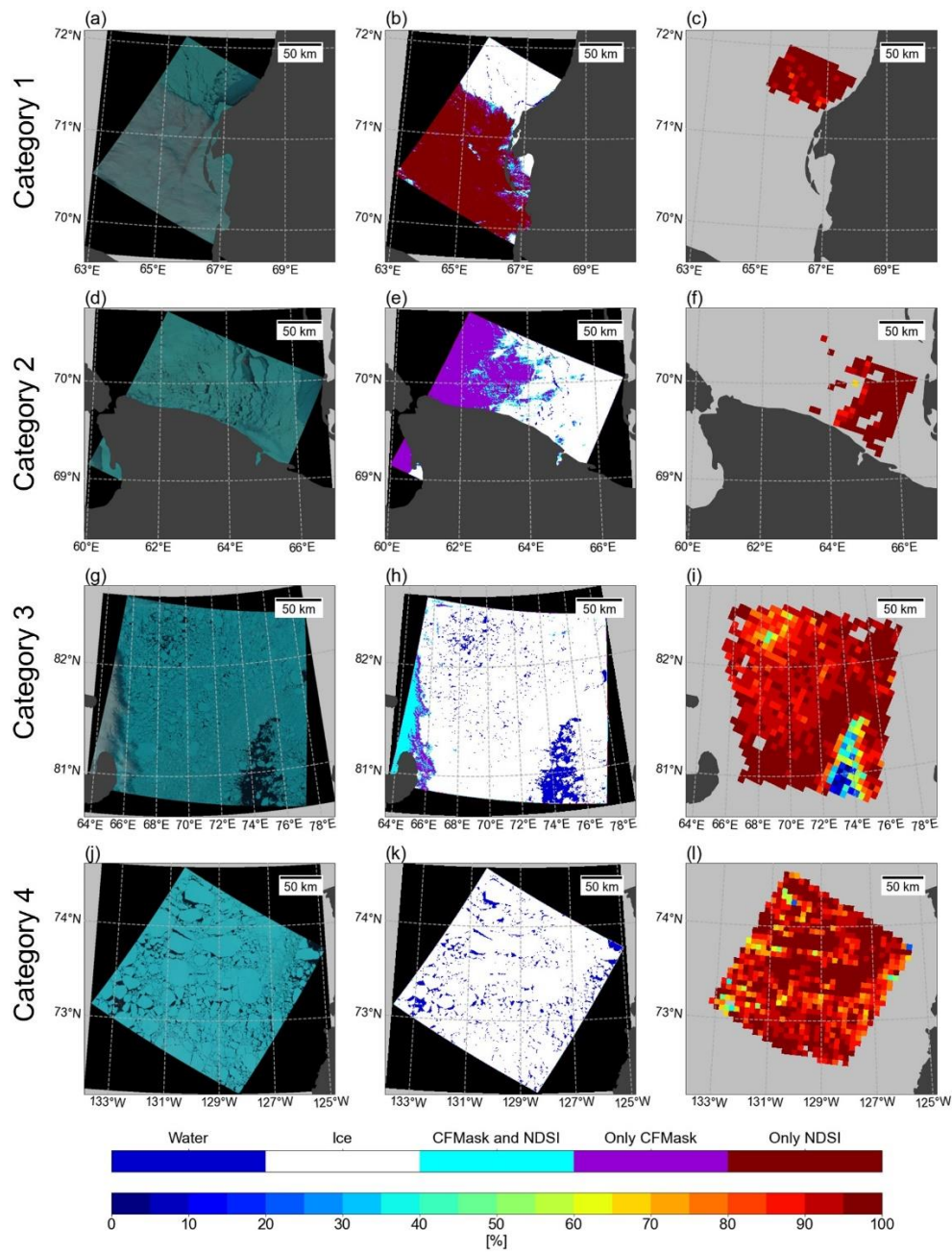
Figure 7: Example of (a, d, g, i) original Landsat-8 true-color image, (b, e, h, k) classification map of ice (white), open water (blue), and cloud (cyan, purple, and red), and (c, f, i, l) Landsat-8 SICs with 6.25 km resolution on (first row) Mar. 22, 2022 over the Kara Sea, (second row) Mar. 17, 2021 over the Barents Sea, (third row) Jun. 26, 2022 over the Kara Sea, and (fourth row) Jun. 15, 2022 over the Beaufort Sea. From top to bottom row, the select cases correspond to the cloud contamination categories of 1, 2, 3, and 4 respectively. SICs are not estimated over areas of cloud mask (cyan, purple and red pixels in the middle column), and SICs near the coastal area (6.25 km) are masked in this figure. The true-color images were obtained from Earth Resources Observation and Science (EROS) Center (2020). ~~downloaded from United States Geological Survey Earth Explorer (https://earthexplorer.usgs.gov/, last access: May 22, 2024)~~.

4.3 Uncertainty of Landsat-8 SIC

The estimated σ_{SIC} from all the selected 480 scenes in ~~S~~section 3.4 was less than 1%, and the ρ_5 threshold was found to be responsible for more than 99% of σ_{SIC}. The uncertainty (i.e., σ_{SIC}) estimated separately for different ~~sub~~-regions or different cloud contamination categories all remained within 1% and had similar contribution ratios with the ρ_5 threshold being the dominant contribution factor to σ_{SIC} (see Table D~~C~~1, D~~C~~2, D~~C~~3 in Appendix D~~C~~ for the exact values). Thus, σ_{SIC} seems to be independent of ~~sub~~-region or cloud contamination label. However, σ_{SIC} was found to be dependent on the SIC value itself. Figure 8 shows the variation in σ_{SIC} with respect to the SIC ~~sub~~-range, illustrating that the lowest uncertainty is ~0.2% in the SICs from 0 to 10% and from 90 to 100% while the highest uncertainty of 4.5% is observed in SIC ranged from 50 to 60% (see Table D~~C~~4 for exact values). ~~The contribution of the two threshold variables to σ_{SIC} was found that ρ_5 threshold explains most of~~Still, the ρ_5 threshold explains most of the uncertainty, regardless of SIC values. In spite of the relatively high uncertainty in Landsat-8 SIC ~~ranged from~~between 20% ~~to~~and 80%, the product can still be used for validation purposes because most PMW SIC products exhibit much larger uncertainties over such SIC range of up to ±12% in the winter (Ivanova et al., 2014) and ±20% in the summer (Meier and Notz, 2010).
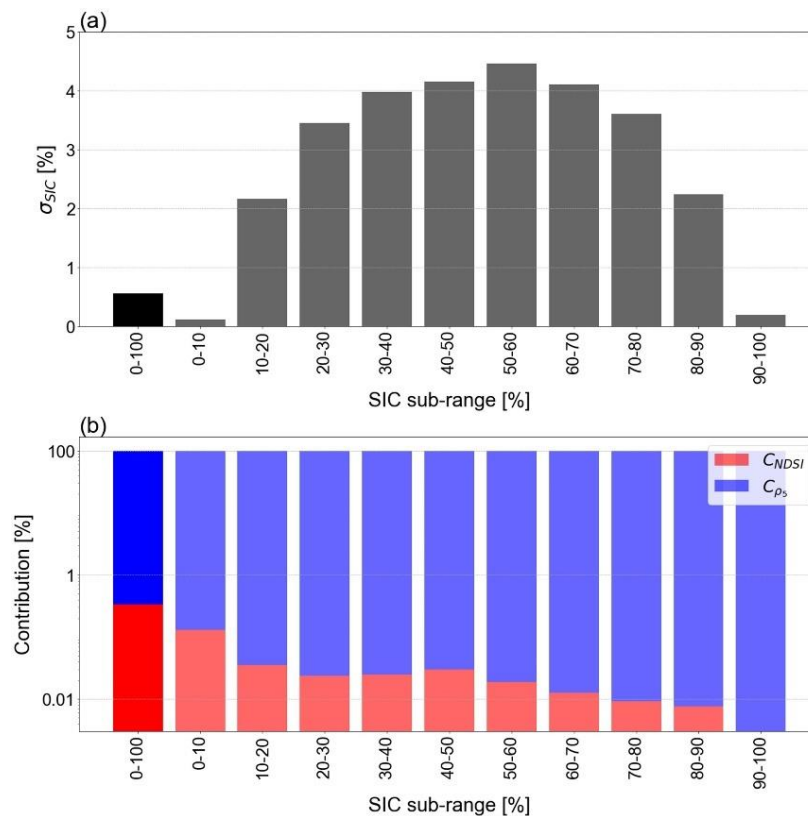
Figure 8: (a) Uncertainties in Landsat-8 SICs (σ_{SIC}) and (b) contributions of the ρ_5 (blue) and the NDSI thresholds (red) to the estimated uncertainties for different SIC ~~sub~~-range, where ρ_5 and NDSI are the TOA reflectivity at band 5 of the OLI sensor and

. Dark and light-coloured bars indicate the uncertainty and contributions computed from all 480 scenes and separately for each SIC sub-range, respectively.

5 Discussion

5.1 Possible Errors in SIC Produced from Landsat-8 Images Labelled C1

As mentioned in ~~S~~sections 3.1 and 3.2, the "clear pixel assumption", which assumes that all cloud pixels in a Landsat-8 image ~~has~~have been removed by the application of CFMask, is not valid for Landsat-8 images labelled C1 in ~~S~~section 3.1. For Landsat-8 SIC associated with C1 category, therefore, it is necessary to evaluate the possible uncertainty in SIC induced by unremoved cloud pixels (i.e., underestimated cloud cover). Evaluation was performed as follows: From Landsat-8 images under the C1 category, ~~sub section with 100% cloud cover based on visual inspection, but less than 100% cloud cover from CFMask was selected. From the collected sub-sections,~~ those having 100% cloud cover based on visual inspection, but less than 100% cloud cover from CFMask were selected. From these images, the ρ_5 and NDSI values were collected over pixels that were not masked by CFMask (i.e., undetected cloud pixels). Classification following the process illustrated in Fig. 4 was performed over the collected undetected cloud pixels to quantitatively assess the possible errors in SIC estimated over such pixels. A total of 6,721,605 undetected cloud pixels were used in this evaluation, and the name and location of Landsat-8 images used are shown in Fig S3~~2~~ and Table S11~~0~~ in the supplements.

The classification result is summarized in Table 4 and Fig. C~~B~~2. From the distribution of the unmasked cloud pixels in the two-dimensional histogram between NDSI (*x*-axis) and ρ_5 (*y*-axis) in Fig. C~~B~~2, it can be seen that the NDSI criterion used in this study reinforces the cloud removal process by filtering cloud pixels that were undetected by CFMask. However, even with the additional procedure to remove remained cloud signals (i.e., the NDSI criterion), 8.54% of the undetected cloud pixels are still classified as open water and/or ice. It is noted that such cloud pixels (i.e., cloud pixels undetected from both CFMask and the NDSI criterion) were predominantly classified as ice (Table 4). Therefore, it can be inferred that the undetected cloud pixels in a Landsat-8 image can induce positively biased SIC and thus for SICs produced from Landsat-8 images labelled C1 over which the "clear pixel assumption" is invalid, the error from ice/water classification is estimated to be large as 8.54% from the percentage of cloud pixels classified as ice in Table 4. The possibility of such large uncertainties should be taken into note when using Landsat-8 SIC labelled C1.

Reference \ Classified (ρ_5 and NDSI)	Open water	Ice	Cloud
Undetected Cloud (by CFMask)	215 (0.00%)	573,922 (8.54%)	6,147,468 (91.46%)

Table 4: The number of cloud pixels that were undetected from the C Function of Mask (CFMask) classified into open water, ice, and cloud from application of the procedure in Fig. 4. The scenes used for the evaluation belong to C1 (i.e. underestimated cloud

cover) category from the method described in Ssection 3.2. The values inside the parentheses indicates the percentage of pixels that belong to each category.

5.2 Evaluation of Landsat-8 SIC Using Ice Charts

The accuracy of Landsat-8 SIC produced in this study was evaluated using ice charts provided by MET Norway as reference. For quantitative comparison, ice charts were collocated into the grid system of Landsat-8 SIC (i.e., PSR grid with 6.25 km resolution) as follows: Data points on the ice chart within each 6.25 km × 6.25 km grid cell were collected, and the SIC mean value from the collected data points were taken as the representative SIC value of ice chart for the 6.25 km × 6.25 km grid cell. It is important to be noted that SIC values in the original ice charts are not normally-defined SICs in satellite remote sensing, but contain uncertainties represented by the ice concentration range defined in Table A1. Therefore, it is necessary to consider the propagation of uncertainty in the collocation process. Uncertainty of the collocated ice chart SIC was estimated by taking the average of the uncertainty in ice chart data points collected from each 6.25 km × 6.25 km grid cell. To avoid the influence of land contamination, a 6.25 km coastal area mask was applied to both SICs prior to the comparison. The number of collocated data points used in the evaluation was 45,547.

From Fig. 9, a good linear relationship (i.e., correlation coefficient of 0.96) between Landsat-8 SIC and ice chart SIC is observed. The spreads (i.e., 20 and 80 percentiles) of Landsat-8 SIC for ice chart SIC sub-ranges, which are shown as red vertical lines in Fig. 9a, was larger in SIC ranged from 20% to 80% relative to other ranges, which is likely due to a consequence of the wider concentration intervals assigned to the 20-80% of SIC values in the original ice chart (Table A1). In addition, SIC from the ice charts was found to be positively biased totends to be higher than that found from Landsat-8 SIC and the bias is more pronounced in the lower SIC range.; This type of state dependent overestimation of SIC from ice charts has been reported in which is also supported by previous works of Tonboe et al. (2016) and Cheng et al. (2020), which shows that overestimation of SIC from ice charts is largest in the lower SIC range due to the "better-safe-than-sorry" practices of the ice charting community. For quantitative comparison of the bin-wise mean biases in Landsat-8 SIC relative to ice chart SIC, bin-averaged SICs from Landsat-8 (red triangle in Fig. 9b) and from ice charts (blue circles in Fig. 9b) were plotted along with their respective uncertainties. Uncertainties of Landsat-8 SICs over the SIC sub-ranges were taken as the values from Table DC4. Except for 70-80% SIC interval, Landsat-8 SICs were negatively biased to ice chart SICs. However, the mean biases for all SIC sub-range were found to be within the uncertainty ranges estimated for each product.
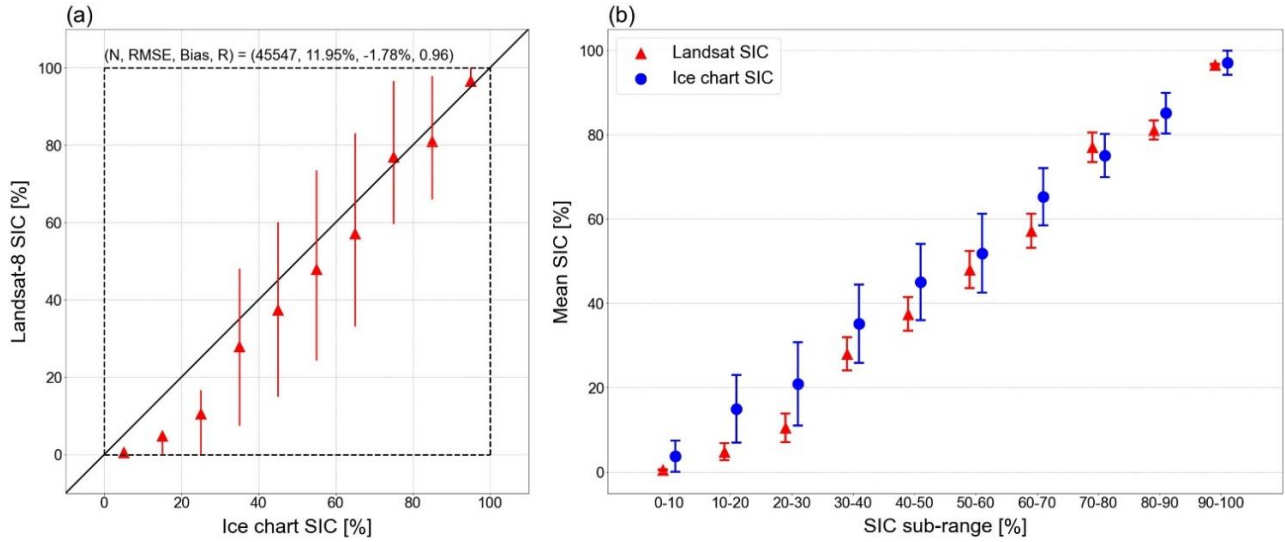
550

Figure 9: (a) Scatter plot of bin-wise mean Landsat-8 SICs and ice chart SIC sub-ranges. The bin-wise mean SICs are shown as red triangles, and the 20 and 80 percentiles are shown as the red vertical lines. The values for number of data points (N), root-mean-square error (RMSE), bias, and Pearson correlation coefficient (R) are presented. (b) For the same SIC intervals as (a), the bin-wise mean SICs of Landsat-8 (red triangle) and ice chart (blue circle) and their respective uncertainties (vertical lines). The uncertainties of Landsat-8 SIC are taken from the values in Table D C 4.

555

5.3 Evaluation of Landsat-8 SIC Over Melt Ponds

The evaluation of variation in Landsat-8 SICs due to melt pond presence was performed using the MPF dataset (Niehaus and Spreen, 2022) described in Ssection 2.5 as reference data for melt ponds. As mentioned in Section 2.5, a total of six Landsat-

560   8 scenes obtained from the periods of Jul. 2020, Aug. 2020, and Jul. 2021 were used in the evaluation. The evaluation was conducted as follows: First, the collocation of the MPF dataset into the grid system of Landsat-8 SIC was performed. This was done by collecting MPF data points within each 6.25 km × 6.25 km grid cell, and taking the mean value of the collected MPF data points as the MPF values for each corresponding grid cell in 6.25 km resolution. In addition, from the OW masks in the MPF dataset, SIC values (SIC_{MPF}) were computed in the grid system of Landsat-8 SIC following the same method

565   introduced in Ssection 3.3. Second, in order to remove the effects of SIC variation from the evaluation, the corresponding Landsat-8 SIC and MPF data points were collected when data points satisfy $SIC_{MPF}=100\%$. The number of collected data points is 98. From the collected data points, the net ice surface fraction (C_{net}) was computed as the following,

$$C_{net} = (1 - MPF) \times SIC_{MPF} \tag{10}$$

where MPF is the melt pond fraction and SIC_{MPF} is the estimated SIC value from the MPF dataset. Since SIC_{MPF} was fixed to

570   100%, in this study, the variation in C_{net} can be considered solely driven by the variation in MPF.

The robustness of the Landsat-8 SIC to the presence of melt ponds is illustrated in Fig. 10, which is a scatter plot between the collected C_{net} (x-axis) and Landsat-8 SIC (y-axis). In this plot, the MPF was varying from 0% to 33%, and therefore, the

computed values of C_net are ranged from 67% to 100%. However, SICs estimated from Landsat-8 are observed to be nearly independent to the varying C_net (statistically insignificant correlation coefficient of 0.11) and thus nearly independent of MPF.

575 Although a few Landsat-8 SICs are observed to be affected by melt pond presence (data points highlighted in red from Fig. 10), which can be expected because melt ponds are not easily ~~discernible to~~distinguished from open water, the number of such data points are very small (only four data points out of 98 data points). It is noted that on average the deviation from 100% ice concentration computed from the data points shown in Fig. 10 was less than 1%. Therefore, it can be inferred that the impact of melt pond presence in SIC calculation using Landsat-8 imagery is small, and that the proposed algorithm for

580 SIC production in this study ~~has robustness~~is robust regardless of surface melting.
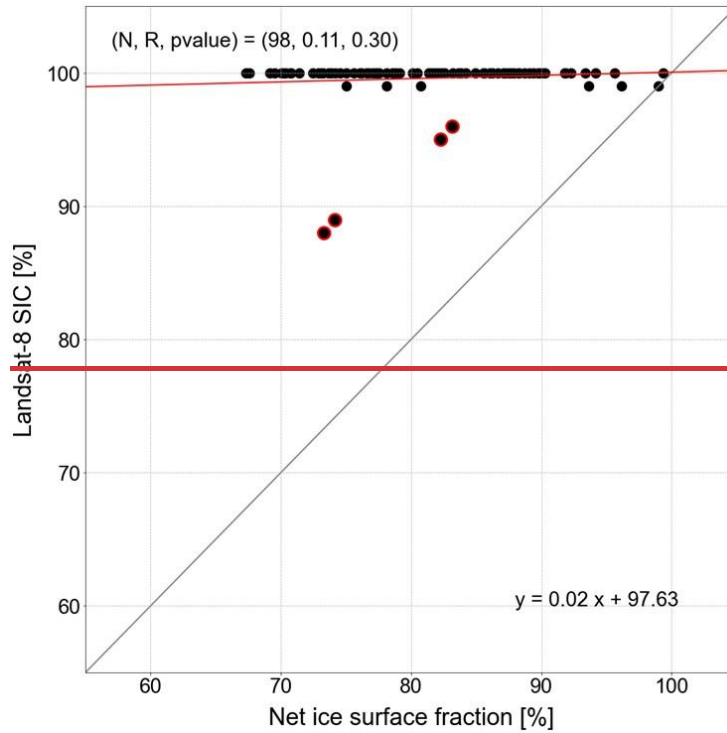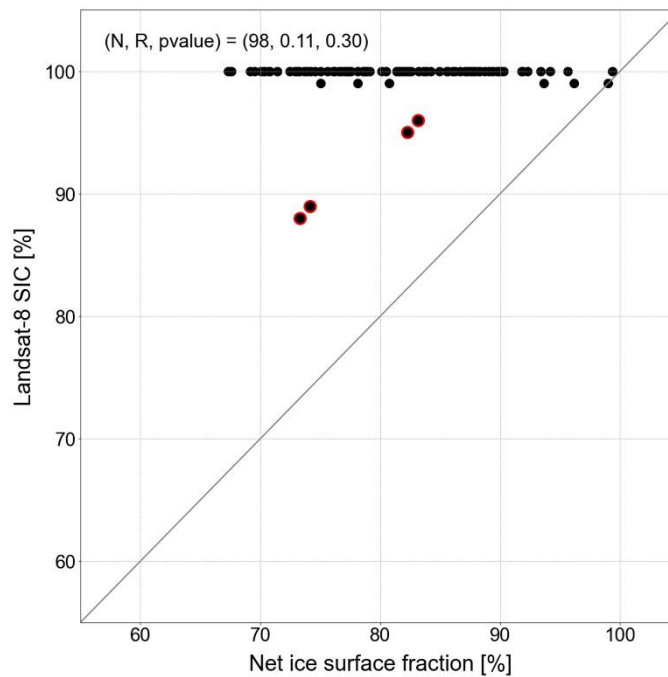
Figure 10: Scatter plot of net ice surface fraction (x-axis) and Landsat-8 SIC (y-axis). The data points shown satisfy SIC$_{MPF}$=100%, and have MPF that vary from 0% to 33%. Data points with more than 4% deviation of Landsat-8 SIC from 100% ice concentration are highlighted in red. **The values for number of data points (N), Pearson correlation coefficient (R), and p-value for the correlation coefficient are presented.** ~~**The red line indicates the least-squares regression line.**~~

5.4 Possible Applications of Landsat-8 SIC for Assessing PMW-based SICs

Landsat-8 SIC produced from this study can be utilized to assess the PMW-based SICs. This section provides the possible application of the constructed Landsat-8 SIC for examining PMW-based SICs. To do this, Landsat-8 SIC was downscaled to 25 km resolution and compared against SICs estimated from BT and NT algorithms, both provided in the PSR grid with 25 km resolution and obtained from NSIDC (Meier et al., 2021), for the selected two cases of Landsat-8 scenes acquired during melting (Jul. 21, 2022 over the Laptev Sea) and freezing (Mar. 4, 2022 over the Chukchi Sea) seasons, respectively. To avoid the influence of land contamination, a coastal area mask, which was also downscaled to 25 km resolution, was applied before the comparison.

Figure 11 illustrates spatial distributions of the three different SICs, differences in SICs of BT and NT from Landsat-8, and scatter plots of BT and NT SIC against Landsat-8. For the case of the melting season (top two rows in Fig. 11), BT SIC showed a positive bias of 8.95%, RMSE of 16.30%, and correlation coefficient of 0.92 (Fig. 11d) to Landsat-8 SIC while SIC retrieved from the NT algorithm is negatively biased to Landsat-8 SIC by -5.21% with a RMSE of 14.35%, and correlation coefficient of 0.94 (Fig. 11h). It is interesting to note that BT SICs are positively (negatively) biased to Landsat-8 SIC for lower (higher) concentrated ice areas (Fig. 11c), while opposite patterns are observed for NT SICs (Fig 11g). Both

PMW-based SICs show the largest disagreement with Landsat-8 SIC near the edges of pack ice (i.e., boundaries between sea ice and open water).

605 For the scene in the freezing season (bottom two rows in Fig. 11), the BT and NT algorithms produced nearly 100% SICs for all grids in this case while Landsat-8 SIC shows lower SIC values in regions coinciding with the leads in the pack ice observed from the true-color image. As a result, positive biases were observed near the position of the lead (Fig. 11k and Fig. 11o), and mean biases for the BT and NT algorithms were 0.83% and 0.53%, respectively. RMSEs of BT and NT SIC were calculated as 1.35% and 0.81%, respectively, which are lower than the RMSE evaluated during the melting season for the

610 two SIC algorithms (Fig. 11i and Fig. 11p).
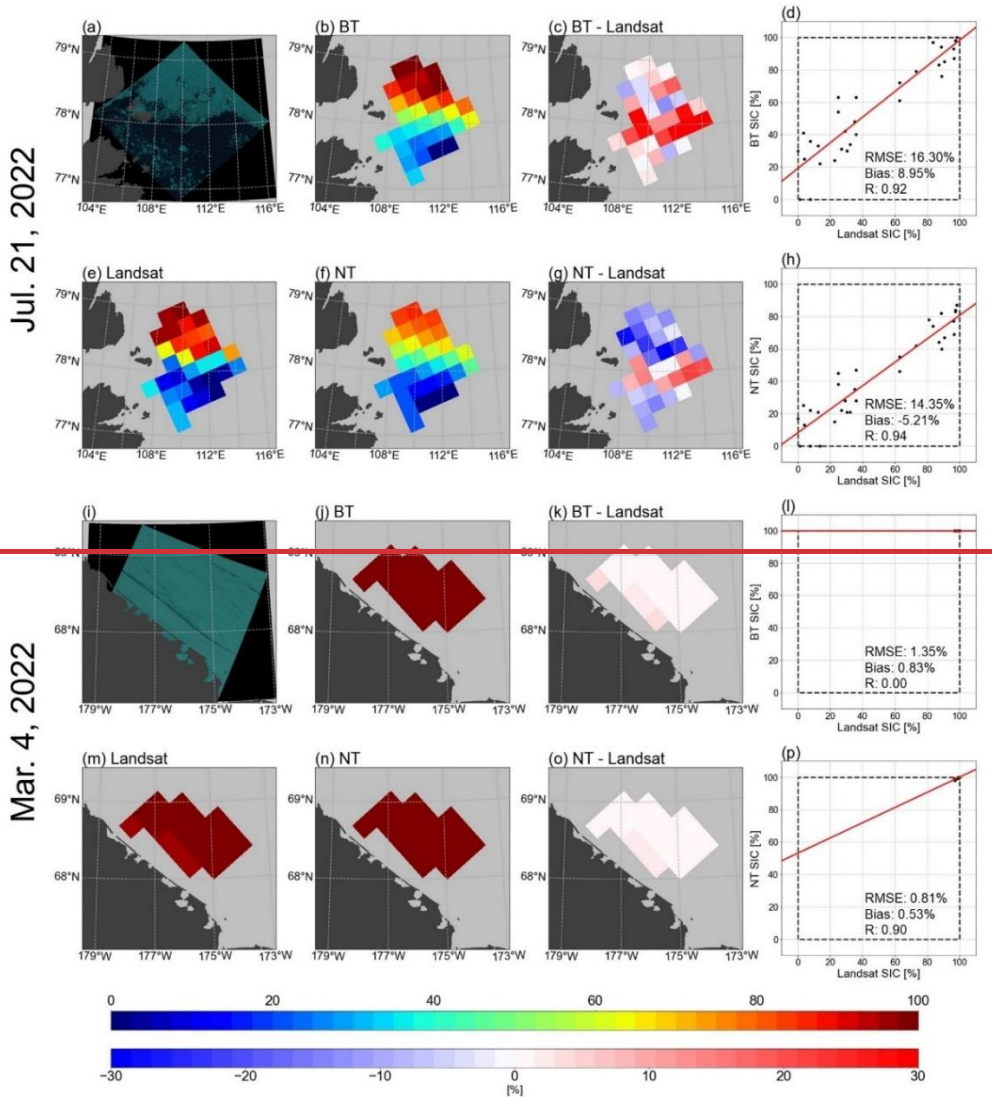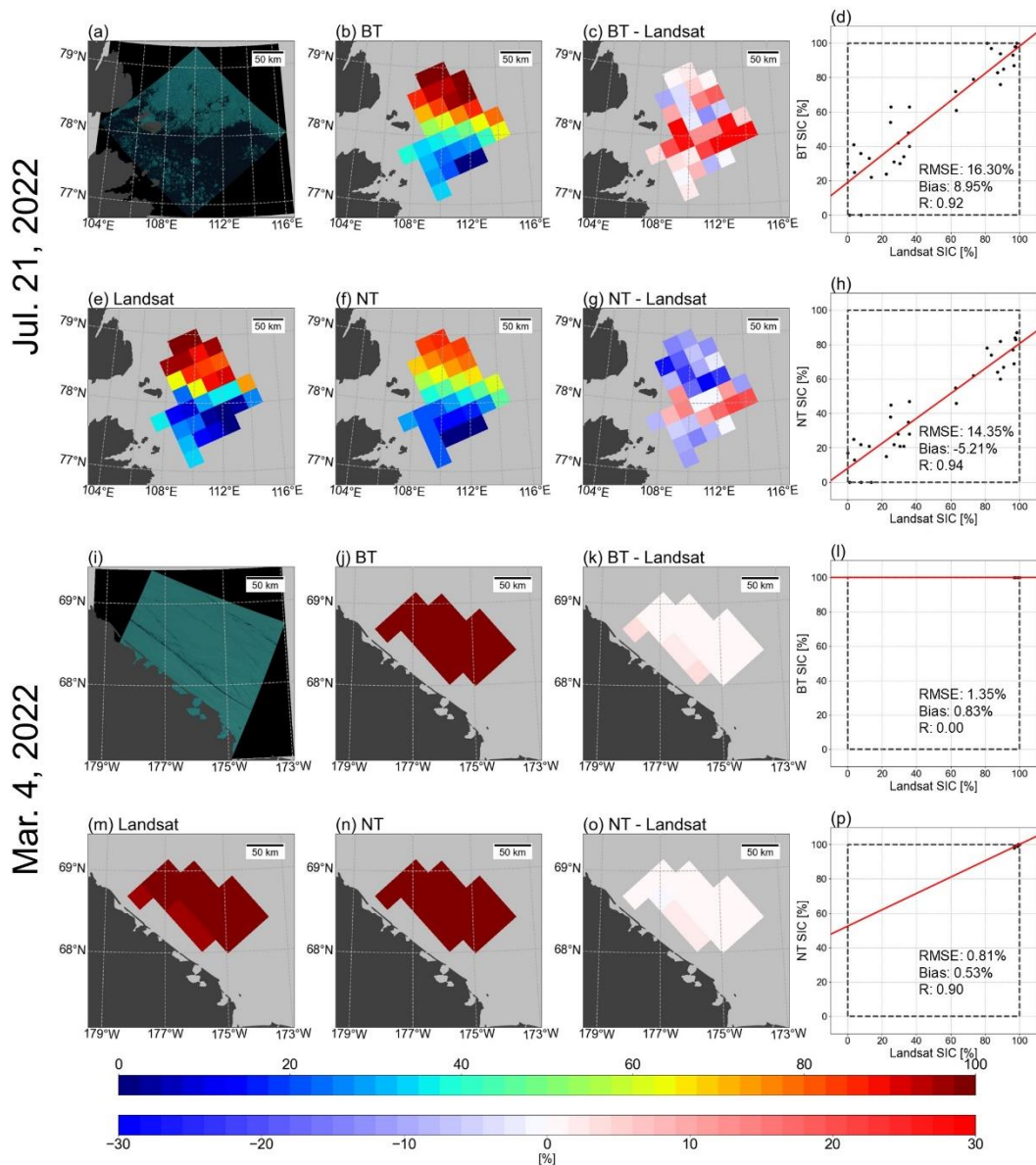
Figure 11: Geographical distributions of (a, i) original Landsat-8 true-color image, (e, m) Landsat-8 SIC, (b, j) SIC from the Bootstrap (BT) algorithm, (f, n) SIC from the NASA Team (NT) algorithm, (c, k) difference in SICs between BT and Landsat-8, (g, o) difference in SICs between NT and Landsat-8 and scatterplot (d, l) between Landsat-8 SIC and SIC from BT and (h, p) between Landsat-8 SIC and SIC from NT. The values of root-mean-square error (RMSE), bias, and Pearson correlation coefficient (R) are presented with the scatter plots. Upper two panels for July 21, 2022 (melting season) over the Laptev Sea and for March 4, 2020 over the Chukchi Sea, respectively. The true-color images were obtained from Earth Resources Observation and Science (EROS) Center (2020) and the SIC retrievals from the BT and NT algorithms were obtained from Meier et al. (2021).~~downloaded from United States Geological Survey Earth Explorer (https://earthexplorer.usgs.gov/, last access: May 22, 2024).~~

6 Code and Data Availability

The Landsat-8 SIC dataset can be downloaded at https://zenodo.org/doi/10.5281/zenodo.10973297 (Jung et al., 2024).
Datasets generated for each Arctic ~~sub-~~region can be found in "sic_landsat08_{~~sub-~~region name}.nc. The datasets are stored

625 in netCDF format and can be accessed using software including Python, MATLAB, and QGIS. Along with the SIC values, N, coastal mask, and ~~sub-~~region mask are also provided in a 1792 × 1216 array format. Cloud contamination category and name of the original Landsat-8 files are also provided for each scene. Variables in the netCDF file are visualized in Fig. 12. Fill values were assigned to grids outside the coverage of a Landsat-8 scene, grids over land, or grids masked by clouds (black grids in Fig. 12a, b). Description of each variable and the fill/flag values are summarized in Table 5.

630 Datasets used to produce and validate the Landsat-8 SIC are listed as follows.

- 'Landsat-8 Collection 2 Level 1 Product' and the corresponding true-color images are accessible from United States Geological Survey Earth Explorer at (https://earthexplorer.usgs.gov/). (Earth Resources Observation and Science (EROS) Center, 2020).

- 'Arctic and Antarctic Regional Masks for Sea Ice and Related Data Products, Version 1' used to mask non-ocean areas

635 and distinguish ~~sub-~~regions can be accessed at https://doi.org/10.5067/CYW3O8ZUNIWC. (Meier and Stewart, 2024).

- 'Landsat surface type over water from supervised classification of surface broadband albedo estimates (Version_2021_fv0.01)' used to test the performance of the ice and open water classification can be accessed at http://doi.org/10.25592/uhhfdm.9181. (Kern, 2021).

- 'Arctic Ocean – Sea Ice Concentration Charts – Svalbard and Greenland' ice charts used to evaluate the produced

640 Landsat-8 SIC can be accessed at https://doi.org/10.48670/moi-00128 .(E.U. Copernicus Marine Service Information (CMEMS), accessed on 11 June 2024).

- 'Melt pond fraction on Arctic sea-ice from Sentinel-2 satellite optical imagery (2017-2021)' used to test the robustness of Landsat-8 SIC over melt ponds can be accessed at https://doi.org/10.1594/PANGAEA.950885. (Niehaus and Spreen, 2022).

645 - 'NOAA/NSIDC Climate Data Record of Passive Microwave Sea Ice Concentration, Version 4' used to illustrate possible applications of Landsat-8 SIC dataset can be accessed at https://doi.org/10.7265/efmz-2t65 (Meier et al., 2024).

The python codes for Landsat-8 SIC production, sensitivity and uncertainty analysis, ice/water classification evaluation, Landsat-8 SIC validation, and figure generation are accessible at https://doi.org/10.5281/zenodo.12754603 (Jung, 2024). Example data to check the functionalities of each python code are provided with the code repository.

650
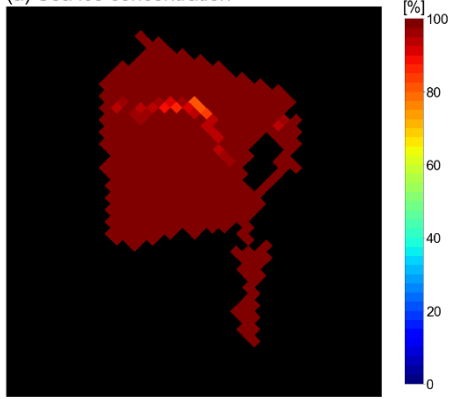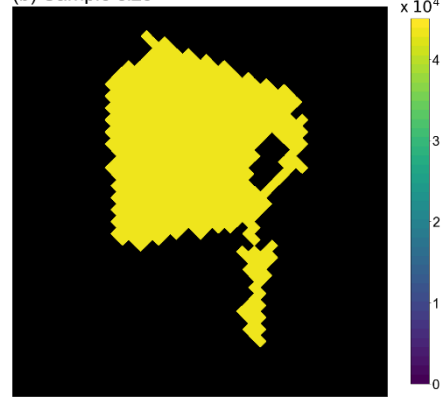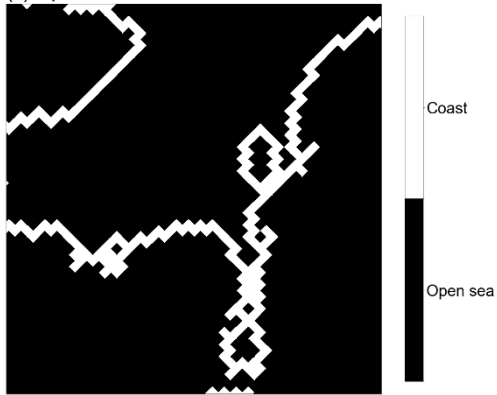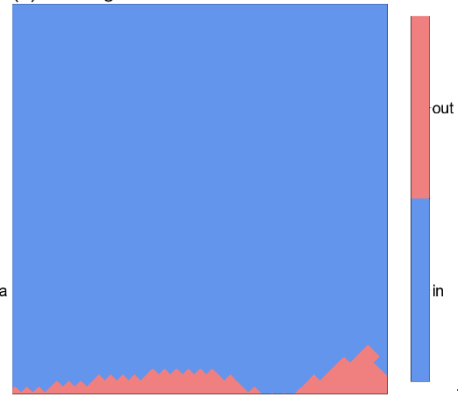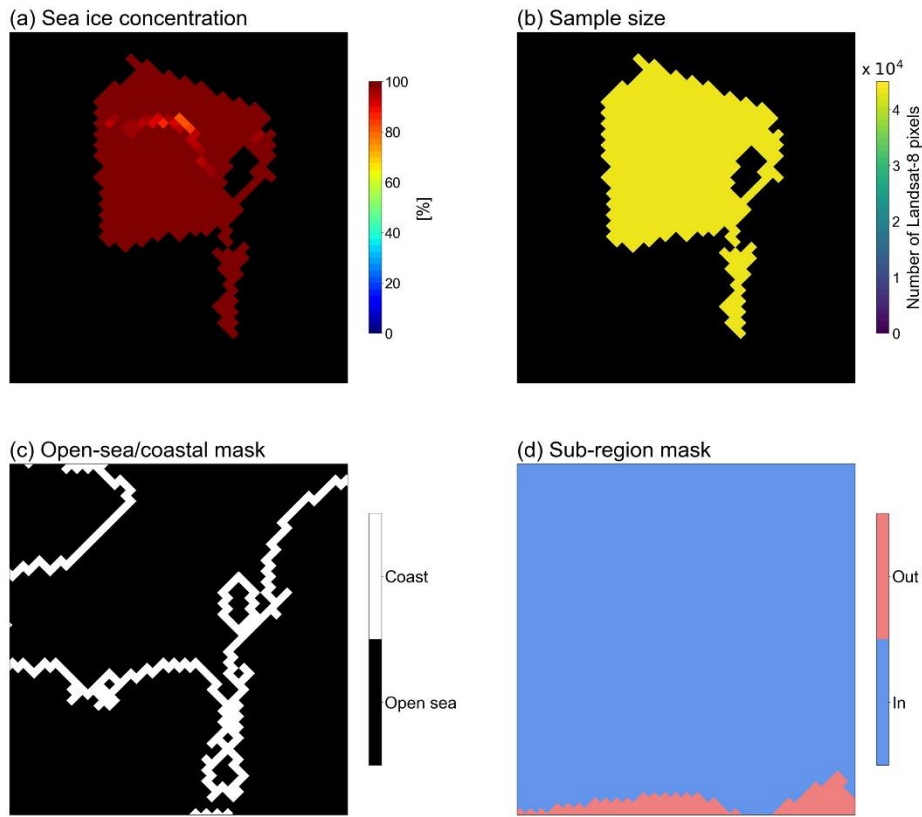
Figure 12: Variables in the Landsat-8 SIC netCDF. The scene is from Jun. 12, 2021 over the Canadian Archipelago. For the (d) sub-region mask, 'In' and 'Out' denote grid cells located inside and outside the designated region, respectively.

655

Variable	Long Name	Flag values
sea_ice_concentration	Estimated fractional sea ice area from Landsat-8 measurements	[-99: Fill value]
sample_size	Number of Landsat-8 pixels used to estimate the sea ice concentration	[0: Fill value]
coastal_mask	Open sea/Coastal Flag	[0: Open_sea, 1: Coast]
sub_region_mask	Sub-region Flag	[0: inside_sub_region, 1: outside_sub_region]

Table 5: Variables in the Landsat-8 SIC netCDF file, name of the variables, and the flag values for each variable.

7 Conclusion

660 In this study, three years (2020-2022) of Landsat-8 data were collected and used to generate sea ice concentration (SIC) datasets in the polar stereographic grid with 6.25 km resolution. A total of 14,297 Landsat-8 images were used to calculate 2,934,399 SIC grid points. Each Landsat-8 SIC is catalogued under a netCDF file named after the twelve ~~sub~~ regions.

Each Landsat-8 image was labelled into four cloud contamination categories (i.e., C1, C2, C3, and C4) according to the overall quality of cloud mask over the image. The categories are provided in the variable under the name 665 'cloud_contamination_category' of the Landsat-8 SIC dataset to allow for selection of SICs calculated without the interference of cloud signals.

The uncertainty of Landsat-8 SIC was estimated to be ranged from 1 to 4% based on the Gaussian error propagation method. In addition, to regulate the potential uncertainty that may arise from the use of partially-covered grid cells, SIC was only produced for grid cells with over 99% of its area covered by Landsat-8 pixels. Evaluation of Landsat-8 SIC using SIC from 670 ice charts show good linear correlation between the two products and also reveal existence of negative bias in Landsat-8 SIC. However, the bias was found to be within the uncertainty range of the Landsat-8 and ice chart SIC. In addition, the production method used for Landsat-8 SIC was found to be robust over melt ponds. Thus, Landsat-8 SIC produced in this study can be considered to be reliable estimates of SIC.

Comparison of Landsat-8 SIC against SIC retrievals from NASA Team (NT) and Bootstrap (BT) algorithms for two cases 675 reveal overall negative bias in NT and positive bias in BT SIC. The spatial distribution of the bias shows that bias in NT and BT SIC may be related ~~with~~to the SIC values, with NT SIC exhibiting stronger negative bias in high SIC regime, and BT SIC showing stronger positive bias in low SIC regime. This suggests that the Landsat-8 SIC can be used as reference SIC to generate quantitative error statistics of various passive microwave SIC retrievals over different regions, seasons, and SIC values, which can be used to develop an optimal combination of existing SIC algorithms or be used to provide realistic 680 observation errors to enhance the performance of sea ice data assimilation.

Future works are aimed to extend the temporal and spatial coverage of the current Landsat-8 SIC dataset by the addition of Landsat-8 images from the years 2018 and 2019. In addition, given the large number of Landsat-8 SIC data points generated in this study, the obtained SIC values also have the potential to be used to train deep-learning models in order to retrieve optimal SIC estimates over the Arctic.

685

690

8 Appendices

 Appendix A: SIC Values in The MET Norway Ice Chart

Concentration class	Concentration interval [%]	Fixed concentration value [%]	Concentration range [%]
Fast Ice	100	100	0
Very Close Drift Ice	90-100	95	5
Close Drift Ice	70-80	75	5
Open Drift Ice	40-60	50	10
Very Open Drift Ice	10-30	20	10
Open Water	0-10	5	5

Table A1: Concentration class, concentration interval, fixed concentration value, and concentration range of the operational ice chart produced by MET Norway.

Appendix B: Visual Inspection for Cloud Mask Quality Control

In this section, a step-by-step description of the process taken to perform the visual inspection of Landsat-8 scenes is presented. As defined in Section 3.1, each pixel in a Landsat-8 scene can be sorted into the following four categories depending on the state of cloud mask for the pixel: False negative (FN; cloud pixel mistaken as clear pixel), false positive (FP; clear pixel mistaken as cloud pixel), true negative (TN; clear pixel identified as clear pixel), and true positive (TP; cloud pixel identified as cloud pixel). It is noted that the pixels with FN are used to calculate SICs while the pixels with FP are not, indicating that the presence of FN pixels can directly introduce errors in the calculated SIC value. Therefore, visual inspection was performed very strictly to detect FN pixels.

Figure B1 outlines the steps taken to perform the visual inspection. The descriptions of each step are provided along with an example case of a Landsat-8 scene that is categorized into C1 during the section-wise inspection stage.

715

Step 1. Generating jpeg file of cloud mask (i.e., cloud mask image).

For each Landsat-8 scene, a false-colour image with each pixel classified as ice (white pixels in Fig. B2b, d), open water (blue pixels in Fig. B2b, d), cloud (grey pixels in Fig. B2b, d), and fill value (black pixels in Fig. B2b, d) is constructed using the OpenCV module in Python. Ice and open water pixels are differentiated using the method 720 described in Section 3.2. Cloud pixels are classified by masking the medium confidence cloud, high confidence cirrus, cloud shadow, and dilated cloud pixels identified by the quality assessment band (i.e., the cloud mask array produced by CFMask).

Step 2. Comprehensive inspection of cloud mask quality.

The cloud mask image generated in Step 1 is visually inspected against the true-colour image to identify sections 725 populated with FN, FP, TN, or TP pixels. This is done in the following order: First, if no cloud pixels are observed from both the cloud mask image and the true-colour image (i.e., all pixels in the image are TN pixels), the scene is labelled as C4. Second, if any cluster of FN pixels is observed, the scene is labelled C1. Third, if any cluster of FP pixels is identified, the scene is labelled C2 and passed on to Step 3. If the clusters of cloud pixels in the cloud mask

image are well corresponding to the position of clouds observed in the true-colour image (i.e., TP pixels), the scene is labelled C3 and passed on to Step 4 (Fig B2a, b).

Step 3. Comprehensive inspection of cloud mask quality for C2.

For the scenes passed on to this step (i.e., scenes labelled C2 from Step 2), the cloud mask image is recreated using a higher confidence threshold (i.e., high confidence cloud, high confidence cirrus, cloud shadow, and dilated cloud pixels) for the quality assessment band. The new cloud mask image is visually inspected against the true-colour image, and if any cluster of FN pixels is observed, the confidence threshold for the quality assessment band is returned to its initial value (i.e., medium confidence cloud, high confidence cirrus, cloud shadow, and dilated cloud pixels). If the observed clusters of cloud pixels in the new cloud mask image are well corresponding to the position of clouds observed in the true-colour image, the higher confidence threshold is kept, and the scene is passed on to Step 4.

Step 4. Section-wise inspection of cloud mask quality.

In this step, the identified clusters of TP pixels are inspected in more detail. For each cluster of TP pixels observed, we zoom in (i.e. about 1000×1000 pixels; the full-size image is approximately 8000×8000 pixels) to the section of the cluster to check for the existence of FN pixels. If any FN pixels are found within the cluster, the scene is labelled C1 (Fig B2c, d).

An example of how a Landsat-8 scene may be categorized according to the process described in Fig B1 is presented using the case of a Landsat-8 scene acquired on Mar. 25, 2022, over the Barents Sea (Fig B2). First, from Step 2. (i.e., the comprehensive inspection step), visual inspection of the cloud mask image (Fig. B2b) against the true-colour image (Fig. B2a) shows that the position of clouds in the cloud mask array is generally well corresponding to those observed in the true-colour image. Therefore, at this step, this scene is labelled C3 and passed on to Step 4 as described above. Next, the section-wise inspection of the cloud mask quality is performed by zooming in to the cloud areas. This is illustrated in Fig. B2c and Fig. B2d, which is a zoomed in image of the area enclosed by the red rectangle in Fig. B2a and Fig. B2b. Inspection of this sub-section shows the presence of unmasked cloud shadow pixels, which results in the erroneous classification of ice as open water. Therefore, at this step, the label of this scene is changed to C1.

The visual inspection was done by HJ and it took approximately 5 – 10 minutes to inspect one Landsat-8 scene for cloud cover.
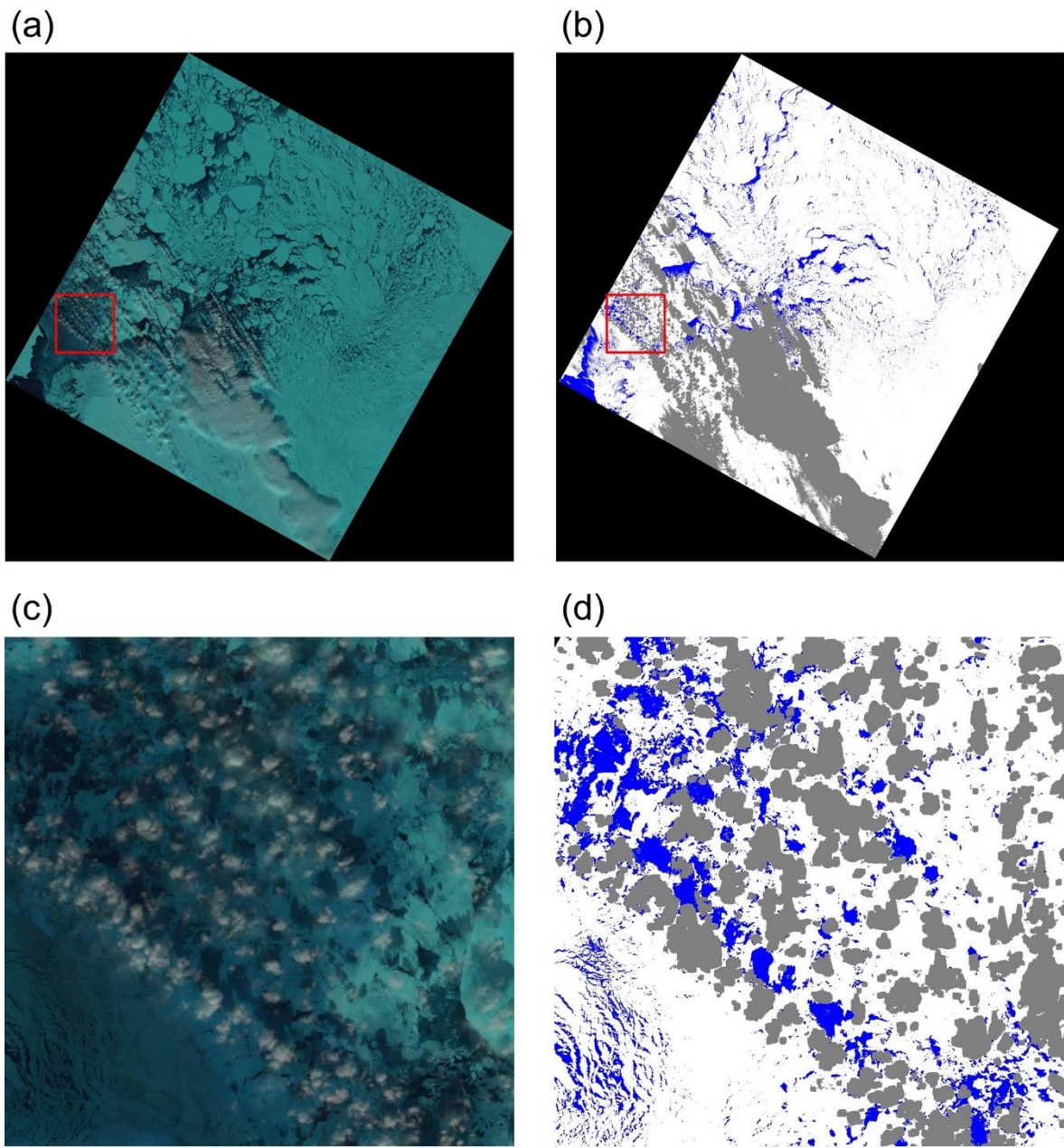
Figure B2: The case of a Landsat-8 scene classified as C1 (i.e., underestimated cloud cover) from the visual inspection step. Shown in the panels are (a) full size true-colour image, (b) full size cloud mask array, (c) true-colour image of the area enclosed by the red rectangle in (a) and (b), and (d) cloud mask array of the area enclosed by the red rectangle in (a) and (b). The blue, white, grey, and black pixels in (b) and (d) are open water, ice, cloud, and fill value pixels, respectively. The scene is from Mar. 25, 2022, over the Barents Sea. The true-colour image is obtained from Earth Resources Observation and Science (EROS) Center (2020).

760

Appendix CB: Validation of Ice and Open Water Classification
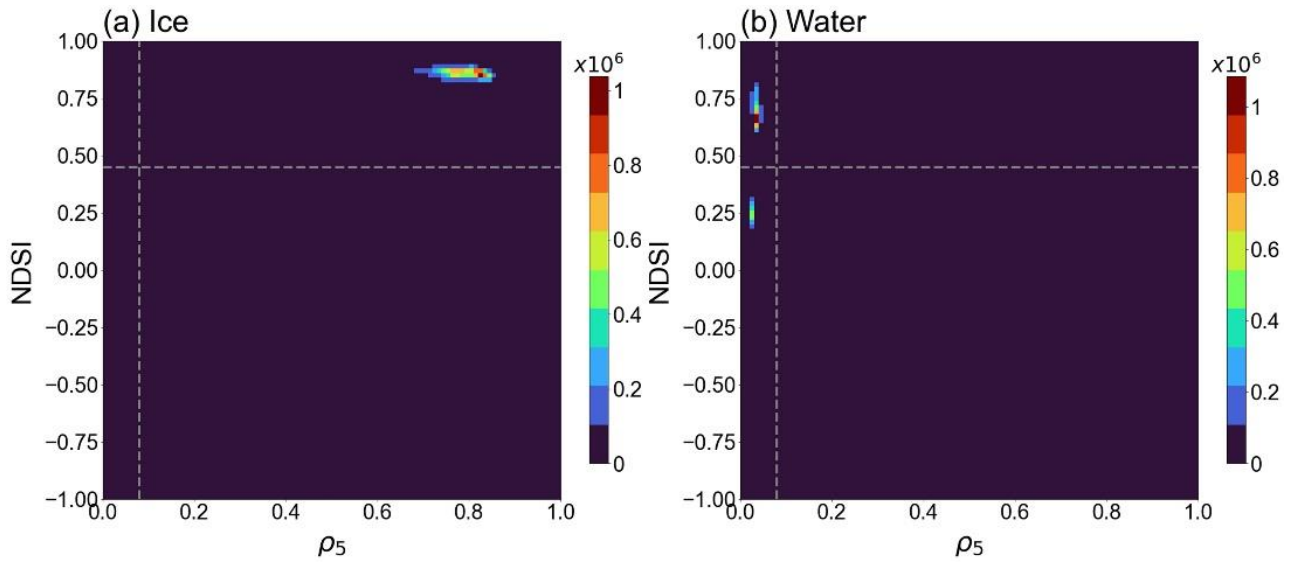
765

Figure CB1: Scatterplot between NDSI and ρ_5 for (a) ice and (b) open water. The values for ice and open water pixels were collected using the ice/water surface classification map (Kern, 2021) as reference data. The thresholds for NDSI and ρ_5 used in this study are shown by the white dashed lines. The colorbars denote the number of pixels.
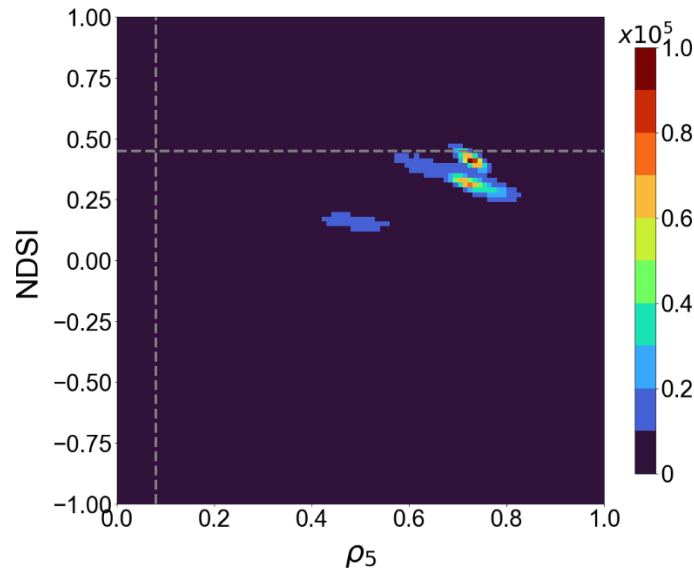
770

Figure CB2: Scatterplot between NDSI and ρ_5 for cloud pixels that remain unmasked after the application of CFMask. The pixels are acquired from ten select Landsat-8 images categorized as C1. The thresholds for NDSI and ρ_5 used in this study are shown by the white dashed lines. The colorbars denote the number of pixels.

775

Appendix DC: Uncertainty of Landsat-8 SIC With Respect To ~~Sub~~-Region, Cloud Contamination Label, an SIC Sub-Range

$C_{\rho5}$ [%]	C_{NDSI} [%]	σ_{SIC} [%]
99.66	0.34	0.56

Table DC1: Contributions from ρ_5 ($C_{\rho5}$) and NDSI (C_{NDSI}) to the estimated uncertainty of SIC (σ_{SIC}) and σ_{SIC} over all 480 scenes.

780

Region	$C_{\rho 5}$ [%]	C_{NDSI} [%]	σ_{SIC} [%]
Baffin Bay	99.74	0.26	0.80
Barents Sea	99.84	0.16	0.65
Beaufort Sea	99.33	0.67	0.30
Bering Sea	97.46	2.54	0.89
Canadian A.	99.93	0.07	0.25
Central Arctic	99.86	0.14	0.56
Chukchi Sea	99.97	0.03	0.45
E. Greenland	99.58	0.42	0.65
E. Siberian	100.00	0.00	0.53
Hudson Bay	98.48	1.52	0.54
Kara Sea	99.23	0.77	0.43
Laptev Sea	99.99	0.01	0.63

Table DC2: Contributions from ρ_5 ($C_{\rho 5}$) and NDSI (C_{NDSI}) to the estimated uncertainty of SIC (σ_{SIC}) and σ_{SIC} for the twelve sub-regions.

785

Cloud Contamination Category	$C_{\rho 5}$[%]	C_{NDSI} [%]	σ_{SIC} [%]
C1	97.10	2.90	0.65
C2	100.00	0.00	0.50
C3	99.99	0.01	0.66
C4	100.00	0.00	0.40

Table DC3: Contributions from ρ_5 ($C_{\rho 5}$) and NDSI (C_{NDSI}) to the estimated uncertainty of SIC (σ_{SIC}) and σ_{SIC} for the three cloud contamination categories.

790

SIC sub-range [%]	$C_{\rho 5}$ [%]	C_{NDSI} [%]	σ_{SIC} [%]
0-10	99.87	0.13	0.11
10-20	99.96	0.04	2.16
20-30	99.98	0.02	3.45
30-40	99.97	0.03	3.99
40-50	99.97	0.03	4.15
50-60	99.98	0.02	4.46
60-70	99.99	0.01	4.11
70-80	99.99	0.01	3.61
80-90	99.99	0.01	2.25
90-100	100.00	0.00	0.19

Table DC4: Contributions from ρ_5 ($C_{\rho 5}$) and NDSI (C_{NDSI}) to the estimated uncertainty of SIC (σ_{SIC}) and σ_{SIC} for varying SIC sub-range.

Author Contribution

HJ contributed to the conceptualization, investigation, methodology, and software of the research, and wrote the original manuscript. SL contributed to the conceptualization and methodology of the research, review & editing of the manuscript, and provided supervision throughout the research progress. JK contributed to the funding acquisition and review & editing of the manuscript. KL contributed to the conceptualization and review & editing of the manuscript.

Competing Interests

The authors declare that they have no conflict of interest.

Acknowledgements

This work was supported by Korea Polar Research Institute (KOPRI) Grant entitled "Development and Application of the Earth System Model-Based Korea Polar Prediction System (KPOP-Earth) for the Arctic and Midlatitude High-Impact Weather Event" funded by the Ministry of Oceans and Fisheries under Grant KOPRI PE23010.

References

810   Agnew, T., and Howell, S.: The use of operational ice charts for evaluating passive microwave ice concentration data, Atmosphere-Ocean, 41(4), 317-331, doi: https://doi.org/10.3137/ao.410405, 2010.

Andersen, S., Tonboe, R., Kaleschke, L., Heygster, G., and Pedersen, L. T.: Intercomparison of passive microwave sea ice concentration retrievals over the high-concentration Arctic sea ice, J. Geophys. Res., 112, C08004, doi: https://doi.org/10.1029/2006JC003543, 2007.

815   Arctic Ocean – Sea Ice Concentration Charts – Svalbard and Greenland, E.U. Copernicus Marine Service Information (CMEMS), Marine Data Store (MDS), doi: https://doi.org/10.48670/moi-00128, accessed on 11 June 2024.

Bolsenga, S. J.: Spectral reflectances of snow and fresh-water ice from 340 through 1100 nm, J. Glaciol., 29, 296-305, doi: https://doi.org/10.3189/S0022143000008352, 1983.

Cavalieri, D. J., Gloersen, P., and Campbell, W. J.: Determination of sea ice parameters with the Nimbus 7 SMMR, J.
820   Geophys. Res., 89, 5355-5369, doi: https://doi.org/10.1029/JD089iD04p05355, 1984.

Cavalieri, D. J., Germain, K. M., and Swift, C. T.: Reduction of weather effects in the calculation of sea-ice concentration with the DMSP SSM/I, J. of Glaciol., 41, 455-464, doi: https://doi.org/10.3189/S0022143000034791, 1995.

Cavalieri, D. J., Markus, T., Hall, D. K., Gasiewski, A. J., Klein, M., and Ivanoff, A.: Assessment of EOS Aqua AMSR-E Arctic Sea Ice Concentration Using Landsat-7 and Airborne Microwave Imagery, IEEE T. Geosci. Remote, 44, 3057-3069,
825   doi: https://doi.org/10.1109/TGRS.2006.878445, 2006.

Cavalieri, D. J., Markus, T., Hall, D. K., Ivanoff A., and Glick E.: Assessment of AMSR-E Antarctic Winter Sea-Ice Concentrations Using Aqua MODIS, IEEE T. Geosci. Remote, 48, 3331-3339, doi: https://doi.org/10.1109/TGRS.2010.2046495, 2010.

Cavalieri, D. J. and Parkinson, C. L.: Arctic sea ice variability and trends, 1979-2010, The Cryosphere, 6, 881-889, doi:
830   https://doi.org/10.5194/tc-6-881-2012, 2012.

Cheng, A., Casati, B., Tivy, A., Zagon, T., Lemieux, J. F., Tremblay, L. B.: Accuracy and inter-analyst agreement of visually estimated sea ice concentrations in Canadian Ice Service ice charts using single-polarization RADARSAT-2, The Cryosphere, 14, 1289-1310, doi: https://doi.org/10.5194/tc-14-1289-2020, 2020.

Chi, J., Kim, H. C., Lee, S., and Crawford, M. M.: Deep learning based retrieval algorithm for Arctic sea ice concentration
835   from AMSR2 passive microwave and MODIS optical data, Remote Sens. Environ., 231, doi: https://doi.org/10.1016/j.rse.2019.05.023, 2019.

Comiso, J. C., Ackley, S. F., and Gordon, A. L.: Antarctic sea ice microwave signatures and their correlation with in situ ice observations, J. Geophys. Res.-Oceans, 89, 662-672, doi: https://doi.org/10.1029/JC089iC01p00662, 1984.

Comiso, J. C.: SSM/I concentrations using the bootstrap algorithm, United States: National Aeronautics and Space
840   Administration, Goddard Space Flight Center, 1995.

Comiso, J. C., Cavalieri, D. J., Parkinson, C. L., and Gloersen, P.: Passive Microwave Algorithm for Sea Ice Concentration: A Comparison of Two Techniques, Remote Sens. Environ., 60, 357-384, doi: https://doi.org/10.1016/S0034-4257(96)00220-9, 1997.

845 Comiso, J. C. and Steffen, K.: Studies of Antarctic sea ice concentrations from satellite data and their applications, J. Geophys. Res., 106, 31361-31385, doi: https://doi.org/10.1029/2001JC000823, 2001.

Comiso, J. C., Meier, W. N., and Gersten, R.: Variability and trends in the Arctic Sea ice cover: Results from different techniques, J. Geophys. Res.-Oceans, 122, 6883-6900, doi: https://doi.org/10.1002/2017JC012768, 2017.

Drüe, C. and Heinemann G.: High-resolution maps of the sea-ice concentration from MODIS satellite data, Geophys. Res. Lett., 31(20), doi: https://doi.org/10.1029/2004GL020808, 2004.

850 Earth Resources Observation and Science (EROS) Center.: Landsat 8-9 Operational Land Imager / Thermal Infrared Sensor Level-1, Collection 2 [dataset], U.S. Geological Survey, doi: https://doi.org/10.5066/P975CC9B, 2020.

Fetterer, F. and Untersteiner, N.: Observations of melt ponds on Arctic sea ice, J. Geophys. Res., 103, 24821-24825, doi: https://doi.org/10.1029/98JC02034, 1998.

Foga, S., Scaramuzza, P. L., Guo, S., Zhu, Z., Dilley, R. D., Beckmann, T., Schmidt, G. L., Dwyer, J. L., Hughes, M. J., and 855 Laue, B., Cloud detection algorithm comparison and validation for operational Landsat data products, Remote Sens. Environ., 194, 379-390, doi: https://doi.org/10.1016/j.rse.2017.03.026, 2017.

Gloersen, P. and Cavalieri, D. J.: Reduction of weather effects in the calculation of sea ice concentration from microwave radiances, J. Geophys. Res., 91, 3913-3919, doi: https://doi.org/10.1029/JC091iC03p03913, 1986.

Hall, D. K., Riggs, G. A., and Salomonson, V. V.: Development of Methods for Mapping Global Snow Cover Using 860 Moderate Resolution Imaging Spectroradiometer Data, Remote Sens. Environ., 54, 127-140, doi: https://doi.org/10.1016/0034-4257(95)00137-P, 1995.

Hall, D. K., Riggs, G. A., Salomonson, V. V., Barton, J. S., Casey, K., Chien, J., DiGirolamo, N. E., Klein, A. G., Powell, H. W., and Tait, A. B.: Algorithm Theoretical Basis Document for the MODIS snow and Sea Ice-Mapping Algorithms, NASA Goddard Spaceflight Center, 2001.

865 Han, H. and Kim, H. C.: Evaluation of summer passive microwave sea ice concentrations in the Chukchi Sea based on KOMPSAT-5 SAR and numerical weather prediction data, Remote Sens. Environ., 209, 343-362, doi: https://doi.org/10.1016/j.rse.2018.02.058, 2018.

Honda, M., Inoue, J., and Yamane, S.: Influence of low Arctic sea-ice minima on anomalously cold Eurasian winters, Geophys. Res. Lett., 36(8), doi: https://doi.org/10.1029/2008GL037079, 2009.

870 Horvat, C., Buckley, E., Stewart, M., Yoosiri, P., and Wilhelmus, M. M.: Linear Ice Fraction: Sea Ice Concentration Estimates from the ICESat-2 Laser Altimeter, EGUsphere [preprint], doi: https://doi.org/10.5194/egusphere-2023-2312, 2023.

Ivanova, N., Johannessen, O. M., Pedersen, L. T., and Tonboe, R. T.: Retrieval of Arctic Sea Ice Parameters by Satellite Passive Microwave Sensors: A Comparison of Eleven Sea Ice Concentration Algorithms, IEEE T. Geosci. Remote, 52, 7233-7246, doi: https://doi.org/10.1109/TGRS.2014.2310136, 2014.

Ivanova, N., Pedersen, L. T., Tonboe, R. T., Kern, S., Heygster, G., Lavergne, T., Sørensen, A., Saldo, R., Dybkjær, G., Brucker, L., and Shokr, M.: Inter-comparison and evaluation of sea ice algorithms: towards further identification of challenges and optimal approach using passive microwave observations, The Cryosphere, 9, 1797-1817, doi: https://doi.org/10.5194/tc-9-1797-2015, 2015.

Jaiser, R., Dethloff, K., Handorf, D., Rinke, A., and Cohen, J.: Impact of sea ice cover changes on the Northern Hemisphere atmospheric winter circulation, Tellus A: Dynamic Meteorology and Oceanography, 64, 1, doi: https://doi.org/10.3402/tellusa.v64i0.11595, 2012.

Jung, H. S., Lee, S. M., Kim, J. H., and Lee, K.: Arctic sea ice concentration data record in 6.25 km polar stereographic grid from three-year Landsat-8 imagery [Dataset], Zenodo, doi: https://zenodo.org/doi/10.5281/zenodo.10973297, 2024.

Jung, H. S.: Software of Arctic sea ice concentration data record in 6.25 km polar stereographic grid from three-year Landsat-8 imagery [Code], Zenodo, doi: https://zenodo.org/doi/10.5281/zenodo.12754603, 2024.

Kaleschke, L., Lüpkes, C., Vihma, T., Harrpaintner, J., Bochert, A., Hartmann, J., Heygster, G.: SSM/I sea ice remote sensing for mesoscale ocean-atmosphere interaction studies, Can. J. Remote Sens., 27(5), 526-537, doi: https://doi.org/10.1080/07038992.2001.10854892, 2001.

Karvonen, J.: Baltic Sea Ice Concentration Estimation Using SENTINEL-1 SAR and AMSR2 Microwave Radiometer Data, IEEE. T. Geosci. Remote., 55, 2871-2883, doi: https://doi.org/10.1109/TGRS.2017.2655567, 2017.

Kern, S.: Landsat surface type over water from supervised classification of surface broadband albedo estimates (Version_2021_fv0.01) [Dataset], doi: http://doi.org/10.25592/uhhfdm.9181, 2021.

Kern, S., Lavergne, T., Pedersen, L. T., Tonboe, R. T., Bell, L., Meyer, M., and Zeigermann, L.: Satellite passive microwave sea-ice concentration data set intercomparison using Landsat data, The Cryosphere, 16, 349-378, doi: https://doi.org/10.5194/tc-16-349-2022, 2022.

Kim, B. M., Son, S. W., Min, S. K., Jeong, J. H., Kim, S. J., Zhang, X., Shim, T., and Yoon, J. H.: Weakening of the stratospheric polar vortex by Arctic sea-ice loss, Nature Communications, 5, 4646, doi: https://doi.org/10.1038/ncomms5646, 2014.

Liu, Y., Key, J., and Mahoney, R.: Sea and Freshwater Ice Concentration from VIIRS on Suomi NPP and the Future JPSS Satellites, Remote Sens., 8(6), 523, doi: https://doi.org/10.3390/rs8060523, 2016.

Ludwig, V., Spreen, G., and Pedersen, L. T.: Evaluation of a New Merged Sea-Ice Concentration Dataset at 1km Resolution from Thermal Infrared and Passive Microwave Satellite Data in the Arctic, Remote Sens., 12(19), 3183, doi: https://doi.org/10.3390/rs12193183, 2020.

Malinka, A., Zege, E., Istomina, L., Heygster, G., Spreen, G., Perovich, D. K., and Polashenski, C.: Reflective properties of melt ponds on sea ice, The Cryosphere, 12, 1921-1937, doi: https://doi.org/10.5194/tc-12-1921-2018, 2018.

Markus, T., Cavalieri, D. J., and Ivanoff, A.: The potential of using Landsat 7 ETM+ for the classification of sea-ice surface conditions during summer, Ann. Glaciol, 34, 415-419, doi: https://doi.org/10.3189/172756402781817536, 2002.

Meier, W. N., and Notz, D.: A note on the accuracy and reliability of satellite-derived passive microwave estimates of sea-ice extent, Clic Arctic sea ice working group, Consensus document, CLIC International Project Office, Tromsø, Norway, 2010.

Meier, W. N., Hovelsrud, G. K., van Oort, B. E.H., Key, J. R., Kovacs, K. M., Michel, C., Hass, C., Granskog, M. A., Gerland, S., Perovich, D. K., Makshtas, A., and Reist, J. D.: Arctic sea ice in transformation: A review of recent observed changes and impacts on biology and human activity, Rev. Geophys., 51, 185-217, doi: https://doi.org/10.1002/2013RG000431, 2014.

Meier, W. N., Fetterer, F., Windnagel, A. K., and Stewart, J. S.: NOAA/NSIDC Climate Data Record of Passive Microwave Sea Ice Concentration, Version 4, Boulder CO, USA, NSIDC: National Snow and Ice Data Center, doi: https://doi.org/10.7265/efmz-2t65, 2021.

Meier, W. N. and Stroeve, J.: An updated assessment of the changing Arctic sea ice cover, Oceanography, vol. 35, 10-19, doi: https://doi.org/10.5670/oceanog.2022.114, 2022.

Meier, W. N. and Stewart, J. S.: Arctic and Antarctic Regional Masks for Sea Ice and Related Data Products, Version 1 [Data Set]. Boulder, Colorado USA. National Snow and Ice Data Center, doi: https://doi.org/10.5067/CYW3O8ZUNIWC, 2023.

Meier, W. N. and Stewart, J. S.: NSIDC Land, Ocean, Coast, Ice, and Sea Ice Region Masks, NSIDC Special Report 25, Boulder CO, USA: National Snow and Ice Data Center, https://nsidc.org/sites/default/files/documents/technical-reference/nsidc-special-report-25.pdf, 2023.

NASA: The Worldwide Reference System, a Joint NASA/USGS Earth Observation Program, accessed [16-03-2024], https://landsat.gsfc.nasa.gov/about/the-worldwide-reference-system/, last access: 16 March 2024, 2021.

Neihaus, H. and Spreen, G.: Melt pond fraction on Arctic sea-ice from Sentinel-2 satellite optical imagery (2017-2021) [Dataset], PANGAEA, doi: https://doi.org/10.1594/PANGAEA.950885, 2022.

Neihaus, H., Spreen, G., Birnbaum, G., Istomina, L., Jäkel, E., Linhardt, F.: Sea Ice Melt Pond Fraction Derived From Sentinel-2 Data: Along the MOSAiC Drift and Arctic-Wide, Geophys. Res. Lett., 50(5), doi: https://doi.org/10.1029/2022GL102102, 2023.

Park, J. W., Korosov, A. A., Babiker, M., Won, J. S., Hansen, M. W., and Kim, H. C.: Classification of sea ice types in Sentinel-1 synthetic aperture radar images, The Cryosphere, 14, 2629-2645, doi: https://doi.org/10.5194/tc-14-2629-2020, 2020.

Parkinson, C. L., Comiso, J. C., Zwally, H. J., Cavalieri, D. J., Gloersen, P., and Campbell, W. J.: Arctic Sea Ice, 1973-1976: Satellite Passive-Microwave Observations, NASA SP-489, National Aeronautics and Space Administration, 296 pp, 1987.

Perovich, D. K.: The optical properties of sea ice, CRREL Monograph 9-61, US Army Corps of Engineers, 1996.

940 Qiu, S., Zhu, Z., and He, B.: Fmask 4.0: Improved cloud and cloud shadow detection in Landsats 4-8 and Sentinel-2 imagery, Remote Sens. Environ., 231, 111205, doi: https://doi.org/10.1016/j.rse.2019.05.024, 2019.

Riggs, G. A., Hall, D. K., and Salomonson, V. V.: Recent Progress in Development of the Moderate Resolution Imaging Spectroradiometer Snow Cover Algorithm and Product, 1996 International Geoscience and Remote Sensing Symposium, Lincoln, NE, USA, 1, 139-141, doi: https://doi.org/10.1109/IGARSS.1996.516270, 1996.

945 Riggs, G. A., Hall, D. K, and Ackerman, S. A.: Sea Ice Extent and Classification Mapping with the Moderate Resolution Imaging Spectroradiometer Airborne Simulator, Remote Sens. Environ., 68, 152-163, doi: https://doi.org/10.1016/S0034-4257(98)00107-2, 1999.

Rösel, A. and Kaleschke, L.: Comparison of different retrieval techniques for melt ponds on Arctic sea ice from Landsat and MODIS satellite data, Ann. Glaciol., 52, 185-191, doi: https://doi.org/10.3189/172756411795931606, 2011.

950 Rösel, A., Kaleschke, L., and Birnbaum, G.: Melt ponds on Arctic sea ice determined from MODIS satellite using an artificial neural network, The Cryosphere, 6(2), 431-446, doi: https://doi.org/10.5194/tc-6-431-2012, 2012.

Shi, H., Lee, S. M., Sohn, B. J., Gasiewski, A. J., Meier, W. N., Dybkjær, G., and Kim, S. W.: Estimation of Arctic Winter Snow Depth, Sea Ice Thickness and Bulk Density, and Ice Freeboard by Combining CryoSat-2, AVHRR, and AMSR Measurements, IEEE T. Geosci. Remote., 61, 1-18, doi: https://doi.org/10.1109/tgrs.2023.3265274, 2023.

955 Song, K. and Minnett, P. J.: Evaluation of Summertime Passive Microwave and Reanalysis Sea-Ice Concentration in the Central Arctic, Earth and Space Science, 11, doi: https://doi.org/10.1029/2023EA003214, 2024.

Spreen, G., Kaleschke, L., and Heygster, G.: Sea ice remote sensing using AMSR-E 89-GHz channels, J. Geophys. Res., 113, C02S03, doi: https://doi.org/10.1029/2005JC003384, 2008.

Svendsen, E., Matzler, C., and Grenfell, T. C.: A model for retrieving total sea ice concentration from a spaceborne dual-

960 polarized passive microwave instrument operating near 90 GHz, Int. J. Remote Sens., 8, 1479-1487, doi: https://doi.org/10.1080/01431168708954790, 1987.

Tanaka, Y. and Lu, J.: A New Sea Ice Concentration Retrieval Algorithm Based on Relationship Between AMSR2 89-GHz Polarization and Landsat 8 Observations, IEEE. T. Geosci. Remote, 61, 1-15, doi: https://doi.org/10.1109/TGRS.2023.3257401, 2023.

965 Tarrio, K., Tang, X., Masek, J. G., Claverie, M., Ju, J., Qiu, S., Zhu, Z., Woodcock, C. E.: Comparison of cloud detection algorithms for Sentinel-2 imagery, Sci. Remote Sens. 2,, 100010, doi: https://doi.org/10.1016/j.srs.2020.100010, 2020.

Tonboe, R. T., Eastwood, S., Lavergne, T., Sørensen, A. M., Rathmann, N., Dybkjær, G., Pedersen, L. T., Høyer, J. L., and Kern, S.: The EUMETSAT sea ice concentration climate data record, The Cryosphere, 10, 2275-2290, doi: https://doi.org/10.5194/tc-10-2275-2016, 2016.

970 Trewin, B., Cazenave, A., Howell, S., Huss, M., Isensee, K., Palmer, M. D., Tarasova, O., and Vermeulen, A.: Headline Indicators for Global Climate Monitoring, Bull. Amer. Meteor. Soc., 102, E20-E37, doi: https://doi.org/10.1175/BAMS-D-19-0196.1, 2021.

Untersteiner, N.: On the mass and heat budget of arctic sea ice, Archiv für Meteorologie, Geophysik und Bioklimatologie, Serie A, 12(2), 151–182, doi: https://doi.org/10.1007/bf02247491, 1961.

975 Zanter, K.: Landsat 8 (L8) Data Users Handbook, LDSD-1574, Version 5, https://www.usgs.gov/landsat-missions/landsat-8-data-users-handbook, 2019.

Zhu, Z. and Woodcock, C. E.: Object-based cloud and cloud shadow detection in Landsat imagery, Remote Sens. Environ., 118, 83-94, doi: https://doi.org/10.1016/j.rse.2011.10.028, 2012.

Zhu, Z., Wang, S., and Woodcock, C. E.: Improvement and expansion of the Fmask algorithm: cloud, cloud shadow, and
980 snow detection for Landsats 4-7, 8, and Sentinel 2 images, Remote Sens. Environ., 159, 269-277, doi: http://dx.doi.org/10.1016/j.rse.2014.12.014, 2015.

Supplements of

Arctic sea ice concentration data record in 6.25 km polar stereographic grid from three-year Landsat-8 imagery

Hee-Sung Jung[1], Sang-Moo Lee[1,2], Joo-Hong Kim[3], and Kyungsoo Lee[1]

[1]Department of Earth and Environmental Sciences, Seoul National University, Seoul, 08826, Republic of Korea
[2]Institute for Data Innovation in Science, Seoul National University, Seoul, 08826, Republic of Korea
[3]Korea Polar Research Institute, Incheon, 21990, Republic of Korea

Correspondence to: Sang-Moo Lee (sangmoolee@snu.ac.kr)

S1 Number of available Landsat-8 images subject to varying cloud cover thresholds
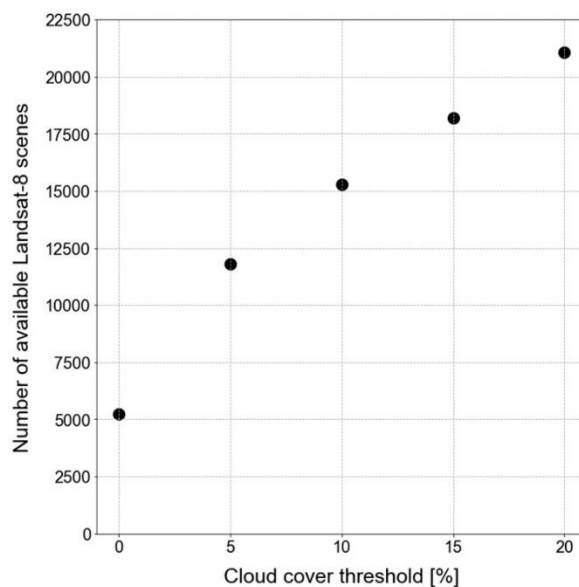
Figure S1: Number of available Landsat-8 images (y-axis) subject to values of different cloud cover thresholds (x-axis) during the period of Jan. 2020 – Dec. 2022 over pan-Arctic areas.

Cloud cover threshold [%]	0	5	10	15	20
Number of available Landsat-8 scenes	5,231	11,787	15,286	18,177	21,060

Table S1: Number of available Landsat-8 images subject to values of different cloud cover thresholds during the period of Jan. 2020 – Dec. 2022 over pan-Arctic areas.

S2~~1~~ Evaluation of Ice And Open Water Classification Over Clear Pixels
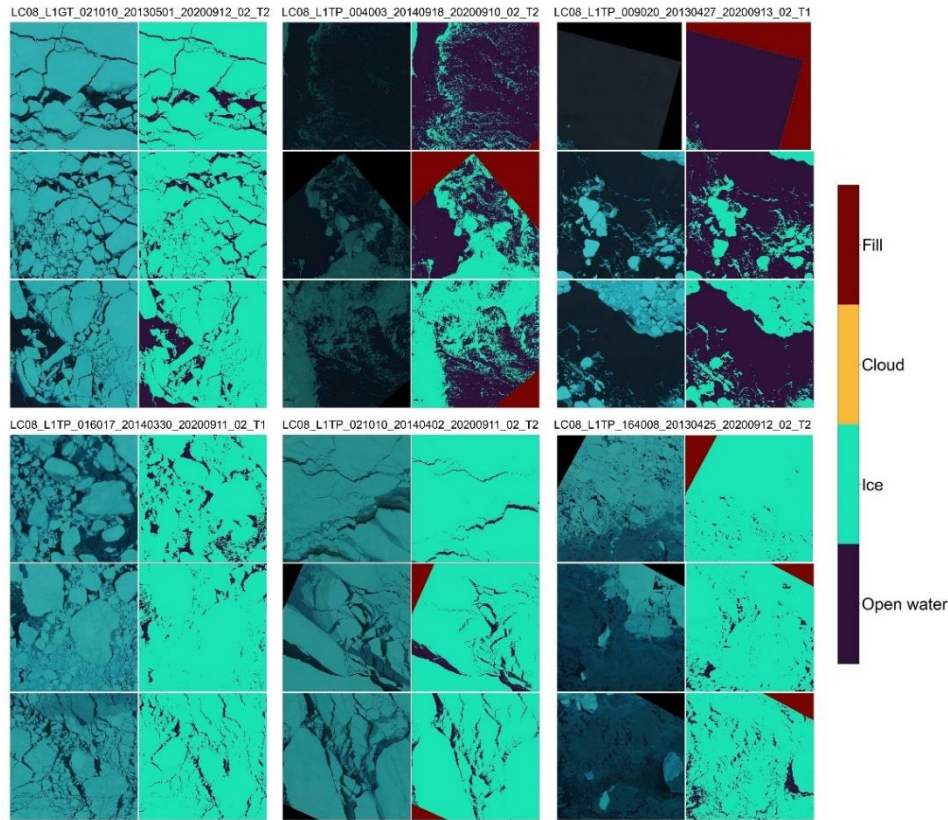
Figure S2~~1~~: Sub-sections of the 6 scenes used for the test of ice and open water classification over clear pixels. True-color images (~~left~~right of each panel) and the reference classification map that our method produced (right~~left~~ of each panel) are provided. Each pixel in the scene belong to open water (dark purple), ice (mint), or cloud (yellow). Red colour indicates the fill values. The true-color images were downloaded from United States Geological Survey Earth Explorer (**https://earthexplorer.usgs.gov/**, last access: May 22, 2024).

Year	Filename
2013	LC08_L1GT_021010_20130501_20200912_02_T2
	LC08_L1TP_009020_20130427_20200913_02_T1
	LC08_L1TP_164008_20130425_20200912_02_T2
2014	LC08_L1TP_004003_20140918_20200910_02_T2
	LC08_L1TP_016017_20140330_20200911_02_T1
	LC08_L1TP_021010_20140402_20200911_02_T2

Table S2: List of Landsat-8 scenes used to test the performance of ice and open water classification over clear pixels.

S3 Evaluation of Landsat-8 SIC Using Ice Chart

Cloud contamination label	Region	Filename (Landsat)	Filename (Ice chart)	Time Difference [sec]
	Barents_Sea	LC08_L1TP_221244_20210430_20210508_02_T2	ice_conc_svalbard_202104301500.nc	1397
	Barents_Sea	LC08_L1TP_226243_20210503_20210508_02_T2	ice_conc_svalbard_202105031500.nc	3225
	Barents_Sea	LC08_L1GT_222242_20210507_20210517_02_T2	ice_conc_svalbard_202105071500.nc	1717
	Barents_Sea	LC08_L1TP_214243_20210803_20210811_02_T1	ice_conc_svalbard_202108031500.nc	-1191
	Barents_Sea	LC08_L1TP_221242_20210804_20210811_02_T1	ice_conc_svalbard_202108041500.nc	1381
	Barents_Sea	LC08_L1TP_214245_20220518_20220525_02_T2	ice_conc_svalbard_202205181500.nc	-1151
	Barents_Sea	LC08_L1TP_225243_20220718_20220726_02_T1	ice_conc_svalbard_202207181500.nc	2899
	East_Greenland_Sea	LC08_L1TP_229012_20210305_20210312_02_T1	ice_conc_svalbard_202103051500.nc	-1164
	East_Greenland_Sea	LC08_L1TP_225011_20210309_20210317_02_T1	ice_conc_svalbard_202103091500.nc	-2673
	East_Greenland_Sea	LC08_L1TP_224011_20210318_20210328_02_T2	ice_conc_svalbard_202103181500.nc	-3049
	East_Greenland_Sea	LC08_L1TP_227011_20210323_20210402_02_T1	ice_conc_svalbard_202103231500.nc	-1937
	East_Greenland_Sea	LC08_L1TP_225010_20210325_20210402_02_T2	ice_conc_svalbard_202103251500.nc	-2703
	East_Greenland_Sea	LC08_L1TP_003005_20210407_20210415_02_T1	ice_conc_svalbard_202104071500.nc	1253
	East_Greenland_Sea	LC08_L1TP_227008_20210408_20210416_02_T2	ice_conc_svalbard_202104081500.nc	-2013
	East_Greenland_Sea	LC08_L1TP_001004_20210409_20210416_02_T2	ice_conc_svalbard_202104091500.nc	486
	East_Greenland_Sea	LC08_L1TP_006004_20210412_20210423_02_T1	ice_conc_svalbard_202104121500.nc	2339
	East_Greenland_Sea	LC08_L1TP_230006_20210413_20210423_02_T1	ice_conc_svalbard_202104131500.nc	-951
	East_Greenland_Sea	LC08_L1TP_004004_20210414_20210423_02_T2	ice_conc_svalbard_202104141500.nc	1597
	East_Greenland_Sea	LC08_L1TP_228007_20210415_20210424_02_T1	ice_conc_svalbard_202104151500.nc	-1669
	East_Greenland_Sea	LC08_L1TP_005004_20210421_20210430_02_T1	ice_conc_svalbard_202104211500.nc	1964
	East_Greenland_Sea	LC08_L1TP_008003_20210426_20210501_02_T1	ice_conc_svalbard_202104261500.nc	3050
	East_Greenland_Sea	LC08_L1TP_004003_20210430_20210508_02_T1	ice_conc_svalbard_202104301500.nc	1564
	East_Greenland_Sea	LC08_L1TP_007004_20210505_20210517_02_T1	ice_conc_svalbard_202105051500.nc	2697
	East_Greenland_Sea	LC08_L1TP_005004_20210507_20210517_02_T1	ice_conc_svalbard_202105071500.nc	1955
	East_Greenland_Sea	LC08_L1TP_225011_20210512_20210524_02_T1	ice_conc_svalbard_202105121500.nc	-2695
	East_Greenland_Sea	LC08_L1TP_002004_20210518_20210528_02_T1	ice_conc_svalbard_202105181500.nc	851
	East_Greenland_Sea	LC08_L1TP_226011_20210519_20210528_02_T1	ice_conc_svalbard_202105191500.nc	-2319
	East_Greenland_Sea	LC08_L1TP_233006_20210520_20210528_02_T1	ice_conc_svalbard_202105201500.nc	158
C1	East_Greenland_Sea	LC08_L1TP_003005_20210525_20210529_02_T1	ice_conc_svalbard_202105251500.nc	1249
	East_Greenland_Sea	LC08_L1TP_002005_20210603_20210614_02_T1	ice_conc_svalbard_202106031500.nc	883
	East_Greenland_Sea	LC08_L1TP_009003_20210604_20210614_02_T1	ice_conc_svalbard_202106041500.nc	3431
	East_Greenland_Sea	LC08_L1TP_230006_20210616_20210622_02_T1	ice_conc_svalbard_202106161500.nc	-943
	East_Greenland_Sea	LC08_L1TP_001004_20210628_20210707_02_T1	ice_conc_svalbard_202106281500.nc	496
	East_Greenland_Sea	LC08_L1TP_003005_20210712_20210720_02_T1	ice_conc_svalbard_202107121500.nc	1262
	East_Greenland_Sea	LC08_L1TP_001006_20210714_20210721_02_T1	ice_conc_svalbard_202107141500.nc	545
	East_Greenland_Sea	LC08_L1TP_005004_20210726_20210804_02_T1	ice_conc_svalbard_202107261500.nc	1987
	East_Greenland_Sea	LC08_L1TP_003004_20210728_20210804_02_T1	ice_conc_svalbard_202107281500.nc	1246
	East_Greenland_Sea	LC08_L1TP_007004_20210809_20210819_02_T1	ice_conc_svalbard_202108091500.nc	2734
	East_Greenland_Sea	LC08_L1TP_225010_20210816_20210826_02_T1	ice_conc_svalbard_202108161500.nc	-2683
	East_Greenland_Sea	LC08_L1TP_232006_20210817_20210827_02_T1	ice_conc_svalbard_202108171500.nc	-182
	East_Greenland_Sea	LC08_L1TP_006004_20210818_20210827_02_T1	ice_conc_svalbard_202108181500.nc	2366
	East_Greenland_Sea	LC08_L1TP_007004_20210825_20210901_02_T1	ice_conc_svalbard_202108251500.nc	2739
	East_Greenland_Sea	LC08_L1TP_227012_20210830_20210909_02_T1	ice_conc_svalbard_202108301500.nc	-1889
	East_Greenland_Sea	LC08_L1TP_006003_20210903_20210910_02_T2	ice_conc_svalbard_202109031500.nc	2347
	East_Greenland_Sea	LC08_L1TP_226012_20210908_20210916_02_T1	ice_conc_svalbard_202109081500.nc	-2257
	East_Greenland_Sea	LC08_L1TP_227011_20210915_20210925_02_T1	ice_conc_svalbard_202109151500.nc	-1909
	East_Greenland_Sea	LC08_L1TP_001006_20220412_20220419_02_T1	ice_conc_svalbard_202204121500.nc	540
	East_Greenland_Sea	LC08_L1TP_225011_20220413_20220420_02_T2	ice_conc_svalbard_202204131500.nc	-2677
	East_Greenland_Sea	LC08_L1TP_002005_20220419_20220427_02_T1	ice_conc_svalbard_202204191500.nc	886
	East_Greenland_Sea	LC08_L1TP_226009_20220420_20220427_02_T1	ice_conc_svalbard_202204201500.nc	-2356
	East_Greenland_Sea	LC08_L1TP_233006_20220421_20220428_02_T1	ice_conc_svalbard_202204211500.nc	168
	East_Greenland_Sea	LC08_L1TP_007004_20220422_20220428_02_T1	ice_conc_svalbard_202204221500.nc	2716
	East_Greenland_Sea	LC08_L1TP_229007_20220425_20220503_02_T1	ice_conc_svalbard_202204251500.nc	-1293
	East_Greenland_Sea	LC08_L1TP_003005_20220426_20220503_02_T1	ice_conc_svalbard_202204261500.nc	1254
	East_Greenland_Sea	LC08_L1TP_001005_20210916_20210925_02_T1	ice_conc_svalbard_202109161500.nc	543
	East_Greenland_Sea	LC08_L1TP_228012_20210922_20210930_02_T1	ice_conc_svalbard_202109221500.nc	-1514
	East_Greenland_Sea	LC08_L1TP_227011_20211001_20211013_02_T1	ice_conc_svalbard_202110011500.nc	-1904

	Region	Scene ID	Ice concentration file	Value
	East_Greenland_Sea	LC08_L1TP_229012_20220324_20220330_02_T1	ice_conc_svalbard_202203241500.nc	-1171
	East_Greenland_Sea	LC08_L1TP_232005_20220329_20220405_02_T2	ice_conc_svalbard_202203291500.nc	-231
	East_Greenland_Sea	LC08_L1TP_006004_20220330_20220406_02_T1	ice_conc_svalbard_202203301500.nc	2341
	East_Greenland_Sea	LC08_L1TP_230008_20220331_20220406_02_T1	ice_conc_svalbard_202203311500.nc	-901
	East_Greenland_Sea	LC08_L1TP_004004_20220401_20220411_02_T2	ice_conc_svalbard_202204011500.nc	1599
	East_Greenland_Sea	LC08_L1TP_226010_20220404_20220412_02_T1	ice_conc_svalbard_202204041500.nc	-2335
	East_Greenland_Sea	LC08_L1TP_224010_20220406_20220412_02_T1	ice_conc_svalbard_202204061500.nc	-3076
	East_Greenland_Sea	LC08_L1TP_231006_20220407_20220412_02_T1	ice_conc_svalbard_202204071500.nc	-575
	East_Greenland_Sea	LC08_L1TP_005004_20220408_20220412_02_T2	ice_conc_svalbard_202204081500.nc	1974
	East_Greenland_Sea	LC08_L1TP_001004_20220428_20220503_02_T2	ice_conc_svalbard_202204281500.nc	488
	East_Greenland_Sea	LC08_L1TP_004003_20220503_20220511_02_T2	ice_conc_svalbard_202205031500.nc	1580
	East_Greenland_Sea	LC08_L1TP_231007_20220509_20220518_02_T1	ice_conc_svalbard_202205091500.nc	-545
	East_Greenland_Sea	LC08_L1TP_005003_20220510_20220518_02_T2	ice_conc_svalbard_202205101500.nc	1956
	East_Greenland_Sea	LC08_L1TP_229006_20220511_20220519_02_T1	ice_conc_svalbard_202205111500.nc	-1310
	East_Greenland_Sea	LC08_L1TP_003005_20220512_20220519_02_T1	ice_conc_svalbard_202205121500.nc	1262
	East_Greenland_Sea	LC08_L1TP_227012_20220513_20220519_02_T1	ice_conc_svalbard_202205131500.nc	-1907
	East_Greenland_Sea	LC08_L1TP_230008_20220518_20220525_02_T1	ice_conc_svalbard_202205181500.nc	-889
	East_Greenland_Sea	LC08_L1TP_230009_20220603_20220610_02_T1	ice_conc_svalbard_202206031500.nc	-860
	East_Greenland_Sea	LC08_L1TP_226012_20220607_20220610_02_T1	ice_conc_svalbard_202206071500.nc	-2268
	East_Greenland_Sea	LC08_L1TP_007004_20220609_20220616_02_T1	ice_conc_svalbard_202206091500.nc	2734
	East_Greenland_Sea	LC08_L1TP_231007_20220610_20220616_02_T1	ice_conc_svalbard_202206101500.nc	-531
	East_Greenland_Sea	LC08_L1TP_008003_20220616_20220629_02_T1	ice_conc_svalbard_202206161500.nc	3086
	East_Greenland_Sea	LC08_L1TP_231006_20220712_20220722_02_T1	ice_conc_svalbard_202207121500.nc	-549
	East_Greenland_Sea	LC08_L1TP_229012_20220714_20220726_02_T1	ice_conc_svalbard_202207141500.nc	-1148
	East_Greenland_Sea	LC08_L1TP_003005_20220715_20220725_02_T1	ice_conc_svalbard_202207151500.nc	1281
	East_Greenland_Sea	LC08_L1TP_232005_20220804_20220818_02_T1	ice_conc_svalbard_202208041500.nc	-164
	East_Greenland_Sea	LC08_L1TP_229012_20220815_20220824_02_T1	ice_conc_svalbard_202208151500.nc	-1129
	East_Greenland_Sea	LC08_L1TP_227011_20220817_20220824_02_T1	ice_conc_svalbard_202208171500.nc	-1894
	East_Greenland_Sea	LC08_L1TP_004003_20220823_20220923_02_T1	ice_conc_svalbard_202208231500.nc	1623
	East_Greenland_Sea	LC08_L1TP_230008_20220907_20220914_02_T1	ice_conc_svalbard_202209071500.nc	-851
	Central_Arctic	LC08_L1TP_221244_20210430_20210508_02_T2	ice_conc_svalbard_202104301500.nc	1397
	Central_Arctic	LC08_L1TP_226243_20210503_20210508_02_T2	ice_conc_svalbard_202105031500.nc	3225
	Central_Arctic	LC08_L1TP_214243_20210811_20210811_02_T1	ice_conc_svalbard_202108031500.nc	-1191
	Central_Arctic	LC08_L1TP_224002_20220406_20220412_02_T1	ice_conc_svalbard_202204061500.nc	-3267
	Central_Arctic	LC08_L1TP_226001_20220420_20220427_02_T2	ice_conc_svalbard_202204201500.nc	-2546
	Central_Arctic	LC08_L1GT_229001_20220425_20220503_02_T2	ice_conc_svalbard_202204251500.nc	-1436
	Central_Arctic	LC08_L1TP_214245_20220518_20220525_02_T2	ice_conc_svalbard_202205181500.nc	-1151
	Central_Arctic	LC08_L1TP_225243_20220718_20220726_02_T1	ice_conc_svalbard_202207181500.nc	2899
	Kara_Sea	LC08_L1GT_222242_20210507_20210517_02_T2	ice_conc_svalbard_202105071500.nc	1717
	Kara_Sea	LC08_L1TP_214243_20210803_20210811_02_T1	ice_conc_svalbard_202108031500.nc	-1191
	Kara_Sea	LC08_L1TP_212245_20210805_20210811_02_T1	ice_conc_svalbard_202108051500.nc	-1956
	Kara_Sea	LC08_L1TP_209242_20220803_20220806_02_T1	ice_conc_svalbard_202208031500.nc	-3047
C2	East_Greenland_Sea	LC08_L1TP_228012_20210330_20210409_02_T1	ice_conc_svalbard_202103301500.nc	-1544
	East_Greenland_Sea	LC08_L1TP_229007_20210406_20210415_02_T1	ice_conc_svalbard_202104061500.nc	-1295
	East_Greenland_Sea	LC08_L1TP_227007_20220411_20220419_02_T1	ice_conc_svalbard_202204111500.nc	-2032
	East_Greenland_Sea	LC08_L1TP_228008_20220317_20220322_02_T1	ice_conc_svalbard_202203171500.nc	-1632
	East_Greenland_Sea	LC08_L1TP_229009_20220324_20220330_02_T1	ice_conc_svalbard_202203241500.nc	-1243
	East_Greenland_Sea	LC08_L1TP_225011_20220328_20220405_02_T2	ice_conc_svalbard_202203281500.nc	-2682
	East_Greenland_Sea	LC08_L1TP_230006_20220331_20220406_02_T2	ice_conc_svalbard_202203311500.nc	-949
	East_Greenland_Sea	LC08_L1TP_009003_20220404_20220412_02_T2	ice_conc_svalbard_202204041500.nc	3431
C3	Barents_Sea	LC08_L1TP_215245_20210607_20210615_02_T2	ice_conc_svalbard_202106071500.nc	-790
	East_Greenland_Sea	LC08_L1TP_227010_20210323_20210402_02_T1	ice_conc_svalbard_202103231500.nc	-1961
	East_Greenland_Sea	LC08_L1TP_227010_20210408_20210416_02_T1	ice_conc_svalbard_202104081500.nc	-1966
	East_Greenland_Sea	LC08_L1TP_223014_20210412_20210423_02_T1	ice_conc_svalbard_202104121500.nc	-3355
	East_Greenland_Sea	LC08_L1TP_230008_20210413_20210423_02_T1	ice_conc_svalbard_202104131500.nc	-903
	East_Greenland_Sea	LC08_L1TP_003004_20210423_20210501_02_T1	ice_conc_svalbard_202104231500.nc	1221
	East_Greenland_Sea	LC08_L1TP_225010_20210426_20210501_02_T2	ice_conc_svalbard_202104261500.nc	-2716
	East_Greenland_Sea	LC08_L1TP_006004_20210428_20210507_02_T1	ice_conc_svalbard_202104281500.nc	2331
	East_Greenland_Sea	LC08_L1TP_004004_20210430_20210508_02_T1	ice_conc_svalbard_202104301500.nc	1588
	East_Greenland_Sea	LC08_L1TP_001004_20210511_20210524_02_T1	ice_conc_svalbard_202105111500.nc	475
	East_Greenland_Sea	LC08_L1TP_225002_20210512_20210524_02_T1	ice_conc_svalbard_202105121500.nc	-2909
	East_Greenland_Sea	LC08_L1TP_009002_20210519_20210528_02_T1	ice_conc_svalbard_202105191500.nc	3399
	East_Greenland_Sea	LC08_L1TP_227008_20210526_20210529_02_T1	ice_conc_svalbard_202105261500.nc	-2016

	East_Greenland_Sea	LC08_L1TP_001005_20210527_20210607_02_T1	ice_conc_svalbard_202105271500.nc	509
	East_Greenland_Sea	LC08_L1TP_225011_20210528_20210607_02_T1	ice_conc_svalbard_202105281500.nc	-2685
	East_Greenland_Sea	LC08_L1TP_231008_20210607_20210615_02_T1	ice_conc_svalbard_202106071500.nc	-527
	East_Greenland_Sea	LC08_L1TP_003004_20210610_20210621_02_T1	ice_conc_svalbard_202106101500.nc	1233
	East_Greenland_Sea	LC08_L1TP_223014_20210615_20210622_02_T1	ice_conc_svalbard_202106151500.nc	-3347
	East_Greenland_Sea	LC08_L1TP_230007_20210616_20210622_02_T1	ice_conc_svalbard_202106161500.nc	-919
	East_Greenland_Sea	LC08_L1TP_228008_20210618_20210628_02_T1	ice_conc_svalbard_202106181500.nc	-1636
	East_Greenland_Sea	LC08_L1TP_233006_20210621_20210629_02_T1	ice_conc_svalbard_202106211500.nc	171
	East_Greenland_Sea	LC08_L1TP_007003_20210622_20210629_02_T1	ice_conc_svalbard_202106221500.nc	2696
	East_Greenland_Sea	LC08_L1TP_001005_20210628_20210707_02_T1	ice_conc_svalbard_202106281500.nc	520
	East_Greenland_Sea	LC08_L1TP_230007_20210702_20210708_02_T1	ice_conc_svalbard_202107021500.nc	-915
	East_Greenland_Sea	LC08_L1TP_226002_20210706_20210713_02_T2	ice_conc_svalbard_202107061500.nc	-2517
	East_Greenland_Sea	LC08_L1TP_001005_20210714_20210721_02_T1	ice_conc_svalbard_202107141500.nc	521
	East_Greenland_Sea	LC08_L1TP_002005_20210721_20210729_02_T1	ice_conc_svalbard_202107211500.nc	895
	East_Greenland_Sea	LC08_L1TP_229009_20210727_20210804_02_T1	ice_conc_svalbard_202107271500.nc	-1231
	East_Greenland_Sea	LC08_L1TP_227012_20210729_20210804_02_T1	ice_conc_svalbard_202107291500.nc	-1900
	East_Greenland_Sea	LC08_L1TP_006004_20210802_20210811_02_T1	ice_conc_svalbard_202108021500.nc	2361
	East_Greenland_Sea	LC08_L1TP_231008_20210810_20210819_02_T1	ice_conc_svalbard_202108101500.nc	-507
	East_Greenland_Sea	LC08_L1TP_229007_20210812_20210819_02_T1	ice_conc_svalbard_202108121500.nc	-1272
	East_Greenland_Sea	LC08_L1TP_232005_20210817_20210827_02_T1	ice_conc_svalbard_202108171500.nc	-206
	East_Greenland_Sea	LC08_L1TP_233005_20210824_20210901_02_T1	ice_conc_svalbard_202108241500.nc	167
	East_Greenland_Sea	LC08_L1TP_005003_20210827_20210901_02_T2	ice_conc_svalbard_202108271500.nc	1974
	East_Greenland_Sea	LC08_L1TP_001004_20210831_20210909_02_T1	ice_conc_svalbard_202108311500.nc	516
	East_Greenland_Sea	LC08_L1TP_227010_20220411_20220419_02_T1	ice_conc_svalbard_202204111500.nc	-1960
	East_Greenland_Sea	LC08_L1TP_001005_20220412_20220419_02_T1	ice_conc_svalbard_202204121500.nc	516
	East_Greenland_Sea	LC08_L1TP_233005_20220421_20220428_02_T1	ice_conc_svalbard_202204211500.nc	144
	East_Greenland_Sea	LC08_L1TP_229006_20220425_20220503_02_T2	ice_conc_svalbard_202204251500.nc	-1317
	East_Greenland_Sea	LC08_L1TP_227010_20211001_20211013_02_T1	ice_conc_svalbard_202110011500.nc	-1928
	East_Greenland_Sea	LC08_L1TP_232008_20220329_20220405_02_T1	ice_conc_svalbard_202203291500.nc	-159
	East_Greenland_Sea	LC08_L1TP_007003_20220406_20220412_02_T1	ice_conc_svalbard_202204061500.nc	2690
	East_Greenland_Sea	LC08_L1TP_227007_20220427_20220503_02_T2	ice_conc_svalbard_202204271500.nc	-2036
	East_Greenland_Sea	LC08_L1TP_001005_20220428_20220503_02_T1	ice_conc_svalbard_202204281500.nc	511
	East_Greenland_Sea	LC08_L1TP_230006_20220502_20220511_02_T1	ice_conc_svalbard_202205021500.nc	-945
	East_Greenland_Sea	LC08_L1TP_226009_20220506_20220512_02_T1	ice_conc_svalbard_202205061500.nc	-2353
	East_Greenland_Sea	LC08_L1TP_231006_20220509_20220518_02_T1	ice_conc_svalbard_202205091500.nc	-569
	East_Greenland_Sea	LC08_L1TP_229008_20220511_20220519_02_T1	ice_conc_svalbard_202205111500.nc	-1262
	East_Greenland_Sea	LC08_L1TP_232008_20220516_20220524_02_T1	ice_conc_svalbard_202205161500.nc	-148
	East_Greenland_Sea	LC08_L1TP_230007_20220603_20220610_02_T1	ice_conc_svalbard_202206031500.nc	-907
	East_Greenland_Sea	LC08_L1TP_226011_20220607_20220610_02_T1	ice_conc_svalbard_202206071500.nc	-2292
	East_Greenland_Sea	LC08_L1TP_001005_20220701_20220707_02_T1	ice_conc_svalbard_202207011500.nc	541
	East_Greenland_Sea	LC08_L1TP_228001_20220707_20220721_02_T1	ice_conc_svalbard_202207071500.nc	-1779
	East_Greenland_Sea	LC08_L1TP_231008_20220712_20220722_02_T1	ice_conc_svalbard_202207121500.nc	-501
	East_Greenland_Sea	LC08_L1TP_225002_20220718_20220726_02_T1	ice_conc_svalbard_202207181500.nc	-2867
	East_Greenland_Sea	LC08_L1TP_008003_20220803_20220817_02_T1	ice_conc_svalbard_202208031500.nc	3101
	East_Greenland_Sea	LC08_L1TP_009002_20220826_20220909_02_T1	ice_conc_svalbard_202208261500.nc	3454
	East_Greenland_Sea	LC08_L1TP_227009_20220902_20220910_02_T1	ice_conc_svalbard_202209021500.nc	-1942
	East_Greenland_Sea	LC08_L1TP_232006_20220905_20220914_02_T1	ice_conc_svalbard_202209051500.nc	-158
	Central_Arctic	LC08_L1TP_225002_20210512_20210524_02_T1	ice_conc_svalbard_202105121500.nc	-2909
	Central_Arctic	LC08_L1TP_215245_20210607_20210615_02_T2	ice_conc_svalbard_202106071500.nc	-790
	Central_Arctic	LC08_L1TP_226002_20210706_20210713_02_T2	ice_conc_svalbard_202107061500.nc	-2517
	Central_Arctic	LC08_L1GT_216245_20220601_20220609_02_T2	ice_conc_svalbard_202206011500.nc	-406
	Central_Arctic	LC08_L1TP_228001_20220707_20220721_02_T1	ice_conc_svalbard_202207071500.nc	-1779
	Central_Arctic	LC08_L1TP_225002_20220718_20220726_02_T1	ice_conc_svalbard_202207181500.nc	-2867
	Central_Arctic	LC08_L1TP_209243_20220803_20220806_02_T1	ice_conc_svalbard_202208031500.nc	-3023
	Kara_Sea	LC08_L1GT_225238_20210629_20210708_02_T2	ice_conc_svalbard_202106291500.nc	2758
	Kara_Sea	LC08_L1TP_209243_20220803_20220806_02_T1	ice_conc_svalbard_202208031500.nc	-3023
	East_Greenland_Sea	LC08_L1TP_228010_20210330_20210409_02_T1	ice_conc_svalbard_202103301500.nc	-1592
	East_Greenland_Sea	LC08_L1TP_003004_20210407_20210415_02_T1	ice_conc_svalbard_202104071500.nc	1229
	East_Greenland_Sea	LC08_L1TP_227012_20210408_20210416_02_T1	ice_conc_svalbard_202104081500.nc	-1918
C4	East_Greenland_Sea	LC08_L1TP_001005_20210409_20210416_02_T1	ice_conc_svalbard_202104091500.nc	510
	East_Greenland_Sea	LC08_L1TP_229010_20210422_20210430_02_T1	ice_conc_svalbard_202104221500.nc	-1230
	East_Greenland_Sea	LC08_L1TP_225011_20210426_20210501_02_T2	ice_conc_svalbard_202104261500.nc	-2692
	East_Greenland_Sea	LC08_L1TP_232006_20210427_20210501_02_T1	ice_conc_svalbard_202104271500.nc	-216

	East_Greenland_Sea	LC08_L1TP_006003_20210428_20210507_02_T1	ice_conc_svalbard_202104281500.nc	2307
	East_Greenland_Sea	LC08_L1TP_001005_20210511_20210524_02_T1	ice_conc_svalbard_202105111500.nc	499
	East_Greenland_Sea	LC08_L1TP_008003_20210512_20210524_02_T1	ice_conc_svalbard_202105121500.nc	3048
	East_Greenland_Sea	LC08_L1TP_002005_20210518_20210528_02_T1	ice_conc_svalbard_202105181500.nc	874
	East_Greenland_Sea	LC08_L1TP_226010_20210519_20210528_02_T1	ice_conc_svalbard_202105191500.nc	-2343
	East_Greenland_Sea	LC08_L1TP_001004_20210527_20210607_02_T1	ice_conc_svalbard_202105271500.nc	485
	East_Greenland_Sea	LC08_L1TP_231008_20210623_20210630_02_T1	ice_conc_svalbard_202106231500.nc	-522
	East_Greenland_Sea	LC08_L1TP_231008_20210709_20210720_02_T1	ice_conc_svalbard_202107091500.nc	-520
	East_Greenland_Sea	LC08_L1TP_002004_20210721_20210729_02_T1	ice_conc_svalbard_202107211500.nc	872
	East_Greenland_Sea	LC08_L1TP_229012_20210727_20210804_02_T1	ice_conc_svalbard_202107271500.nc	-1159
	East_Greenland_Sea	LC08_L1TP_227011_20210729_20210804_02_T1	ice_conc_svalbard_202107291500.nc	-1924
	East_Greenland_Sea	LC08_L1TP_001005_20210730_20210804_02_T1	ice_conc_svalbard_202107301500.nc	529
	East_Greenland_Sea	LC08_L1TP_005004_20210811_20210819_02_T1	ice_conc_svalbard_202108111500.nc	1994
	East_Greenland_Sea	LC08_L1TP_232008_20210817_20210827_02_T1	ice_conc_svalbard_202108171500.nc	-134
	East_Greenland_Sea	LC08_L1TP_233006_20210824_20210901_02_T1	ice_conc_svalbard_202108241500.nc	190
	East_Greenland_Sea	LC08_L1TP_005004_20210827_20210901_02_T1	ice_conc_svalbard_202108271500.nc	1998
	East_Greenland_Sea	LC08_L1TP_232008_20210902_20210910_02_T1	ice_conc_svalbard_202109021500.nc	-130
	East_Greenland_Sea	LC08_L1TP_006004_20210903_20210910_02_T1	ice_conc_svalbard_202109031500.nc	2371
	East_Greenland_Sea	LC08_L1TP_227012_20220411_20220419_02_T1	ice_conc_svalbard_202204111500.nc	-1913
	East_Greenland_Sea	LC08_L1TP_229010_20220425_20220503_02_T1	ice_conc_svalbard_202204251500.nc	-1221
	East_Greenland_Sea	LC08_L1TP_003004_20220426_20220503_02_T1	ice_conc_svalbard_202204261500.nc	1231
	East_Greenland_Sea	LC08_L1TP_225010_20220328_20220405_02_T2	ice_conc_svalbard_202203281500.nc	-2706
	East_Greenland_Sea	LC08_L1TP_233006_20220405_20220412_02_T1	ice_conc_svalbard_202204051500.nc	166
	East_Greenland_Sea	LC08_L1TP_224011_20220406_20220412_02_T1	ice_conc_svalbard_202204061500.nc	-3052
	East_Greenland_Sea	LC08_L1TP_008003_20220429_20220504_02_T1	ice_conc_svalbard_202204291500.nc	3060
	East_Greenland_Sea	LC08_L1TP_230009_20220502_20220511_02_T1	ice_conc_svalbard_202205021500.nc	-873
	East_Greenland_Sea	LC08_L1TP_004004_20220503_20220511_02_T1	ice_conc_svalbard_202205031500.nc	1604
	East_Greenland_Sea	LC08_L1TP_002005_20220505_20220511_02_T1	ice_conc_svalbard_202205051500.nc	888
	East_Greenland_Sea	LC08_L1TP_226012_20220506_20220512_02_T1	ice_conc_svalbard_202205061500.nc	-2282
	East_Greenland_Sea	LC08_L1TP_231008_20220509_20220518_02_T1	ice_conc_svalbard_202205091500.nc	-521
	East_Greenland_Sea	LC08_L1TP_005004_20220510_20220518_02_T1	ice_conc_svalbard_202205101500.nc	1980
	East_Greenland_Sea	LC08_L1TP_229007_20220511_20220519_02_T1	ice_conc_svalbard_202205111500.nc	-1286
	East_Greenland_Sea	LC08_L1TP_003004_20220512_20220519_02_T1	ice_conc_svalbard_202205121500.nc	1239
	East_Greenland_Sea	LC08_L1TP_228010_20220824_20220924_02_T1	ice_conc_svalbard_202208241500.nc	-1547
	East_Greenland_Sea	LC08_L1TP_002005_20220825_20220924_02_T1	ice_conc_svalbard_202208251500.nc	929
	East_Greenland_Sea	LC08_L1TP_009003_20220826_20220909_02_T1	ice_conc_svalbard_202208261500.nc	3478
	East_Greenland_Sea	LC08_L1TP_227012_20220902_20220910_02_T1	ice_conc_svalbard_202209021500.nc	-1871
	East_Greenland_Sea	LC08_L1TP_230008_20220923_20220929_02_T1	ice_conc_svalbard_202209231500.nc	-846
	Central_Arctic	LC08_L1TP_225001_20220718_20220726_02_T1	ice_conc_svalbard_202207181500.nc	-2891

Table S3~~2~~: List of Landsat-8 scenes and ice charts used for evaluation. Time differences between the two data for each scene are also tabulated.

40 S4̶3̶ Melt Pond Fraction Data

Filename (Melt Pond Fraction)	Filename (Landsat-8)	Time Difference [sec[
20210719_T45XVK_s2_mpf.nc	LC08_L1TP_173002_20210719_20210729_02_T1	-1539
20200806_T31XDL_s2_mpf.nc	LC08_L1GT_023243_20200806_20200916_02_T2	7268
20200806_T31XDL_s2_mpf.nc	LC08_L1TP_023244_20200806_20200916_02_T1	7292
20200711_T13XEL_s2_mpf.nc	LC08_L1TP_065001_20200711_20200912_02_T1	-5904
20210719_T14XMQ_s2_mpf.nc	LC08_L1TP_068001_20210719_20210729_02_T1	-2378
20200711_T13XEL_s2_mpf.nc	LC08_L1TP_081244_20200711_20200912_02_T1	5842

Table S4̶3̶: List of Landsat-8 scenes and melt pond fraction datasets used for evaluation. Time differences between the two data for each scene are also tabulated.

45 S5̶4̶ Sensitivity Test and Uncertainty Analysis

Region	Filename	
	C1	C2
	LC08_L1TP_058245_20200507_20200820_02_T1	LC08_L1TP_010020_20220222_20220301_02_T2
	LC08_L1TP_061244_20210429_20210508_02_T1	LC08_L1TP_014013_20200316_20200822_02_T1
	LC08_L1TP_044002_20210406_20210415_02_T1	LC08_L1TP_011010_20220317_20220322_02_T1
	LC08_L1TP_035248_20200826_20200905_02_T1	LC08_L1TP_029005_20210328_20210402_02_T1
	LC08_L1TP_039002_20210419_20210430_02_T1	LC08_L1TP_019013_20220426_20220503_02_T2
	LC08_L1TP_037002_20220830_20220910_02_T1	LC08_L1TP_056245_20220531_20220609_02_T1
	LC08_L1TP_081240_20200609_20200824_02_T1	LC08_L1TP_030008_20220322_20220330_02_T2
	LC08_L1TP_016015_20220405_20220412_02_T1	LC08_L1TP_014009_20200401_20200822_02_T1
	LC08_L1TP_022011_20220922_20220929_02_T1	LC08_L1TP_038003_20200511_20200820_02_T1
	LC08_L1TP_011012_20220317_20220322_02_T1	LC08_L1TP_036005_20200411_20200822_02_T1
Baffin Bay	C3	C4
	LC08_L1TP_038247_20210514_20210525_02_T1	LC08_L1TP_017016_20200812_20200918_02_T1
	LC08_L1TP_033005_20220514_20220519_02_T1	LC08_L1TP_018008_20210502_20210508_02_T1
	LC08_L1TP_051246_20220629_20220707_02_T1	LC08_L1TP_010011_20220801_20220805_02_T1
	LC08_L1TP_038002_20200425_20200822_02_T1	LC08_L1TP_067242_20220629_20220707_02_T1
	LC08_L1TP_034003_20210502_20210508_02_T1	LC08_L1TP_030248_20220626_20220706_02_T1
	LC08_L1TP_040247_20220616_20220629_02_T1	LC08_L1TP_034003_20210822_20210827_02_T1
	LC08_L1TP_078241_20200722_20200911_02_T1	LC08_L1TP_018008_20220318_20220322_02_T1
	LC08_L1TP_060244_20210625_20210707_02_T1	LC08_L1TP_029005_20220705_20220722_02_T1
	LC08_L1TP_004026_20210921_20210930_02_T1	LC08_L1TP_013009_20220619_20220630_02_T1
	LC08_L1TP_018016_20220926_20221004_02_T1	LC08_L1TP_051246_20200623_20200823_02_T1

	C1	C2
	LC08_L1TP_197001_20220425_20220503_02_T2	LC08_L1TP_013242_20220518_20220525_02_T2
	LC08_L1TP_214002_20200731_20200908_02_T1	LC08_L1TP_184015_20210222_20210303_02_T1
	LC08_L1GT_194002_20220420_20220427_02_T2	LC08_L1TP_222001_20220424_20220503_02_T2
	LC08_L1GT_027238_20210602_20210608_02_T2	LC08_L1TP_177006_20220328_20220405_02_T2
	LC08_L1TP_172010_20210322_20210401_02_T1	LC08_L1GT_204246_20220426_20220503_02_T2
	LC08_L1TP_180008_20220605_20220610_02_T1	LC08_L1TP_171012_20210315_20210328_02_T1
	LC08_L1TP_186013_20210409_20210416_02_T1	LC08_L1TP_210002_20210503_20210508_02_T2
	LC08_L1TP_179006_20210915_20210924_02_T1	LC08_L1TP_203245_20210502_20210508_02_T1
	LC08_L1TP_008242_20220718_20220725_02_T1	LC08_L1TP_176011_20210318_20210328_02_T1
Barents Sea	LC08_L1TP_169012_20220304_20220314_02_T1	LC08_L1TP_169011_20210317_20210328_02_T2
	C3	C4
	LC08_L1TP_183014_20220712_20220722_02_T1	LC08_L1TP_184012_20200526_20200820_02_T1
	LC08_L1TP_177013_20220531_20220609_02_T1	LC08_L1TP_185015_20200330_20200822_02_T1
	LC08_L1TP_023239_20210606_20210615_02_T1	LC08_L1TP_186014_20200321_20200822_02_T1
	LC08_L1TP_205002_20200817_20200920_02_T2	LC08_L1TP_176011_20200721_20200911_02_T1
	LC08_L1TP_023240_20200619_20200824_02_T1	LC08_L1TP_178008_20220607_20220610_02_T1
	LC08_L1TP_169012_20210925_20211001_02_T1	LC08_L1TP_185014_20210605_20210614_02_T1
	LC08_L1TP_172012_20210626_20210707_02_T1	LC08_L1TP_184015_20211004_20211013_02_T1
	LC08_L1TP_174011_20220408_20220412_02_T1	LC08_L1TP_184012_20220703_20220708_02_T1
	LC08_L1TP_208003_20200619_20200823_02_T1	LC08_L1TP_174011_20200723_20200911_02_T1
	LC08_L1TP_026240_20220529_20220603_02_T2	LC08_L1TP_178014_20200719_20200911_02_T1
	C1	C2
	LC08_L1TP_060010_20210625_20210707_02_T1	LC08_L1TP_071011_20210403_20210409_02_T1
	LC08_L1GT_065010_20220717_20220725_02_T2	LC08_L1TP_059011_20210330_20210409_02_T1
	LC08_L1TP_063006_20210326_20210402_02_T1	LC08_L1TP_065006_20220327_20220405_02_T2
	LC08_L1GT_071008_20220524_20220602_02_T2	LC08_L1TP_071010_20210403_20210409_02_T2
	LC08_L1TP_072010_20200610_20200823_02_T1	LC08_L1TP_078010_20220322_20220330_02_T2
	LC08_L1TP_071010_20220406_20220412_02_T2	LC08_L1TP_075010_20200311_20200822_02_T2
	LC08_L1TP_061011_20220416_20220420_02_T1	LC08_L1TP_065006_20210409_20210416_02_T2
	LC08_L1TP_059009_20210415_20210424_02_T1	LC08_L1TP_079010_20210411_20210416_02_T2
	LC08_L1TP_061008_20220721_20220801_02_T1	LC08_L1TP_077010_20210328_20210402_02_T1
Beaufort Sea	LC08_L1TP_072011_20210410_20210416_02_T1	LC08_L1TP_075011_20210314_20210328_02_T1
	C3	C4
	LC08_L1TP_080010_20200704_20200913_02_T1	LC08_L1TP_060010_20220324_20220330_02_T1
	LC08_L1GT_073006_20220506_20220512_02_T2	LC08_L1TP_065012_20220327_20220405_02_T1
	LC08_L1TP_063011_20210513_20210524_02_T2	LC08_L1TP_073011_20200430_20200820_02_T1
	LC08_L1TP_079010_20200510_20200820_02_T1	LC08_L1GT_071010_20220422_20220428_02_T2
	LC08_L1TP_063011_20210614_20210622_02_T1	LC08_L1GT_072010_20220312_20220321_02_T2
	LC08_L1TP_064006_20220507_20220512_02_T2	LC08_L1TP_063011_20200611_20200824_02_T1
	LC08_L1TP_070011_20220330_20220406_02_T1	LC08_L1TP_079010_20210326_20210402_02_T1
	LC08_L1TP_064011_20210418_20210424_02_T1	LC08_L1TP_075011_20210720_20210729_02_T1

	LC08_L1TP_061011_20200731_20200908_02_T1	LC08_L1TP_072011_20210715_20210721_02_T1
	LC08_L1TP_065006_20210425_20210501_02_T2	LC08_L1TP_062008_20220423_20220428_02_T2
	C1	**C2**
	LC08_L1TP_090014_20200304_20200822_02_T2	LC08_L1TP_090015_20210408_20210416_02_T2
	LC08_L1GT_090015_20200405_20200822_02_T2	LC08_L1TP_082016_20200225_20200822_02_T2
	LC08_L1TP_080015_20221014_20221021_02_T1	LC08_L1TP_086013_20210311_20210317_02_T2
	LC08_L1TP_084014_20200310_20200822_02_T1	LC08_L1GT_082017_20200225_20200822_02_T2
	LC08_L1TP_095021_20200627_20200823_02_T1	LC08_L1TP_082014_20200328_20200822_02_T1
	LC08_L1TP_094017_20210319_20210328_02_T1	LC08_L1TP_086013_20210327_20210402_02_T2
	LC08_L1TP_079016_20200408_20200822_02_T1	LC08_L1TP_087014_20210318_20210328_02_T2
	LC08_L1TP_073020_20200210_20200823_02_T1	LC08_L1TP_079018_20210310_20210317_02_T2
	LC08_L1TP_084016_20210225_20210304_02_T2	LC08_L1TP_082015_20200328_20200822_02_T2
	LC08_L1TP_077023_20220126_20220204_02_T1	LC08_L1TP_075018_20200224_20200822_02_T2
Bering Sea	**C3**	**C4**
	LC08_L1TP_096018_20220524_20220602_02_T1	LC08_L1TP_099019_20200304_20200822_02_T1
	LC08_L1TP_089016_20200617_20200823_02_T1	LC08_L1TP_092013_20220425_20220503_02_T1
	LC08_L1TP_079014_20220430_20220504_02_T1	LC08_L1TP_082016_20220419_20220427_02_T1
	LC08_L1TP_090015_20200608_20200824_02_T1	LC08_L1TP_090014_20210526_20210607_02_T1
	LC08_L1TP_098021_20220826_20220924_02_T1	LC08_L1TP_098020_20210417_20210424_02_T1
	LC08_L1TP_083024_20211203_20211209_02_T1	LC08_L1TP_096017_20200228_20200822_02_T1
	LC08_L1TP_086013_20220602_20220610_02_T1	LC08_L1TP_096017_20211028_20211104_02_T1
	LC08_L1TP_099019_20200928_20201006_02_T1	LC08_L1TP_092015_20210711_20210720_02_T1
	LC08_L1TP_073019_20210924_20210930_02_T1	LC08_L1TP_095018_20220601_20220609_02_T1
	LC08_L1TP_078017_20200519_20200820_02_T1	LC08_L1TP_078016_20210420_20210430_02_T1
	C1	**C2**
	LC08_L1TP_046013_20200417_20200822_02_T2	LC08_L1TP_036010_20210329_20210409_02_T2
	LC08_L1TP_106240_20220615_20220627_02_T1	LC08_L1TP_055247_20220422_20220428_02_T1
	LC08_L1TP_061001_20210515_20210525_02_T1	LC08_L1TP_050008_20210331_20210409_02_T2
	LC08_L1TP_060247_20210422_20210430_02_T1	LC08_L1TP_049007_20220327_20220405_02_T2
	LC08_L1TP_060004_20210508_20210518_02_T1	LC08_L1TP_032012_20210317_20210328_02_T1
	LC08_L1TP_062001_20220525_20220602_02_T1	LC08_L1TP_059009_20210330_20210409_02_T2
	LC08_L1TP_053009_20210320_20210401_02_T2	LC08_L1TP_052011_20210329_20210409_02_T1
Canadian	LC08_L1TP_033009_20200321_20200822_02_T1	LC08_L1TP_061006_20200325_20200822_02_T1
Archipelago	LC08_L1TP_056011_20210410_20210416_02_T1	LC08_L1TP_049006_20220327_20220405_02_T2
	LC08_L1TP_106238_20200609_20200824_02_T1	LC08_L1TP_041009_20220420_20220428_02_T2
	C3	**C4**
	LC08_L1TP_037009_20220408_20220412_02_T1	LC08_L1TP_065006_20210425_20210501_02_T2
	LC08_L1TP_043011_20210922_20210930_02_T1	LC08_L1TP_057006_20210503_20210508_02_T1
	LC08_L1TP_062001_20220626_20220706_02_T1	LC08_L1TP_080243_20220726_20220802_02_T1
	LC08_L1TP_041011_20200313_20200822_02_T2	LC08_L1TP_059004_20210618_20210628_02_T1
	LC08_L1TP_060007_20210828_20210901_02_T1	LC08_L1TP_047013_20220329_20220406_02_T1
	LC08_L1TP_041012_20220420_20220428_02_T2	LC08_L1TP_058247_20210424_20210501_02_T1

	LC08_L1TP_042012_20210611_20210622_02_T1	LC08_L1TP_035008_20200725_20200908_02_T1
	LC08_L1TP_039012_20210708_20210713_02_T1	LC08_L1TP_060001_20220511_20220519_02_T1
	LC08_L1TP_060004_20200809_20200917_02_T1	LC08_L1TP_055002_20200502_20200820_02_T1
	LC08_L1TP_047011_20210630_20210708_02_T1	LC08_L1TP_055010_20220711_20220722_02_T1
	C1	**C2**
	LC08_L1TP_085243_20220714_20220722_02_T1	LC08_L1TP_023244_20210505_20210517_02_T2
	LC08_L1TP_056248_20220413_20220420_02_T1	LC08_L1TP_065003_20220412_20220419_02_T2
	LC08_L1TP_060004_20200419_20200822_02_T1	LC08_L1TP_065005_20220327_20220405_02_T1
	LC08_L1TP_039244_20220524_20220602_02_T1	LC08_L1TP_065005_20210409_20210416_02_T2
	LC08_L1TP_022245_20210514_20210525_02_T1	LC08_L1TP_062005_20220407_20220412_02_T1
	LC08_L1TP_227001_20200726_20200908_02_T1	LC08_L1TP_064006_20220421_20220428_02_T2
	LC08_L1TP_198242_20200512_20200820_02_T1	LC08_L1GT_192246_20200502_20201016_02_T2
	LC08_L1TP_042245_20220427_20220503_02_T1	LC08_L1TP_124006_20210407_20210415_02_T1
	LC08_L1TP_219002_20210822_20210827_02_T1	LC08_L1TP_065002_20220412_20220419_02_T2
Central Arctic	LC08_L1TP_074245_20220614_20220627_02_T1	LC08_L1TP_029247_20220416_20220420_02_T1
	C3	**C4**
	LC08_L1TP_031244_20220617_20220629_02_T1	LC08_L1TP_030245_20210623_20210630_02_T1
	LC08_L1TP_006247_20220821_20220923_02_T1	LC08_L1TP_048248_20200415_20200822_02_T1
	LC08_L1TP_063006_20220617_20220629_02_T1	LC08_L1TP_035247_20220512_20220519_02_T1
	LC08_L1TP_052245_20210617_20210628_02_T1	LC08_L1GT_073005_20220506_20220512_02_T2
	LC08_L1TP_012248_20220714_20220725_02_T1	LC08_L1TP_033244_20220530_20220609_02_T1
	LC08_L1TP_063004_20200627_20200823_02_T1	LC08_L1TP_049246_20210527_20210607_02_T1
	LC08_L1TP_015247_20210513_20210524_02_T1	LC08_L1GT_182247_20220721_20220726_02_T2
	LC08_L1TP_032245_20220523_20220602_02_T1	LC08_L1TP_074244_20220801_20220805_02_T1
	LC08_L1TP_217002_20210808_20210819_02_T1	LC08_L1TP_013247_20200629_20200823_02_T1
	LC08_L1TP_066001_20220825_20220924_02_T1	LC08_L1TP_059004_20210415_20210424_02_T1
	C1	**C2**
	LC08_L1TP_087013_20210318_20210328_02_T2	LC08_L1TP_082013_20200328_20200822_02_T1
	LC08_L1TP_079013_20220703_20220707_02_T1	LC08_L1TP_095011_20210310_20210317_02_T2
	LC08_L1TP_091012_20200412_20200822_02_T2	LC08_L1TP_086014_20210327_20210402_02_T1
	LC08_L1TP_081011_20200508_20200820_02_T2	LC08_L1TP_091012_20220402_20220412_02_T1
	LC08_L1GT_092010_20220409_20220419_02_T2	LC08_L1TP_084013_20220401_20220411_02_T2
	LC08_L1TP_086014_20200409_20200822_02_T1	LC08_L1TP_086013_20210327_20210402_02_T2
Chukchi Sea	LC08_L1TP_090013_20220801_20220805_02_T1	LC08_L1TP_079014_20200408_20200822_02_T1
	LC08_L1TP_090012_20220326_20220330_02_T2	LC08_L1TP_086013_20210311_20210317_02_T2
	LC08_L1TP_094011_20200417_20200825_02_T2	LC08_L1TP_091012_20200327_20200822_02_T2
	LC08_L1TP_080011_20210317_20210328_02_T1	LC08_L1TP_095010_20210310_20210317_02_T2
	C3	**C4**
	LC08_L1TP_083010_20200709_20210330_02_T1	LC08_L1TP_083014_20200607_20200824_02_T1
	LC08_L1TP_079014_20200814_20200920_02_T1	LC08_L1TP_080014_20200330_20200822_02_T1
	LC08_L1TP_084013_20200614_20200823_02_T1	LC08_L1TP_080011_20220320_20220329_02_T2
	LC08_L1TP_082013_20200515_20200820_02_T1	LC08_L1TP_079013_20220313_20220322_02_T1

	LC08_L1TP_096010_20220523_20220602_02_T1	LC08_L1TP_081012_20220311_20220321_02_T1
	LC08_L1TP_092012_20210422_20210430_02_T2	LC08_L1TP_088013_20220312_20220321_02_T2
	LC08_L1TP_088013_20220803_20220818_02_T1	LC08_L1TP_092011_20220425_20220503_02_T2
	LC08_L1TP_086014_20220602_20220610_02_T1	LC08_L1TP_087013_20220422_20220428_02_T2
	LC08_L1TP_083012_20210525_20210529_02_T1	LC08_L1TP_081011_20210425_20210501_02_T1
	LC08_L1TP_081013_20200711_20200912_02_T1	LC08_L1TP_079010_20220414_20220420_02_T2

	C1	C2
	LC08_L1TP_227011_20210915_20210925_02_T1	LC08_L1TP_229009_20220324_20220330_02_T1
	LC08_L1TP_232016_20200323_20200822_02_T1	LC08_L1TP_230008_20200325_20200822_02_T1
	LC08_L1TP_052240_20210601_20210608_02_T1	LC08_L1TP_009003_20220404_20220412_02_T1
	LC08_L1TP_019245_20200725_20200908_02_T1	LC08_L1TP_228008_20220317_20220322_02_T1
	LC08_L1TP_229013_20220730_20220806_02_T1	LC08_L1TP_228008_20200412_20200822_02_T1
	LC08_L1TP_026244_20210627_20210707_02_T1	LC08_L1TP_010003_20210408_20210416_02_T1
	LC08_L1TP_233006_20210418_20210424_02_T1	LC08_L1TP_024245_20220429_20220504_02_T1
	LC08_L1TP_216003_20200424_20200822_02_T1	LC08_L1TP_228012_20210330_20210409_02_T1
	LC08_L1TP_229010_20210508_20210518_02_T1	LC08_L1TP_230006_20220331_20220406_02_T2
East Greenland	LC08_L1TP_230006_20200528_20200820_02_T1	LC08_L1TP_231007_20200401_20200822_02_T1
Sea	C3	C4
	LC08_L1TP_227008_20200827_20200906_02_T1	LC08_L1TP_220014_20220528_20220603_02_T1
	LC08_L1TP_001005_20210527_20210607_02_T1	LC08_L1TP_002005_20220505_20220511_02_T1
	LC08_L1TP_228001_20220707_20220721_02_T1	LC08_L1TP_012002_20210406_20210415_02_T1
	LC08_L1GT_229001_20210711_20210720_02_T2	LC08_L1TP_006003_20220501_20220511_02_T1
	LC08_L1TP_001004_20210831_20210909_02_T1	LC08_L1TP_037242_20200621_20200823_02_T1
	LC08_L1TP_035243_20220512_20220519_02_T1	LC08_L1TP_229008_20210422_20210430_02_T1
	LC08_L1TP_228007_20200428_20200820_02_T1	LC08_L1TP_231006_20220423_20220428_02_T1
	LC08_L1TP_218013_20210527_20210607_02_T1	LC08_L1TP_037243_20210523_20210529_02_T1
	LC08_L1TP_045241_20210616_20210622_02_T1	LC08_L1TP_233017_20200922_20201005_02_T1
	LC08_L1TP_024244_20210512_20210524_02_T1	LC08_L1TP_045241_20200629_20200824_02_T1

	C1	C2
	LC08_L1TP_121009_20210317_20210328_02_T2	LC08_L1TP_108011_20210322_20210401_02_T1
	LC08_L1TP_108010_20200319_20200822_02_T2	LC08_L1TP_099012_20220411_20220419_02_T1
	LC08_L1TP_121009_20200330_20200822_02_T1	LC08_L1TP_095011_20210326_20210402_02_T2
	LC08_L1TP_099012_20220310_20220315_02_T2	LC08_L1TP_125006_20210414_20210423_02_T2
	LC08_L1TP_122007_20220412_20220419_02_T1	LC08_L1TP_099011_20210323_20210402_02_T1
East Siberian Sea	LC08_L1TP_100012_20210501_20210508_02_T1	LC08_L1TP_125007_20200326_20200822_02_T1
	LC08_L1TP_100011_20200311_20200822_02_T2	LC08_L1TP_128006_20210403_20210409_02_T2
	LC08_L1TP_178238_20210620_20210629_02_T1	LC08_L1TP_113010_20200322_20200822_02_T2
	LC08_L1TP_094011_20210319_20210328_02_T2	LC08_L1TP_099012_20210307_20210317_02_T2
	LC08_L1TP_100011_20210330_20210409_02_T2	LC08_L1TP_099011_20210408_20210416_02_T2
	C3	C4
	LC08_L1TP_103011_20220407_20220412_02_T1	LC08_L1TP_111010_20220330_20220406_02_T1
	LC08_L1TP_108010_20210626_20210707_02_T1	LC08_L1TP_106011_20210527_20210607_02_T1

	LC08_L1GT_176239_20220609_20220616_02_T2	LC08_L1TP_093011_20220315_20220322_02_T2
	LC08_L1TP_115010_20200405_20200822_02_T2	LC08_L1GT_170239_20200711_20200912_02_T2
	LC08_L1TP_102011_20220502_20220511_02_T2	LC08_L1TP_119009_20200620_20200823_02_T1
	LC08_L1TP_099011_20220817_20220824_02_T1	LC08_L1TP_096011_20220320_20220329_02_T1
	LC08_L1TP_096010_20220608_20220616_02_T1	LC08_L1TP_109010_20210516_20210525_02_T1
	LC08_L1GT_121008_20200517_20200820_02_T2	LC08_L1TP_097011_20200509_20200820_02_T2
	LC08_L1TP_119008_20220407_20220412_02_T2	LC08_L1TP_098011_20220404_20220412_02_T1
	LC08_L1TP_105011_20210707_20210713_02_T1	LC08_L1TP_108010_20210525_20210529_02_T1

	C1	C2
	LC08_L1TP_025017_20210417_20210424_02_T2	LC08_L1TP_023018_20210318_20210328_02_T2
	LC08_L1TP_030010_20200417_20200822_02_T1	LC08_L1TP_020021_20220316_20220322_02_T1
	LC08_L1TP_028010_20220511_20220519_02_T1	LC08_L1TP_019016_20200404_20200822_02_T1
	LC08_L1TP_028011_20210929_20211012_02_T1	LC08_L1TP_027014_20210330_20210409_02_T1
	LC08_L1TP_028010_20200505_20200820_02_T1	LC08_L1TP_022021_20200308_20200822_02_T1
	LC08_L1TP_021020_20220627_20220706_02_T1	LC08_L1TP_032018_20200314_20200822_02_T2
	LC08_L1TP_029020_20210328_20210402_02_T1	LC08_L1TP_015018_20210326_20210402_02_T2
	LC08_L1TP_017017_20210324_20210402_02_T2	LC08_L1TP_029015_20200309_20200822_02_T2
	LC08_L1TP_024012_20200423_20200822_02_T1	LC08_L1TP_023012_20200331_20200822_02_T2
Hudson Bay	LC08_L1TP_032016_20220320_20220329_02_T1	LC08_L1TP_026011_20200421_20200822_02_T1

	C3	C4
	LC08_L1TP_021023_20220713_20220722_02_T1	LC08_L1TP_030016_20220407_20220412_02_T2
	LC08_L1TP_033019_20220818_20220823_02_T1	LC08_L1TP_020023_20220924_20221004_02_T1
	LC08_L1TP_028011_20210406_20210415_02_T2	LC08_L1TP_032018_20210317_20210328_02_T1
	LC08_L1TP_024014_20210715_20210721_02_T1	LC08_L1TP_026016_20200405_20200822_02_T2
	LC08_L1TP_023016_20210318_20210328_02_T1	LC08_L1TP_027016_20200701_20200913_02_T1
	LC08_L1TP_024016_20210901_20210909_02_T1	LC08_L1TP_019024_20210712_20210720_02_T1
	LC08_L1TP_025012_20210924_20210930_02_T1	LC08_L1TP_029013_20220619_20220630_02_T1
	LC08_L1TP_019020_20220426_20220503_02_T2	LC08_L1TP_019020_20220325_20220330_02_T1
	LC08_L1TP_022021_20220906_20220914_02_T1	LC08_L1TP_019016_20220715_20220725_02_T1
	LC08_L1GT_026014_20220513_20220519_02_T2	LC08_L1TP_026021_20221004_20221012_02_T1

	C1	C2
	LC08_L1TP_160010_20220422_20220428_02_T2	LC08_L1TP_160008_20210403_20210409_02_T2
	LC08_L1TP_177006_20220328_20220405_02_T2	LC08_L1TP_161013_20200306_20200822_02_T2
	LC08_L1TP_205245_20210430_20210508_02_T1	LC08_L1GT_160003_20210403_20210409_02_T2
	LC08_L1TP_165012_20200403_20200822_02_T1	LC08_L1TP_164008_20210330_20210409_02_T2
Kara Sea	LC08_L1TP_163008_20210323_20210402_02_T2	LC08_L1GT_158003_20220510_20220518_02_T2
	LC08_L1TP_162003_20200414_20200822_02_T2	LC08_L1TP_169011_20210317_20210328_02_T2
	LC08_L1TP_168008_20200408_20200822_02_T1	LC08_L1TP_167003_20210404_20210409_02_T2
	LC08_L1TP_160009_20220406_20220412_02_T2	LC08_L1GT_192246_20200502_20201016_02_T2
	LC08_L1GT_210241_20200703_20200913_02_T2	LC08_L1TP_165007_20210321_20210401_02_T2
	LC08_L1TP_164009_20220402_20220411_02_T1	LC08_L1TP_160009_20200416_20200822_02_T2

	C3	C4

LC08_L1TP_167010_20210810_20210819_02_T1	LC08_L1TP_172011_20220613_20220617_02_T1
LC08_L1TP_151005_20220509_20220518_02_T1	LC08_L1TP_164002_20200412_20200822_02_T2
LC08_L1TP_166009_20210328_20210402_02_T1	LC08_L1TP_164007_20210330_20210409_02_T1
LC08_L1TP_158008_20220627_20220706_02_T1	LC08_L1TP_185248_20220421_20220428_02_T1
LC08_L1TP_201242_20200704_20200913_02_T1	LC08_L1TP_182246_20220721_20220726_02_T1
LC08_L1TP_172010_20210712_20210720_02_T1	LC08_L1TP_164010_20200514_20200820_02_T1
LC08_L1TP_161008_20210629_20210708_02_T1	LC08_L1TP_158007_20220611_20220617_02_T1
LC08_L1TP_175010_20220602_20220609_02_T1	LC08_L1TP_168010_20210614_20210622_02_T1
LC08_L1TP_160005_20200705_20200913_02_T1	LC08_L1TP_172011_20220731_20220806_02_T1
LC08_L1TP_179006_20220716_20220726_02_T1	LC08_L1TP_158009_20200504_20200820_02_T2

	C1	C2
	LC08_L1TP_155005_20220419_20220427_02_T1	LC08_L1TP_121008_20220320_20220329_02_T1
	LC08_L1TP_147006_20210323_20210402_02_T1	LC08_L1TP_124007_20200404_20200822_02_T1
	LC08_L1TP_144006_20200416_20200822_02_T1	LC08_L1TP_128006_20210403_20210409_02_T2
	LC08_L1TP_125010_20200310_20200822_02_T2	LC08_L1TP_130008_20210401_20210409_02_T2
	LC08_L1TP_132009_20220317_20220322_02_T1	LC08_L1TP_150005_20220416_20220420_02_T1
	LC08_L1GT_149005_20210406_20210415_02_T2	LC08_L1TP_129006_20210325_20210402_02_T2
	LC08_L1TP_139008_20220318_20220322_02_T2	LC08_L1TP_174001_20220424_20220428_02_T2
	LC08_L1TP_144007_20220321_20220329_02_T1	LC08_L1TP_151005_20200417_20200822_02_T2
	LC08_L1TP_127006_20210428_20210507_02_T2	LC08_L1TP_129010_20210410_20210416_02_T1
	LC08_L1TP_150006_20220416_20220420_02_T1	LC08_L1TP_155004_20210331_20210409_02_T2
Laptev Sea	C3	C4
	LC08_L1TP_133009_20220425_20220503_02_T1	LC08_L1TP_129010_20220515_20220519_02_T1
	LC08_L1TP_131008_20210713_20210721_02_T1	LC08_L1TP_123009_20220318_20220322_02_T1
	LC08_L1TP_126010_20200621_20200823_02_T1	LC08_L1TP_122008_20210527_20210607_02_T1
	LC08_L1TP_150006_20200731_20200908_02_T1	LC08_L1TP_139008_20210331_20210409_02_T1
	LC08_L1TP_166002_20220502_20220511_02_T2	LC08_L1TP_130008_20200617_20200823_02_T1
	LC08_L1GT_158003_20220510_20220518_02_T2	LC08_L1TP_146007_20210401_20210409_02_T1
	LC08_L1TP_121010_20220405_20220412_02_T2	LC08_L1TP_126008_20220611_20220617_02_T1
	LC08_L1TP_130009_20210417_20210424_02_T2	LC08_L1TP_124009_20200911_20200919_02_T1
	LC08_L1TP_124009_20220410_20220419_02_T2	LC08_L1TP_124010_20220410_20220419_02_T1
	LC08_L1TP_152005_20220804_20220818_02_T1	LC08_L1TP_144008_20200923_20201006_02_T1

Table S54: List of Landsat-8 scenes used in the sensitivity test.

	$\dfrac{\partial \text{SIC}}{\partial \text{NDSI}}$ [%]	$\dfrac{\partial \text{SIC}}{\partial \rho_5}$ [%]
Sensitivity	-0.64	-36.95

Table S65: Sensitivities computed numerically over all 480 scenes.

Region	Sensitivity	
	$\dfrac{\partial \text{SIC}}{\partial \text{NDSI}}$ [%]	$\dfrac{\partial \text{SIC}}{\partial \rho_5}$ [%]
Baffin Bay	-0.81	-53.43
Barents Sea	-0.52	-43.21
Beaufort Sea	-0.50	-20.21
Bering Sea	-2.83	-58.45
Canadian Archipelago	-0.13	-16.34
Central Arctic	-0.41	-37.24
Chukchi Sea	-0.16	-29.72
E. Greenland Sea	-0.84	-42.95
E. Siberian Sea	-0.03	-35.53
Hudson Bay	-1.33	-35.61
Kara Sea	-0.76	-28.85
Laptev Sea	-0.14	-41.74

Table S76: Sensitivities computed numerically over each sub-region.

Cloud contamination category	Sensitivity	
	$\dfrac{\partial \text{SIC}}{\partial \text{NDSI}}$ [%]	$\dfrac{\partial \text{SIC}}{\partial \rho_5}$ [%]
C1	-2.22	-42.74
C2	-0.03	-33.02
C3	-0.14	-44.31
C4	-0.03	-26.82

Table S87: Sensitivities computed numerically for each cloud contamination category.

SIC sub-range [%]	Sensitivity	
	$\dfrac{\partial \text{SIC}}{\partial \text{NDSI}}$ [%]	$\dfrac{\partial \text{SIC}}{\partial \rho_5}$ [%]
0-10	-0.08	-7.64
10-20	-0.81	-144.01
20-30	-1.06	-230.27
30-40	-1.26	-265.66
40-50	-1.44	-276.95
50-60	-1.22	-297.54
60-70	-0.93	-274.00
70-80	-0.69	-240.84
80-90	-0.39	-149.76
90-100	-0.02	-12.82

Table S98: Sensitivities computed numerically over each SIC sub-range.

S65 Landsat-8 SIC Dataset

Sub-region	Cloud Contamination Category	Mean SIC [%]	Std. SIC [%]	N_{scene}	N_{pixel}
Baffin Bay	C1	69.59	43.27	727	76301
	C2	92.63	20.85	68	9441
	C3	47.53	44.54	886	183815
	C4	56.71	42.8	626	117085
Barents Sea	C1	50.15	47	258	40845
	C2	97.3	10.66	6	1086
	C3	26.21	41.02	244	72665
	C4	24.77	40	123	28844
Beaufort Sea	C1	89.83	26.06	194	37323
	C2	99.25	5.63	21	6598
	C3	75.58	36.89	101	28933
	C4	91.51	21.33	94	26529
Bering Sea	C1	57.4	46.82	152	20114
	C2	96.29	9.83	19	3303

	C3	28.45	42.12	234	59792
	C4	53.24	45.55	179	45355
Canadian A	C1	97.86	12.13	1537	291922
	C2	99.65	4.18	142	19808
	C3	84.52	32.78	819	204867
	C4	89.99	27.19	540	149110
Central Arctic	C1	88.03	29.91	1132	179148
	C2	99.67	2.9	40	7688
	C3	88.12	27.51	646	142530
	C4	86.35	28.5	385	68150
Chukchi Sea	C1	88.89	29.61	144	30839
	C2	97.9	8.31	31	5604
	C3	49.51	46	127	37332
	C4	81.48	35.39	106	27544
E. Greenland Sea	C1	73.07	40.78	641	84769
	C2	97.02	7.71	26	5717
	C3	55.13	44.91	353	83192
	C4	66.98	41.96	301	70497
E. Siberian Sea	C1	95.09	19.67	227	50554
	C2	99.44	5.81	38	9864
	C3	72.91	41.4	136	40397
	C4	86.24	31.87	132	37685
Hudson Bay	C1	78.39	38.99	565	84843
	C2	96.28	11.38	106	10182
	C3	43.8	45.67	348	96689
	C4	53.92	46.32	385	105082
Kara Sea	C1	86.79	31.7	448	87498
	C2	99.22	5.93	31	4681
	C3	53.49	45.41	236	68225
	C4	65.42	44.35	125	36858
Laptev Sea	C1	86.22	32.04	311	61149
	C2	97.57	10.45	21	5658
	C3	53.34	47.14	159	35842
	C4	77.42	38.06	127	32446

Table S109: The mean and the standard deviation of Landsat-8 SIC during the study period and the number of Landsat-8 scenes used for SIC production (N_{scene}) and the number of Landsat-8 SIC pixels produced (N_{pixel}) over the twelve sub-regions for the four cloud contamination categories.

S7̶6̶ Evaluation of Ice And Open Water Classification Over Cloud Pixels
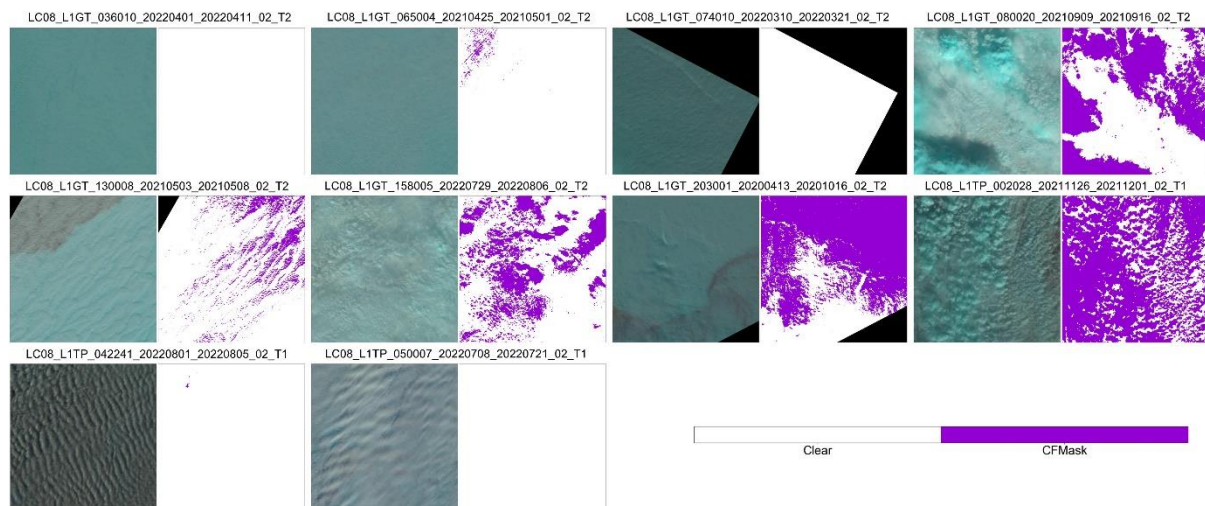
Figure S3̶2̶: **The (left panel) True-color image and (right panel) estimated cloud mask from CFMask over 10 scenes used for evaluation of SICs produced under C1. Cloud pixels detected by CFMask are shown as purple colour pixels. Cloud pixels undetected by CFMask are shown as black colour pixels. Fill values are shown as black colour pixels. The true-color images were downloaded from United States Geological Survey Earth Explorer The true-color images were downloaded from United States Geological Survey Earth Explorer (https://earthexplorer.usgs.gov/, last access: May 22, 2024).**

Region	Filename
Canadian Archipelago	LC08_L1GT_036010_20220401_20220411_02_T2
Central Arctic	LC08_L1GT_065004_20210425_20210501_02_T2
Beaufort Sea	LC08_L1GT_074010_20220310_20220321_02_T2
Bering Sea	LC08_L1GT_080020_20210909_20210916_02_T2
Laptev Sea	LC08_L1GT_130008_20210503_20210508_02_T2
Kara Sea	LC08_L1GT_158005_20220729_20220806_02_T2
Barents Sea	LC08_L1GT_203001_20200413_20201016_02_T2
Baffin Bay Labrador Seas	LC08_L1TP_002028_20211126_20211201_02_T1
East Greenland Sea	LC08_L1TP_042241_20220801_20220805_02_T1
Canadian Archipelago	LC08_L1TP_050007_20220708_20220721_02_T1

Table S1̶1̶0̶: List of Landsat-8 scenes used to evaluate SICs produced under C1.